2015

SHAPE MEMORY BEHAVIOR OF SINGLE CRYSTAL AND POLYCRYSTALLINE Ni-RICH NiTiHf HIGH TEMPERATURE SHAPE MEMORY ALLOYS

Sayed M. Saghaian
University of Kentucky, ssaghaian@yahoo.com

Recommended Citation

Saghaian, Sayed M., "SHAPE MEMORY BEHAVIOR OF SINGLE CRYSTAL AND POLYCRYSTALLINE Ni-RICH NiTiHf HIGH TEMPERATURE SHAPE MEMORY ALLOYS" (2015). *Theses and Dissertations--Mechanical Engineering*. 65.
https://uknowledge.uky.edu/me_etds/65

STUDENT AGREEMENT:

I represent that my thesis or dissertation and abstract are my original work. Proper attribution has been given to all outside sources. I understand that I am solely responsible for obtaining any needed copyright permissions. I have obtained needed written permission statement(s) from the owner(s) of each third-party copyrighted matter to be included in my work, allowing electronic distribution (if such use is not permitted by the fair use doctrine) which will be submitted to UKnowledge as Additional File.

I hereby grant to The University of Kentucky and its agents the irrevocable, non-exclusive, and royalty-free license to archive and make accessible my work in whole or in part in all forms of media, now or hereafter known. I agree that the document mentioned above may be made available immediately for worldwide access unless an embargo applies.

I retain all other ownership rights to the copyright of my work. I also retain the right to use in future works (such as articles or books) all or part of my work. I understand that I am free to register the copyright to my work.

REVIEW, APPROVAL AND ACCEPTANCE

The document mentioned above has been reviewed and accepted by the student's advisor, on behalf of the advisory committee, and by the Director of Graduate Studies (DGS), on behalf of the program; we verify that this is the final, approved version of the student's thesis including all changes required by the advisory committee. The undersigned agree to abide by the statements above.

Sayed M. Saghaian, Student

Dr. Haluk E. Karaca, Major Professor

Dr. Haluk E. Karaca, Director of Graduate Studies

SHAPE MEMORY BEHAVIOR OF SINGLE CRYSTAL AND POLYCRYSTALLINE Ni-RICH NiTiHf HIGH TEMPERATURE SHAPE MEMORY ALLOYS

DISSERTATION

A dissertation submitted in partial fulfillment of the
requirements for the degree of Doctor of Philosophy in the
College of Engineering
at the University of Kentucky

By
Sayed M. Saghaian
Lexington, Kentucky

Director: Dr. Haluk E. Karaca, Professor of Mechanical Engineering
Co-Director: Dr. Yang-Tse Cheng, Professor of Materials Engineering
Lexington, Kentucky
2015

ABSTRACT OF THE DISSERTATION

SHAPE MEMORY BEHAVIOR OF SINGLE CRYSTAL AND POLYCRYSTALLINE Ni-RICH NiTiHf HIGH TEMPERATURE SHAPE MEMORY ALLOYS

NiTiHf shape memory alloys have been receiving considerable attention for high temperature and high strength applications since they could have transformation temperatures above 100 °C, shape memory effect under high stress (above 500 MPa) and superelasticity at high temperatures. Moreover, their shape memory properties can be tailored by microstructural engineering. However, NiTiHf alloys have some drawbacks such as low ductility and high work hardening in stress induced martensite transformation region. In order to overcome these limitations, studies have been focused on microstructural engineering by aging, alloying and processing.

Shape memory properties and microstructure of four Ni-rich NiTiHf alloys ($Ni_{50.3}Ti_{29.7}Hf_{20}$, $Ni_{50.7}Ti_{29.3}Hf_{20}$, $Ni_{51.2}Ti_{28.8}Hf_{20}$, and $Ni_{52}Ti_{28}Hf_{20}$ (at. %)) were systematically characterized in the furnace cooled condition. H-phase precipitates were formed during furnace cooling in compositions with greater than 50.3Ni and the driving force for nucleation increased with Ni content. Alloy strength increased while recoverable strain decreased with increasing Ni content due to changes in precipitate characteristics.

The effects of the heat treatments on the transformation characteristics and microstructure of the Ni-rich NiTiHf shape memory alloys have been investigated. Transformation temperatures are found to be highly annealing temperature dependent. Generation of nanosize precipitates (~20 nm in size) after three hours aging at 450 °C and 550 °C improved the strength of the material, resulting in a near perfect dimensional stability under high stress levels (> 1500 MPa) with a work output of 20–30 J cm^{-3}. Superelastic behavior with 4% recoverable strain was demonstrated at low and high temperatures where stress could reach to a maximum value of more than 2 GPa after three hours aging at 450 and 550 °C for alloys with Ni great than 50.3 at. %.

Shape memory properties of polycrystalline $Ni_{50.3}Ti_{29.7}Hf_{20}$ alloys were studied via thermal cycling under stress and isothermal stress cycling experiments in tension. Recoverable strain of ~5% was observed for the as-extruded samples while it was decreased to ~4% after aging due to the formation of precipitates. The aged alloys demonstrated near perfect shape memory effect under high tensile stress level of 700 MPa and perfect superelasticity at high temperatures up to 230 °C. Finally, the tension-compression asymmetry observed in NiTiHf where recoverable tensile strain was higher than compressive strain.

The shape memory properties of solutionized and aged Ni-rich $Ni_{50.3}Ti_{29.7}Hf_{20}$ single crystals were investigated along the [001], [011], and [111] orientations in compression. [001]-oriented single crystals showed high dimensional stability under stress levels as high as 1500 MPa in both the solutionized and aged conditions, but with transformation strains of less than 2%. Perfect superelasticity with recoverable strain of more than 4% was observed for solutionized and 550 °C-3h aged single crystals along the [011] and [111] orientations, and general superelastic behavior was observed over a wide temperature range. The calculated transformation strains were higher than the experimentally observed strains since the calculated strains could not capture the formation of martensite plates with (001) compound twins.

KEYWORDS: NiTiHf, High Temperature Shape memory alloys, Mechanical
Characterization, High Strength Shape Memory Alloy,
Orientation Dependence of NiTiHf

Sayed M. Saghaian

Student's Signature

08/05/2015

Date

SHAPE MEMORY BEHAVIOR OF SINGLE CRYSTAL AND POLYCRYSTALLINE Ni-RICH NiTiHf HIGH TEMPERATURE SHAPE MEMORY ALLOYS

By

Sayed M. Saghaian

Haluk E. Karaca

Director of Dissertation

Yang-Tse Cheng

Co-Director of Dissertation

Haluk E. Karaca

Director of Graduate Studies

08/05/2015

This work is dedicated to my mother and father.

ACKNOWLEDGEMENTS

Foremost, I would like to sincerely thank my advisor, Prof. Haluk E. Karaca, who provided his guidance to complete this research and thought me how to do scientific research. His willingness to dedicate his time so generously has been very much appreciated. He was always approachable when I had questions about the research. This dissertation could not have been made possible without his tremendous guidance and invaluable comments. I cannot thank him enough for his patient guidance and enthusiastic encouragement during my research.

I would also like to thank the other dissertation committee members for their help and support. Our collaborator from NASA Glenn Research Center, Prof. R. Noebe who supplied all the polycrystalline material for this research and was always available for question about shape memory alloys. Additionally, I thank Prof. Chumlyakov for providing single crystals and his valuable suggestions. I would also like to thank Prof. J. Pons and Dr. R. Santamarta for all their help on the TEM work and the valuable comments about the findings. My grateful thanks are also extended to Dr. Burak Basaran for his help to conduct the experiments.

I would also like to offer my special thanks to my lab-mates, Gurdish Ded, Mohammad Souri, Ali Sadi Turabi, Soheil Saedi, Emre Acar, Irfan Kaya, Peizhen Li and Sesha Spandana Pulla. I also appreciate the generous help from Dr. Hirobumi Tobe for TEM experiments. Thanks also to the technicians of the mechanical engineering department for their help.

I would like to express my gratitude to my father, mother, and brothers for their constant support. Especially, many thanks go to my brother, Sayed Y. Saghaian, who support and encouraged me during my research.

Finally, I would like to thanks the NASA Fundamental Aeronautics Program, Supersonics Project and the NASA EPSCOR program for funding the project.

Table of Contents

List of Tables

List of Figures

1 Introduction

1.1 Motivation and Statement of Problem

For centuries, metals have played a significant role as structural materials. With advancement in science and a better understanding of the effects of microstructure and processing techniques on the material behavior, the field of material science has fundamentally improved through the past decades. Active materials are specialized subgroups of a new branch of materials called multifunctional materials, which in general exhibit a mechanical response when subjected to non-mechanical field (i.e. thermal, electrical, magnetic, optical, etc.). Some example of active materials includes shape memory alloys (coupling of thermal with mechanical field), piezoelectric and piezomagnetic (coupling of mechanical with electrical and magnetic fields). An ideal active material would have high actuation energy density. Figure 1.1 shows typical ranges of actuation stress, actuation strain, and actuation energy densities of some common active materials. The actuation energy density is denoted by dotted lines and is calculated by product of the actuation stress with the actuation strain, assuming here that the active material is operating under constant stress [1]. Shape memory alloys (SMAs) have the ability to recover their shape when the temperature is increased and they show shape recovery under high stress levels therefore resulting in high actuation energy densities as shown in Figure 1.1. Magnetic SMAs and shape memory polymers have higher actuation energy density and larger actuation strain in contrast with other type of active materials. In addition, under specific conditions, SMAs can absorb and dissipate mechanical energy by undergoing a reversible hysteretic shape change when subjected to apply mechanical cyclic loading. These unique characteristics of SMAs have made them a good candidate for actuation, sensing, vibration damping and impact absorption applications. The application of SMAs have permeated into the mainstream of many industries, particularly in the biomedical, transportation, energy, and aerospace fields [1, 2]. One important application is in the field of actuators. Repeated cyclic motions are achieved by heating and cooling these alloys providing thermal actuators. SMA actuators exist in a variety of forms such as ribbons, wires and thin films. Among the various forms of SMA, solid state actuation systems for use in the aerospace, automotive and energy industries is currently driving research in "high temperature shape memory alloys" (HTSMAs) [3].

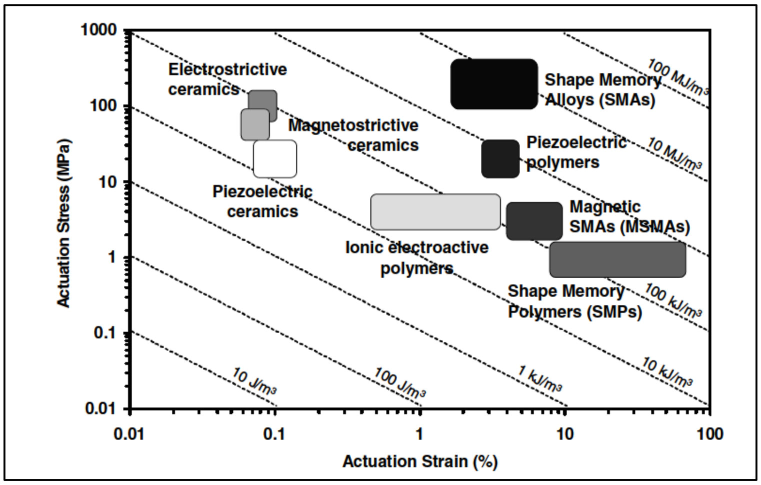

Figure 1.1: Actuation energy density diagram of different active materials [1].

NiTi is the most explored and also the most widely utilized SMA due to its good dimensional stability, superior shape memory properties, corrosion resistance, biocompatibility, ductility, and high work output capability. However, it can only operate below 100 °C due to its low martensitic transformation temperature [4]. This limitation in conventional NiTi alloys has resulted in the development of HTSMAs that can operate at temperatures above 100 °C. Recently, the aerospace, automotive, oil and many other industries have become interested in compact, lightweight, high force and high strain

HTSMAs since SMAs intrinsically possess higher energy density than most conventional actuators. Furthermore, they are robust, frictionless, do not require extraneous systems such as hydraulic or pneumatic lines, and are easier to inspect and maintain [4, 5]. HTSMAs can be used in several practical application such as; clearance control in the compressor and turbine sections of aircraft engines, variable geometry inlets and nozzles for subsonic and supersonic aircraft, flow control devices, shape changing or articulating blades, safety switches, self-damping components in fuel line clamps, flutter control, and damping of fan blades [3, 6].

Ternary elements are added to Ni-Ti alloys to increase their transformation temperatures (TTs) with the hope to maintain its superior shape memory and mechanical properties. It has been founded that the additions of Hf, Zr, Pd, Pt, and Au elements result in an increase in the TTs but also a decrease in the ductility. Among those elements Pd, Pt, and Au are very expensive and Zr is associated with high oxygen affinity [3, 4, 7]. Among the potential HTSMAs, due to its low cost, medium ductility and high work output NiTiHf seems to be the most promising HTSMA for a wide range of applications in the critical 100-300 °C temperature range [5]. Most HTSMA research was focused on (Ti+Hf)-rich NiTiHf alloys due to the low TTs of Ni-rich materials. However, Ti-rich NiTiHf alloys exhibit poor mechanical and functional properties including a large temperature hysteresis (>50 °C), low strength, low transformation strain (when compared to NiTi), lack of cyclic stability due to the high stresses required for reorientation of martensite and detwinning, and low resistance to slip leading to plastic deformation of both the martensite and austenite phases at relatively low stresses [5, 8].

For practical applications, some of the most important issues with SMAs are the large plastic deformations observed at high temperatures and stress levels, unstable cyclic performance, and a strong orientation/texture-dependent behavior [3, 9]. In addition, several other factors (e.g. creep and oxidation) can uniquely affect the shape memory behavior in the high temperature regime [5, 10]. The most important problem in HTSMAs is the low strength for dislocation generation and motion which result in large irrecoverable strain and cyclic instability [3, 4, 8]. Among the most common methods employed to improve the shape memory and mechanical properties of SMAs are thermomechanical processing, precipitate hardening, solid solution hardening, and grain refinement of polycrystalline alloys [2, 5, 8, 11-16]. Unfortunately, the majority of prospective HTSMAs systems are ordered intermetallic with limited ductility at low and intermediate temperatures, making it difficult and expensive to apply thermomechanical processing techniques to increase the material's strength. Thus, to increase the strength of the material, precipitation and solid solution hardening are the most practical and cost-effective method amongst the others. It has been shown that by employing nanoscale particles, the strength of the matrix can be increased by raising the critical shear stress for slip, which in turn improves shape memory properties and fatigue life [17-20].The introduction of nanoscale particles to serve as barriers to dislocation motion would also improve the fatigue life and cyclic stability [17-19]. The strengthening ability of the precipitates depends on the size, volume fraction, interparticle spacing, and coherency of the second phase [21]. In addition to aging time and temperature, lattice mismatch between the matrix and precipitates introduce local stress files which alter the strengthening behavior, martensite nucleation and shape memory and material properties.

It is a reasonable assumption that through alloying and thermal treatments, precipitation properties can be controlled and precipitation could be utilized to design NiTiHf alloys with high TTs, high strength, stable response that can be employed for SMA applications above 100 °C. This statement is based on the former knowledge on Ni-rich NiTi alloys where formation of coherent nanosize precipitates (e.g, Ni_4Ti_3, Ni_3Ti_2) significantly improves the shape memory behavior due to their strong pinning effect on dislocation movement [17, 19].

1.2 Technical Approach and Objectives

In order to understand the effects of chemical composition on precipitation characteristics, four alloys systems $Ni_{50.3}Ti_{29.7}Hf_{20}$, $Ni_{50.7}Ti_{29.3}Hf_{20}$, $Ni_{51.2}Ti_{28.8}Hf_{20}$, and $Ni_{52}Ti_{28}7Hf_{20}$ will be studied. Their TTs and thermal hysteresis will be determined using Differential Scanning Calorimeter (DSC). For selected cases, Scanning Electron Microscopy (SEM) with Energy dispersive spectroscopy (EDS) capabilities will be used to determine the composition of matrix and second phases. Also, the structure of transforming phases will be determined using X-ray Diffraction (XRD). If alloys are in two phase condition, homogenization at high temperatures for a long time will be done at temperatures determined by high temperature DSC. Heat treatments will be applied to four alloys systems to form precipitates. In selected cases, cyclic DSC tests will be employed to determine the stability of the material response. Microhardness tests will be employed to determine the strength of the alloys as function of aging time and temperature. Transmission Electron Microscopy (TEM) investigation will be employed to determine the precipitation size, volume, distribution and structure as functions of composition and thermal treatments.

For practical applications, we must determine the shape memory and mechanical behavior of HTSMAs. Through the composition and aging study, optimum heat treatments for the alloys systems will be determined. According to this knowledge, compression and tension samples will be aged at predetermined temperatures for certain periods of time. Then two main experiments will be conducted; i) ***Thermal cycling under stress***: to determine the, thermal hysteresis, transformation strain, dimensional stability and work output of material, which are the main factors for actuator applications, as a function of applied stress ii) ***Isothermal stress-strain experiment*** : to investigate the critical stress for phase transformation (or variant reorientation), transformation strain, stress hysteresis, Young's modulus of transforming phases as functions of temperature. The results from thermal and stress cycling will be used to determine the phase diagram with Clausius-Clapeyron (CC) slope of both compression and tension samples.

To develop, process and characterize shape memory and material properties of Ni-rich NiTiHf, the following objectives are proposed:

1. Investigate the effects of chemical composition on shape memory and material properties of NiTiHf high temperature shape memory alloys.
2. Reveal the influences of heat treatment time and temperature on the martensite morphology, transformation temperatures and strain, thermal and mechanical hysteresis and work output of polycrystalline and single crystalline NiTiHf alloys.
3. Study the tension-compression asymmetry in NiTiHf alloys.
4. Investigate the orientation dependence of shape memory properties of NiTiHf alloys.

5. Study the microstructural dependence of the shape memory behavior and stored elastic energy in NiTiHf alloys
6. Calculate the theoretical transformation strain of single crystals and compare with the experimental results.

The most important result of this study will be to understand the precipitation characteristics of NiTiHf alloys to gain the fundamental understanding on composition-microstructure-property relationship in HTSMAs. By utilizing that knowledge, inexpensive NiTiHf based HTSMAs with stable shape memory and material properties that can operate reliably at temperatures higher than 100 °C can be fabricated. By understanding and controlling the structure of these materials, we should be able to develop next generation shape memory alloys fully capable of enabling the development of adaptive aero-structures such as lightweight, durable high temperature engine materials, airframes for aircrafts such as engine chevrons, torque actuators. The developed alloys can be used where conventional actuators cannot be used because of weight or size limitations. Aircraft with adaptive SMA structures will have improved performance, reduced fuel consumption, and will have minimal environmental impact because of reduced emissions and noise.

1.3 Brief Background on Shape Memory Alloys

Shape memory alloys are a class of metal alloys that show thermomechanical memory and are capable of converting thermal energy into mechanical work. In other word, SMAs are an extraordinary group of material that undergoes a solid to solid diffusionless phase transformation and as consequences can produce very high recoverable shape changes (up to 20% uniaxial strain), stresses (~100-500 MPa) and work output (~10 MJ/m^3) [1, 9]. The phase transformation involve the coordinate motion of the atoms over very short distances in the crystal as the material structure transforms from one lattice type to another. The SMAs have two stable phases, the high temperature phase, called "*austenite"*, and the low temperature phase, called "*martensite".* Austenite phase is a high symmetry structure and low temperature structure has a lower symmetry. In addition, the martensite phase can be in one of two forms: twinned (self-accommodated) and detwinned (Deform martensite). A phase transformation which occurs between these two phases by thermal cycling and/or stress-strain cycling upon are the basis for the unique properties of the SMAs which will discuss in detail in next section.

Adolf Martens revealed the martensite in steels in the 1980s and his discovery was a major step toward the eventual discovery of SMAs. However, the martensitic transformation observed in the Fe-C system was an irreversible process. The martensitic transformation in SMAs is found to be reversible in the sense that as material cool down from austenite to martensite phase the "*forward*" transformation takes place and a subsequent increase in temperature results in "*reverse*" transformation (martensite to austenite). In 1932, Olander observed that the deformation after applied stress to gold-cadmium (Au-Cd) can fully recover by heating. For the first time, the concept of thermoelastic martensitic transformation, which explained the reversible transformation of martensite upon heating, was experimentally observed in CuZn and CuAl by Kurdjumove and Kandros in 1949 [22]. In 1951, Chang and Read [23] reported the shape memory properties of Au-Cd by studying the boundary motion between austenite and martensite phases during phase transformation using electrical resistivity measurement and X-ray analysis.

The discovery of shape memory effect in nearly equiatomic NiTi alloy by the group of William Buehler [24], while trying to develop lightweight high temperature aerospace alloys at Noval Ordinance Laboratory (NOL) in 1963, brought a breakthrough for the engineering application. They demonstrated that the system possessing shape memory effect, which is the ability of material to return to a undeform shape upon finishing the phase transformation, could perform work. During their research at NOL, Buehler showed that the NiTi alloy revealed good mechanical properties and confirmed the occurrence of the shape memory effect in this type of material. Significant research carried out by Wang [25], displays that the addition of a third alloying element such as Fe or Co to the existing NiTi system had a strong influence on the TTs. The new alloys was used for pipe couplings in F14 fighter aircraft as the first commercial SMA application, known as Cryofit [26, 27]. Continued research led to development of NiTiNb [26] alloy with the comparably higher TTs and found widespread applications in battle damage repair and in repairs for nuclear reactors [28]. However, Melton and Mercier [29], while studying the fatigue properties of NiTi in 1978, showed that the addition of Cu to NiTi doesn't change the TTs considerably, but narrowed the stress hysteresis. Later in 1999, Miyazaki [30] showed that the addition of Cu to NiTi improved the fatigue properties of this material system. The improved fatigue life and the low cost associated with this material system made it promising candidate for a wide variety of engineering applications.

Shape memory alloys can display the distinctive properties of shape memory effect and superelasticity due to reversible martensitic transformations and therefore have been employed in many industrial applications [2, 3, 7, 9, 31]. Shape memory and superelastic behaviors are functions of a large number of factors that include microstructural features (e.g. martensite morphology, grain size, dislocation density and precipitate characteristics) as well as external influences such as applied stress and temperature [5] and will discussed in the following sections.

1.3.1 Thermodynamics of Martensitic Transformations in SMAs

Unique behavior of SMAs is due to the reversible shape changes corresponded to martensitic phase transformations. A martensitic transformation is an example of a displacive (diffusionless shear transformation) transition, in which there is cooperative motion of a relatively large number of atoms, each being displaced by only a small distance and they move in an organized manner relative to their neighbors. This homogeneous shearing of the parent phase creates a new crystal structure, without any compositional change (no diffusion). A simple thermodynamic analysis of the phase transformations is given here. The Gibbs free energy general form is given by;

$$\Delta G = \Delta H - T\Delta S \tag{1.1}$$

where ΔH is the enthalpy change, ΔS is the entropy change and T is temperature. For simplicity, the Gibbs free energies of martensite and austenite can be assumed to be decreasing linearly with temperature. At the intersection of their Gibbs free energy curves, the transforming phases have the same free energy and are in equilibrium at the equilibrium temperature (T_0). Below T_0, martensite is favored thermodynamically since it has lower free energy while austenite is stable above T_0. The schematic of energy curves for austenite to martensite phase transformation are illustrated in Figure 1.2. G_{Ch}^{A} and G_{Ch}^{M} are the chemical energies of austenite and martensite, respectively.

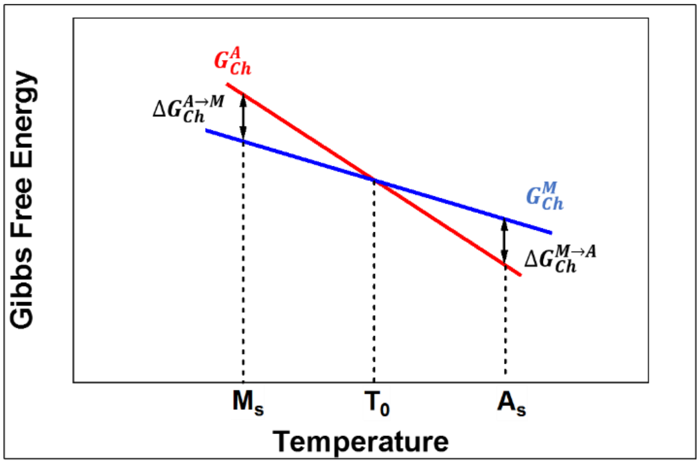

Figure 1.2: Schematic Gibbs free energy versus temperature curves for martensite and austenite.

$\Delta G_{Ch}^{A\to M}$ is the chemical driving force for phase transformation from austenite to martensite and $\Delta G_{Ch}^{M\to A}$is the driving force for reverse transformation. Martensitic transformations are considered thermoelastic if the martensite reverts to the austenite in its original orientation upon heating. Thermoelastic equilibrium at a transforming interface requires a local balance between chemical and non-chemical contributions of the total Gibbs free energy of the system. The chemical constituent is a result of the chemical energy different between the austenitic and martensitic phases due to the nature of bonding in the crystalline phases. Without non-chemical energy, the transformation would take place when the G_{Ch}^{M} and G_{Ch}^{A} are equal to each other ($\Delta G_{ch}=0$) at T_0. However, the forward and reverse transformation starts temperatures, M_s and A_s, respectively, are shifted respect to T_0 as illustrated in Figure 1.2, which provides the finite driving force necessary to balance non-chemical energy. The non-chemical components are reversible (elastic) and irreversible energies and the general thermodynamical equilibrium equation for the forward transformation can be written of the forms [32];

$$\Delta G_{total}^{A\to M} = \Delta G_{Ch}^{A\to M} + \Delta G_{nc}^{A\to M} = \Delta G_{Ch}^{A\to M} + \Delta G_{el}^{A\to M} + \Delta G_{irr}^{A\to M} \qquad (1.2)$$

where $\Delta G_{total}^{A\rightarrow M}$ is the total Gibbs free energy difference to initiate the martensitic transformation, $\Delta G_{Ch}^{A\rightarrow M}$ is the change in chemical energy, $\Delta G_{nc}^{A\rightarrow M}$ is the change in non-chemical energy. The non-chemical energy can be expressed as a combination of the change in elastic energy, $\Delta G_{el}^{A\rightarrow M}$, and the irreversible energy, $\Delta G_{irr}^{A\rightarrow M}$, during the phase transformation from austenite to martensite [33]. $\Delta G_{total}^{A\rightarrow M}$ term should be smaller than zero in order to initiate the martensitic transformation. At T_0, since there is no driving force to trigger the martensitic transformation, an additional energy should be supplied (by cooling or heating) to initiate the transformation.

Additional cooling (T_0–M_s) below T_0 is necessary for austenite to martensite transformation and additional heating (A_s-T_0) beyond T_0 is required for martensite to austenite transformation assuming negligible elastic energy storage. Shape memory effect and superelasticity originate from the thermoelastic martensitic transformation [34]. $\Delta G_{el}^{A\rightarrow M}$ is the stored elastic energy during the forward transformation and it is released completely upon back transformation from martensite to austenite. Hence, the elastic energy storage is a reversible process [32]. The amount of the stored elastic energy should be equal to the released energy upon reverse transformation if there is no plastic relaxation due to dislocation generation/plastic deformation after a full transformation cycle [35, 36].

The irreversible energy $\Delta G_{irr}^{A\rightarrow M}$ can be assumed as a combination of mainly frictional energy that is required to move phase front (between transforming phases), friction between martensite variants and internal twins in variants in addition to plastic relaxation energy due to dislocation generation. Both of the abovementioned mechanisms result in dissipation of energy and consequently, hysteresis in SMAs [37]

1.3.2 Thermal Induced Martensitic Transformation

Phase transformation in SMAS can be controlled by temperature or stress. Temperature induced martensitic transformation can take place under applied stress or in a stress free condition. Figure 1.3 illustrates the temperature induced phase transformation in the absence and presence of applied mechanical loading. In Figure 1.3a, phase transformations are represented as peaks and the areas under those peaks indicate the enthalpies of transformations. Upon cooling the material from the high temperature austenite phase transforms into self-accommodated (twin) martensite. As a result of this phase transformation no observable macroscopic shape change occurs. Upon heating, a reverse phase transformation takes place and as a result, the material in the martensitic phase transforms to austenite. It is known that the forward transformation (austenite to martensite) is exothermic and the reverse transformation is endothermic reactions. There are specific temperatures at which the transformation from austenite to martensite and its reverse transformation begins and end. These temperature are commonly referred to as the martensite start temperature (M_s) which is the temperature that the material starts transforming from austenite to martensite; martensite finish temperature (M_f), at which the forward transformation (martensite to austenite) is complete and the material is fully in the martensite phase; austenite start temperature (A_s) at which the reverse transformation (austenite to martensite) initiates; and austenite finish temperature (A_f) at which the reverse phase transformation is completed and the material is fully in austenite phase. It is important to know TTs so that the alloy can be effectively used for a specific application. The enthalpy change ($\triangle H$) of the phase transition can be found by integrating the area between to selected temperatures as shown in the Figure 1.3a. It is also possible that thermal induce a martensitic phase transformation which lead directly to (partially or fully) detwinned (or oriented) martensite and it is shown in Figure 1.3b. If stress isothermally applied in austenitic phase and then the material is cooled, the phase transformation will result in detwinned martensite and a net shape change will be observed. Reheating the material to a temperature above A_f will result in complete shape recovery if the applied stress in not sufficient enough to introduce defects, i.e. plastic deformation, in the material. The TTs strongly depend on applied stress. Usually, the TTs have a linear relationship with applied load and TTs elevate with applied stress. Figure 1.3b illustrates the critical point for the transformation determined by using graphical method. Total strain, ε_{total}, was determined by measuring the distance between the cooling and heating portions at M_s and TTs were determined by tangent method. Thermal hysteresis, ΔT, was calculated as a temperature difference at the middle point of total cooling and heating curves. Irrecoverable strain, ε_{ir}, is the amount deformation that is not recover at the end of thermal cycle and it is the key parameter to determine the dimensional stability of the material for actuation application.

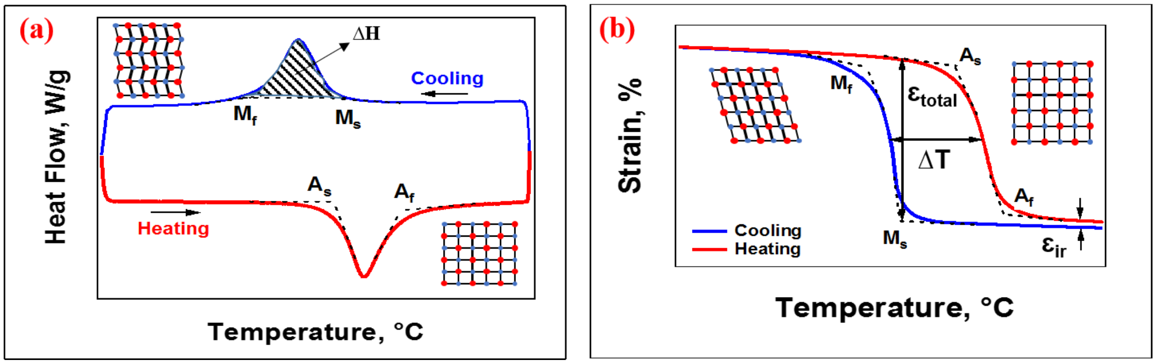

Figure 1.3: Thermal induce phase transformation in the absence (a) and presence (b) of applied stress.

1.3.3 Shape Memory Properties

There are unique properties exhibited by SMAs depending on TTs of the alloy and the operating temperature. If a mechanical load is applied to the SMA at temperature below M_f, it is possible to detwin the twinned martensite by reorienting a certain number of variants as shown in Figure 1.4. This deformation is therefore different from deformation induced by dislocation motion or deformation twins. The detwinning process results in a macroscopic shape change, where the materials remains in the deformed configuration upon releasing of the load. A subsequent heating of the SMA to a temperature above A_f will result in reverse phase transformation and will lead to complete shape recovery. This process is referred to as the *shape memory effect* (SME) or one way shape memory effect as illustrated in Figure 1.4a. It is worth to note that cooling back to a temperature below M_f leads to the formation of twinned martensite again with no associated shape change observed. The reason behind the phenomenon of SME is the formation of self-accommodating martensite structure in order to minimize energy upon cooling under no load. When a force applied in martensite, some favorable martensite variants grow at the expense of others and remain in detwin structure while the load is removed. Furthermore, the detwinned martensite variants transform to austenite phase during heating since it has a higher order of symmetry than martensite, while the self-accommodating martensite structure formed upon cooling in stress free condition, hence, there is no observed shape change. It is worth to mention that the remained strain might not fully recover by heating up above A_f if the stress is sufficient to introduce plastic deformation and irrecoverable strain (ε_{ir}) would present after heating cycle. The total recoverable strain is the combination of elastic (ε_{el}) and shape memory effect (ε_{sme}) strains.

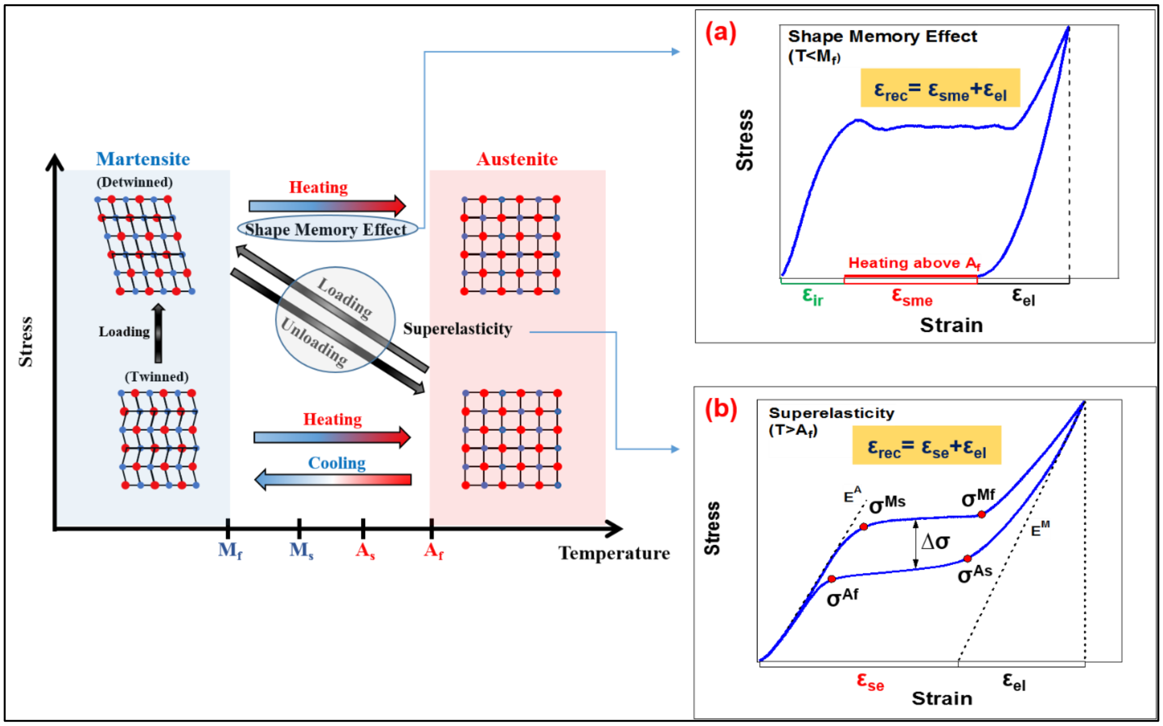

Figure 1.4: Schematic of shape memory effect and superelasticity behavior of SMAs.

In contrast to one way shape memory effect where the material only memorize the structure of parent phase, it is possible that the alloy remember the shape of both low and high temperatures phase. This phenomena is called as *two way shape memory effect* (TWSME) where material has the ability to generate strain by only thermal cycling in the absence of applied stress. This could be attributed to the development of local stress fields due to presence of defects, such as dislocations, that disrupt self-accommodating structure and favors formation of selective martensite variants upon cooling. It is important to note that the dislocations do not disappear during reverse transformation and they are present in the austenite phase. Thus, the stress fields around the dislocations induce particular martensite variants during cooling and hence a shape change observed during thermal cycling under stress free condition.

In addition to temperature induced martensitic transformation, SMAs also exhibit stress induced phase transformation. During loading at temperatures slightly above A_f, stress induced transformation leads to formation of detwinned martensite at sufficiently high stress levels and a complete shape recovery is observed upon unloading due to reverse transformation from martensite to austenite phase. This phenomenon is called *superelasticity* which is schematically shown in Figure 1.4. Superelasticity is represented in the stress-strain curve as shown in Figure 1.4b. After elastic deformation of austenite, the stress induced martensite transformation initiated at a critical stress level of σ^{Ms} and the martensitic transformation end at σ^{Mf}, followed by elastic deformation of martensite phase. Upon unloading, the martensite transforms back to austenite and deformation is ideally recovered. The total amount of superelasticity strain that is recovered upon unloading is symbolized by ε_{se} in Figure 1.4b and the stress hysteresis mentioned in the plot depicts the difference in critical stresses for forward and reverse transformation. Young Modulus of elasticity for austenite and martensite phase are represent by E^A and E^M, respectively.

It can be realized that the SME is a consequence of thermal cycling between A_f and M_f temperatures and superelasticity occurs due to stress induced martensitic transformation at temperatures above A_f. The Clausius-Clapeyron relationship (CC) is a best equation to describe the stress-temperature dependence of martensitic transformation in SMAs. The relationship for uniaxial stress can be written as follows:

$$\frac{d\sigma}{dT} = -\frac{\Delta S}{\varepsilon_{tr}} = -\frac{\Delta H}{\varepsilon_{tr} T_0} \qquad (1.3)$$

where σ is the uniaxial stress, ε_{tr} is the transformation strain, ΔS is the entropy of transformation per unit volume, ΔH is the enthalpy of transformation per unit volume, and

T_0 is the equilibrium temperature of transformation which is determined from the enthalpy and entropy changes of the transformation. Since ΔS, ΔH and T_0 are constant for a given system, hence the relation between stress and strain is linear. The equilibrium temperature of thermoelastic martensitic transformation can be calculated by the following equation [38, 39]:

$$T_0 = \frac{M_s + A_f}{2} \qquad (1.4)$$

The enthalpy changes of the forward and reverse martensitic transformation can be obtained by measuring the area of cooling and heating curves of thermal induce transformation in the absence of stress results. The entropy of martensitic transformation can be express as follows:

$$\Delta S = \frac{\Delta H_{avg}}{T_0} \qquad (1.5)$$

Critical stresses for martensite reorientation, martensitic transformation and dislocation slip are strongly testing temperature dependent and are schematized in Figure 1.5. It is noted from Figure 1.5 that SME occurs at temperatures below A_s and critical stress for the martensite reorientation decreases with temperature due to increased mobility of internal twins and martensite plates boundaries. The green line in the Figure 1.5 illustrates the critical stress required to induce martensitic transformation which follows the CC relation (Eq. 1.3) and increases with temperature. If the material is in austenite and deformed between M_s and A_f, stress induced martensitic transformation during loading and shape recovery cannot be obtained upon unloading, however, full recovery occurs when the temperature is increased above A_f temperature if no plastic deformation formed in the material. Superelasticity is observed when the sample deformed between A_f and martensite desist temperature (M_d) where the critical for slip is higher than the stress needed to induce martensitic transformation. Stress induced martensite cannot be observed above M_d and alloys deform like conventional materials [40]. The intersection of critical stresses of martensitic transformation and dislocation slip can be considered as M_d and it is shown in Figure 1.5. In general, the critical stress for slip (yield stress of austenite) decreases with increasing temperature. If the material is not strong enough or temperature is close to M_d, partial recovery can be observed since martensitic transformation and plastic deformation occur simultaneously. Also, plastic deformation of austenite takes place above M_d where stress induced martensitic transformation is no longer possible and shape recovery cannot be observed during unloading. Thus, superelasticity can only be observed between A_f and M_d where the difference between these temperatures is called superelastic window and shown as a shaded portion in Figure 1.5.

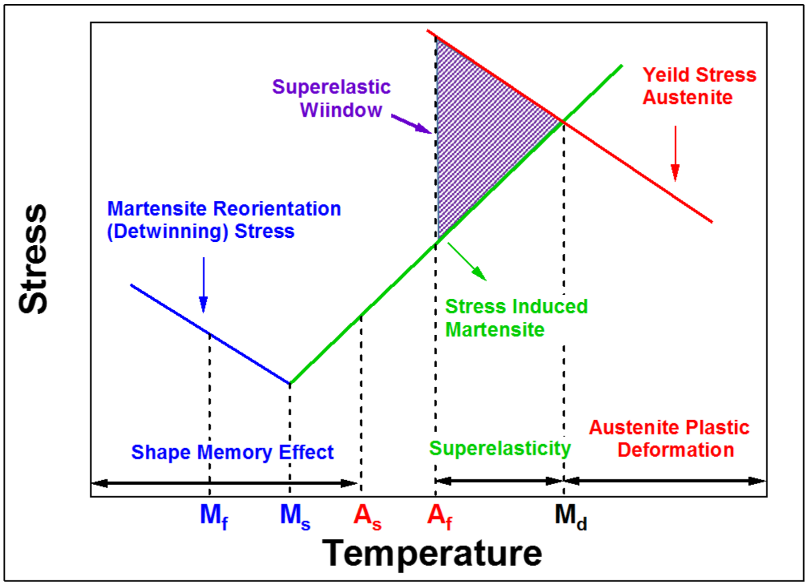

Figure 1.5: Schematic for the critical stresses of various deformation modes as a function of temperature in SMAs.

1.4 Literature Review on Binary NiTi and NiTi-based HTSMAs

1.4.1 Binary NiTi

Among the various shape memory alloy systems, NiTi alloys have good dimensional stability, shape memory properties, ductility and workability. Currently, NiTi alloys are the most commercially viable SMAs and practically being used in various medical and engineering applications where the operating temperature is below 100 °C [4]. Binary NiTi are ordered intermetallic compound that undergoes reversible martensitic transformation. From the phase diagram, this compound exist as the stable phase down to room temperature and the order-disorder of transition of equiatomic NiTi marked at 1090 °C [34]. The structure of high temperature austenite phase for NiTi is cubic (B2) and the low temperature martensite phase can be either monoclinic (B19’) or orthorhombic (B19). The B19 crystal structure is created by $(110)[1\bar{1}0]_{B2}$ shear of the B2 structure while B19’ crystal structure is created by the same shear as B19 with an additional $(001)[1\bar{1}0]_{B2}$ shear [41, 42]. It should be noted that crystal structures and lattice parameters are composition, alloying and thermomechanical treatment dependent [17, 34, 43, 44]. In fully annealed near stoichiometric NiTi, the high temperature B2 austenite phase transforms directly to monoclinic B19’ upon cooling through martensitic transformation [34]. In some cases in NiTi alloys, B2 austenite could transform to R-phase first followed by R to B19’ phase transformation upon cooling while the single step B19’ to B2 phase transformation occurs during revers transformation [45]. R-phase is a transition structure that has commonly rhombohedral structure, low transformation strain and temperature hysteresis [34]. R-Phase can be formed in NiTi alloys subsequent to cold working, aging of Ni-rich alloys and alloying with a third element such as iron [46]. Several factors have been proposed to explain multistage transformation in NiTi alloys such as stress fields around the precipitates, inhomogeneous distribution of precipitates and the inhomogeneity of the microstructure [47-50].

It has been demonstrated that the TTs of binary NiTi can be controlled through the Ni concentration of the alloy [51, 52]. Figure 1.6 illustrates the dependence of TTs on composition of NiTi. It is clear from Figure 1.6a that the M_s is less sensitive to compositional changes in the Ti-rich side of stoichiometry due to formation of Ti-rich precipitates (Ti_2Ni), leaving a near stoichiometric (Ti-50 at. % Ni) matrix composition [34]. As Ni content increases above 50 at.% in Ni-rich side of the stoichiometry, TTs decrease drastically to lower temperatures [17, 51]. This can be due to the fact that the elastic constant that dictate the shearing involve in the martensitic transformation are change to resists the austenite to martensite phase transformation, hence, undercooling is required. However, it can be seen from Figure 1.6b that aging can lead to a dramatic increase in TTs of Ni-rich NiTi alloys, whereas there is very little difference between the quenched and aged conditions of Ti-rich alloys. Thus, formation of metastable Ni_4Ti_3 precipitates after appropriate heat treatments in Ni-rich NiTi alloys greatly increase the TTs (Figure 1.6b) and improve the shape memory properties [17, 53, 54]. Consequently, Ni-rich NiTi shape memory alloys are coming into prominence due to their distinct superelasticity and shape memory properties as compared to near equiatomic NiTi SMAs. In addition, Ni-rich NiTi SMAs demonstrate unique properties such as good corrosion resistance, smooth surface finish, high toughness and lower density than steel makes them an excellent candidate for different applications in biomedical and energy industries [55].

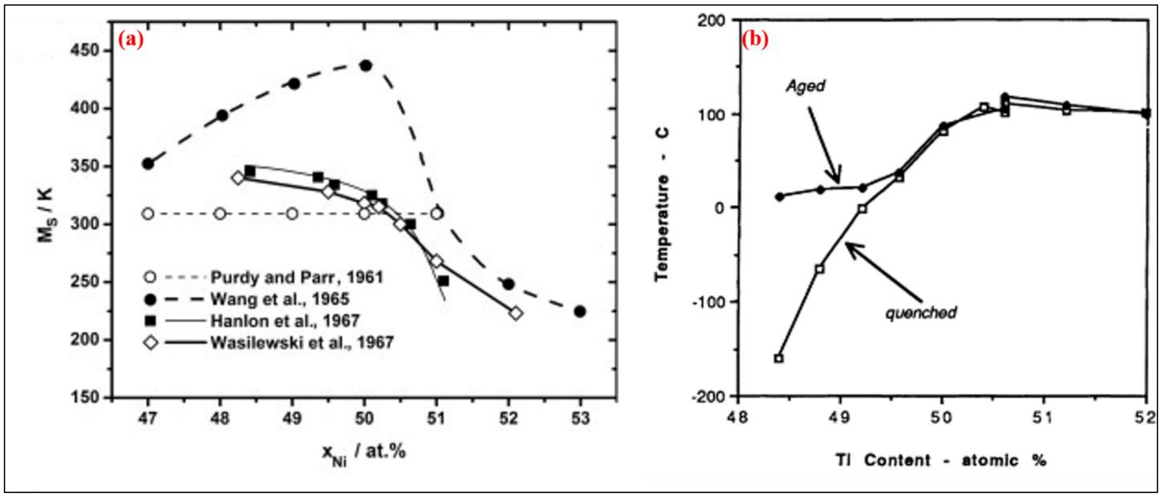

Figure 1.6: The dependence of TTs on (a) composition [56] and (b) aging [57].

As described above, TTs of Ni-rich NiTi alloys are very sensitive to the Ni content of the matrix where they decrease about 93 °C/ at % [58] and they increase with aging. In Ni-rich NiTi SMAs, aging introduces metastable and stable second phases which alters the composition of the matrix. Nishida et al. reported [59] that the complete sequence of precipitation from metastable to stable phase is to be $Ti_3Ni_4 \rightarrow Ti_2Ni_3 \rightarrow TiNi_3$ after aging of a Ni-rich NiTi alloy. At low aging temperatures or short aging time, the precipitates are metastable Ni_4Ti_3 while the stable Ni_3Ti phase introduced into matrix at high temperature or long duration heat treatments. The transmission electron microscopy (TEM) micrograph and diffraction pattern from Ni_4Ti_3 precipitates after aging at 500 °C are shown in Figure 1.7. The morphology of the precipitates are lenticular and diffraction pattern shows the characteristic $\frac{1}{7}\langle 321\rangle$ diffraction spots denoted by the arrows. It is worth to mention that the size of precipitates, interparticle distances and volume fraction of precipitates are function of aging time and temperatures. Although, the change in precipitates characteristics could lead to series changes in shape memory and mechanical properties.

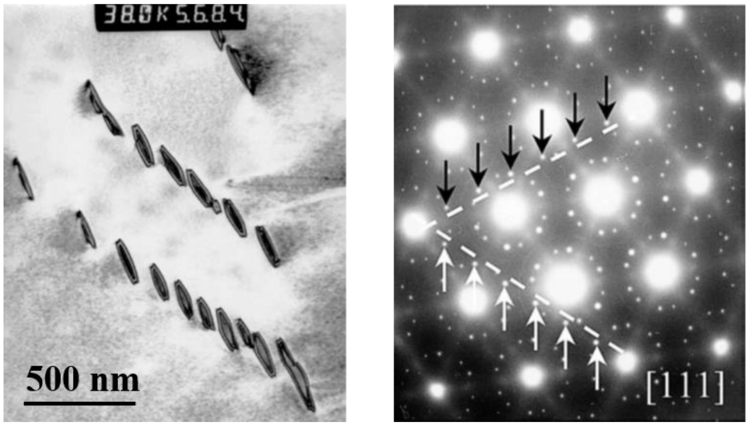

Figure 1.7: TEM micrograph and diffraction pattern from Ni_4Ti_3 precipitates [17].

There are several competing mechanism that affect the TTs and strength of NiTi which are related to size of precipitates and space between them. The general mechanism is the chemical effect of precipitation where the Ni-rich precipitates that are formed remove Ni content from the matrix, therefore, TTs are shifted to higher temperatures [48]. The Ni concentration in the NiTi matrix between two growing precipitates with large interparticle distance could be different which results in broadening the transformation peaks due to inhomogeneity of the composition between the large particles [48]. Another mechanism is related to the local stress fields around the precipitates. The TTs will increase when the stress fields are oriented correctly to nucleate the martensite and enough space is provided between particles for nucleation of martensite. However, the stress fields around the fine precipitates with small interparticle distance generates obstacles and resists the martensitic transformation, therefore, undercooling is required to creates high enough driving force for nucleation and propagation of martensite [60, 61].

In addition to TTs, hardness, an indicative parameter of material strength, has a complex dependence on the size and distance between the precipitates [5, 13]. The critical stress for plastic deformation increases by forming densely distributed fine precipitates which acts as an obstacle against dislocation motion. In other word, the stress field created by the precipitates interact with stress fields of dislocation, resisting plastic deformation and increase the strength of material. Fine precipitates are sheared by dislocation cutting through them which new interface between precipitates and matrix is produced and increased the interfacial energy, hence, the strength of material improved. In the case of bigger precipitates with longer interparticle distances, dislocations could bypass the precipitates by looping around them instead of cutting through them which diminish the strength of the alloy [62]. It has been also demonstrated that the strength of NiTi SMAs improves with increasing Ni content where the austenitic yield stress at room temperature is almost twice higher in in NiTi with 50.4 at. % Ni in compared to the one containing only 49.4 at. % Ni [57].

Repeatable superelastic behavior during cyclic load/unloading in NiTi was first reported in early 1980s where complete recoverable superelastic strain up to 5-8% was achieved [63, 64]. Mechanical behavior of NiTi SMAs is highly test temperature, composition and heat treatment dependent. The effects of deformation temperature on stress-strain curves of $Ni_{50.6}Ti_{49.4}$ (at. %) is shown in Figure 1.8. It is clear that the deformation at lower temperatures is accomplished by reorientation of self-accommodated twins and the growth of some martensite variant at the expense of others which as described before this process known as detwinning. This deformation is different from deformation induced by dislocation or twins and corresponds to Figure 1.8 (a)-(i). At temperatures above A_f, the alloy exhibit complete recoverable superelastic strain up to 4% as demonstrated in Figure 1.8 (j)-(l). As expected from the CC relation (Equation 1.3), the critical stress required to induce martensitic transformation in this temperature range showed in curves (m)-(p) became so large that the plastic deformation by the movement of dislocations occurs simultaneously with the formation of stress induced martensite.

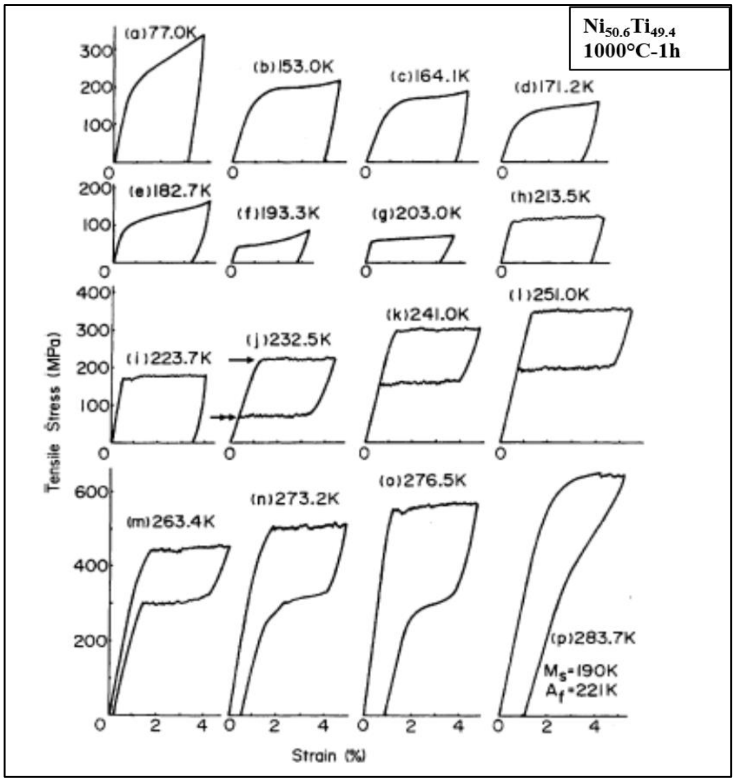

Figure 1.8: Stress-strain curves of $Ni_{50.6}Ti_{49.4}$ as a function of temperature [64].

Figure 1.9 depicts the tensile behavior of NiTi as function of composition and aging. The reverse transformation temperatures are shown in the parentheses and they decrease with Ni content while increase with aging. The samples with different Ni concentration were heat treated at 400 °C and tensile tested at 37 °C. It is obvious from Figure 1.9a that the critical stress to induce martensitic transformation increases with Ni content due to decrease of TTs with Ni concentration. As mention previously, the deformation behavior of SMAs depend on TTs and test temperature where SME was observed for the NiTi alloy containing 50 at. % Ni while almost perfect superelasticity was obtained as Ni content increased to 50.9 at. %. In other hand, TTs increase with aging temperature and perfect superelasticity was observed for $Ni_{50.9}Ti_{49.1}$ alloy as shown in Figure 1.9b. It is worth to mention that the decrease in critical stress to induce martensitic transformation with aging is correlated to TTs and test temperature (37 °C) where more stress needed to initiate martensitic transformation as the difference between A_f and test temperature get larger since the austenite phase become more stable at higher temperatures.

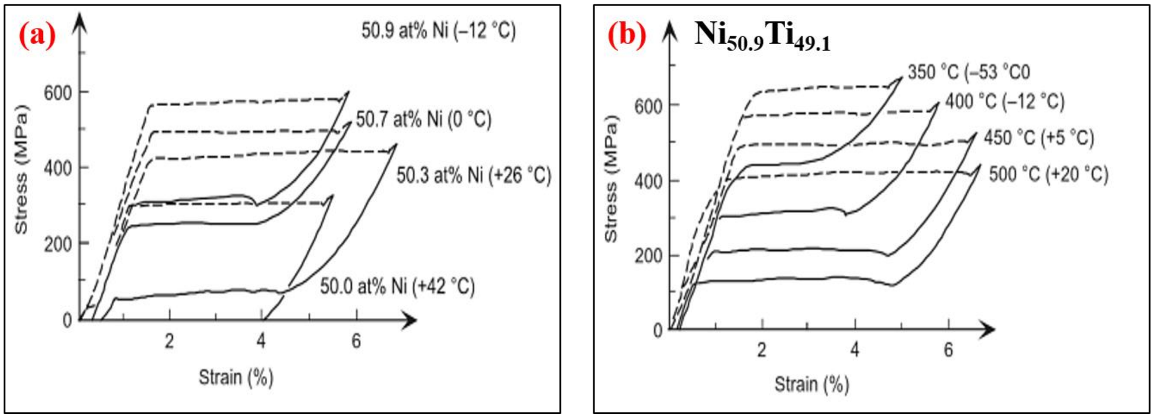

Figure 1.9: Stress vs. strain behavior of NiTi as function of (a) Ni content and (b) aging [65].

Mechanical behavior of NiTi SMAs depend not only on the composition and aging, but also on direction of applied stress. It means that the shape memory behavior can be different in tension, compression and torsion. Tension testing methods and parameters of SMAs are identified in ASTM-E8-”Standart test methods for tension testing of metallic materials”. Figure 1.10 shows the tension, shear and compression behavior of NiTi. It is clear that the flat stress-plateau, (Lüders-like deformation) is observed in tension and torsion but not in compression. Also, the maximum achievable stress after 6% deformation is ~800 MPa under compression while is lower than 200 MPa for tension and torsion. The asymmetry in the mechanical behavior of SMAs is related to the difference in deformation mechanisms during phase transformation and the martensite morphology. As an example, it is known that variant-variant interaction is more pronounced and detwinning is more difficult under compression, resulting in higher stress-strain slope during transformation and lower transformation strain. Furthermore, observed twinning types can also be different. It is important to note that the most common twinning type observe in NiTi alloys is <011> type II [66]. It has been observed that the twinning type can be mixture of type I and type II while a combination of type I and <001> compound twins were also observed after proper cold rolling [67].

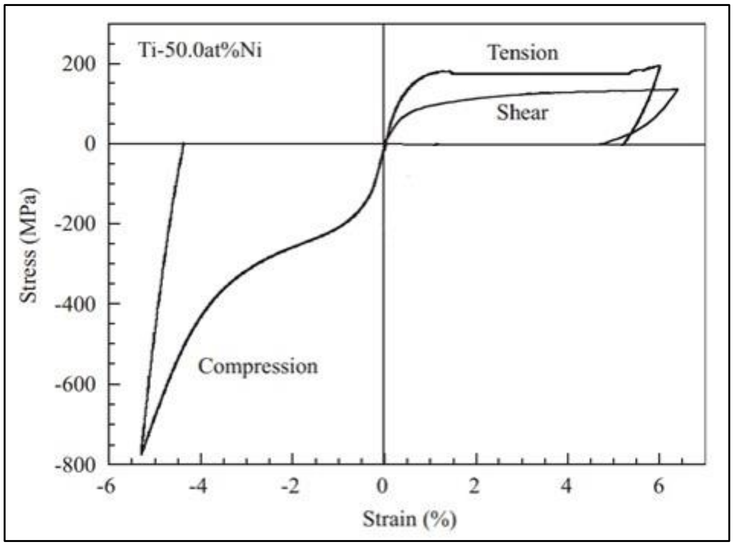

Figure 1.10: Deformation behavior of NiTi shape memory alloys under tensile, compressive and shear stress [68].

It is known that shape memory (transformation strain, hysteresis, CC slope) and material properties (critical stress for slip, ductility) of NiTi SMAs are highly orientation and heat treatment dependent [19, 69, 70]. Figure 1.11a demonstrates the stress-strain responses of aged $Ni_{50.8}Ti_{49.2}$ alloys as a function of crystallographic orientation in compression. The highest recoverable compressive strain, about 9%, was observed along the [148] orientation while recoverable compressive strains were 8%, 4.8% and 3% along the [001], [112], and [111] orientations, respectively. It is clear that [111] and [112]-oriented single crystals exhibit high stress-strain slope during the martensitic transformation due to the formation of multiple correspondent variant pairs (CVPs) while [001] and [148]-oriented single crystals exhibit plateau-like behavior. The orientations with high stress-strain slope in plateau region quickly reached the critical stress for plastic deformation, therefore, their transformation strain and superelastic temperature window is limited [19, 70]. In addition, the CC slopes of aged $Ni_{51.5}Ti_{48.5}$ are 9.3 and 7.5 MPa/ ºC for [111] and [110] orientations [70] , respectively, while for equiatomic NiTi polycrystalline alloys are approximately 12 MPa/ °C in compression [71] and 5–8 MPa/ °C in tension [72].

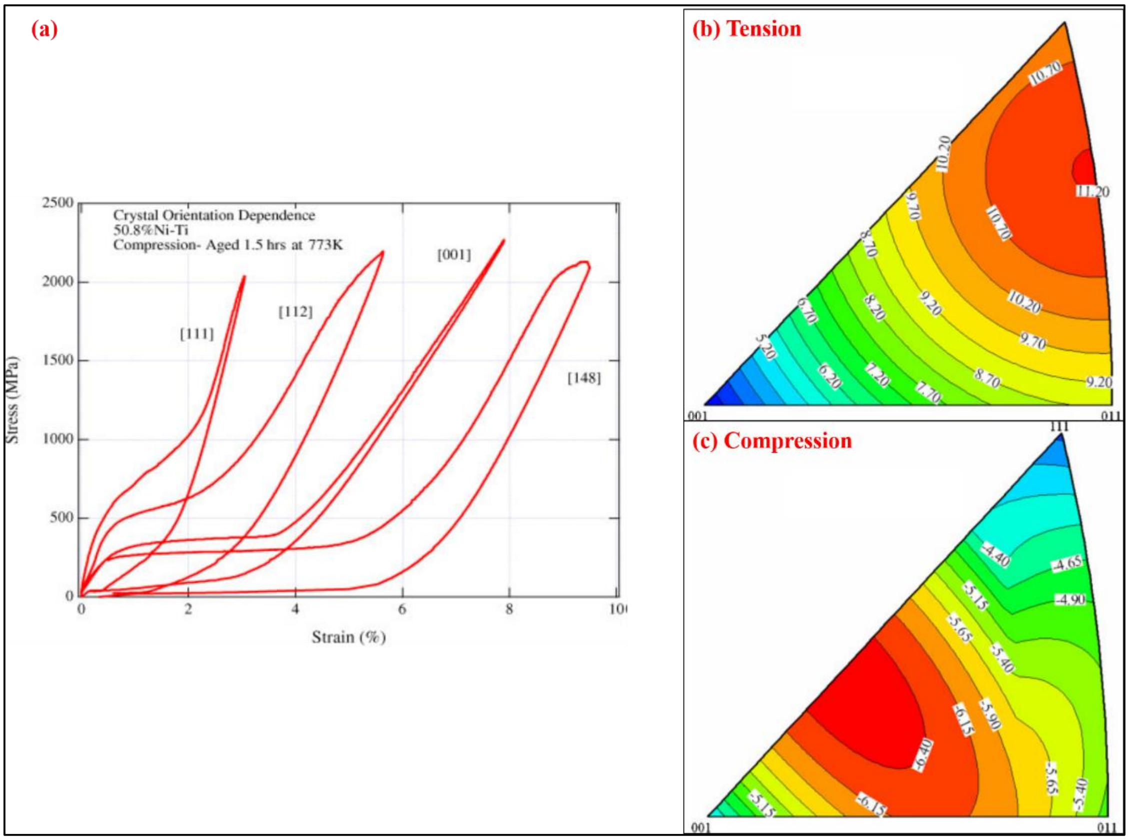

Figure 1.11: (a) Superelastic behavior of NiTi SMA as a function of crystal orientation as a function of the crystallographic orientation [5] and (b, c) crystal orientation dependence of maximum theoretical transformation strain under tension and compression [73].

In single crystal, it is possible to calculate the *resolved shear stress factor* (RSSF) for each variants based on the orientation relationship between the direction of the applied stress and a particular habit plane, which described by its unique habit plane normal and transformation shear direction. The more likely variants that will be activated/favored are the ones with the greatest RSSF value. It is also known that the stress induce martensitic transformation (σ_{SIM}) at lower stress level and transformation strain is higher for orientation with larger RSSF. For instance in NiTi, the [001] has lower σ_{SIM} and larger recoverable strain than [111] direction under compression (Figure 1.11) where the RSSF values are about 0.4 and 0.27 for [001] and [111] orientations under compression, respectively [70].

Similarly, it is possible to calculate the maximum transformation strain along the certain crystallographic orientation. General approaches for such calculations are the Energy Minimization Theory [74] and the Lattice Deformation Theory [75]. The energy minimization theory considers the existence of the invariant plane (habit plane) between austenite and martensite phases while the lattice deformation theory assumes that the austenite transforms into a single crystal of martensite without twins and does not consider the existence of habit planes. Transformation strain has a theoretical limit, which is dependent on the lattice parameters of transforming phases, type of twinning systems and crystal orientation or texture [76]. These calculation can be performed for all orientation under different applied stress-states and plotted as transformation strain contours as long as the lattice parameter and crystal structure of transforming phases are known. Theoretical transformation strain contours under tension and compression are shown in Figure 1.11b and c, respectively. Also, the maximum transformation strain calculated by using energy minimization theory, RSSF and experimental recoverable strain for the $<011>_{B19'}$ type II twin, which is the dominant twinning mode observed in martensite plates [77], are summarized in Table 1.1. It is clear that single crystal orientations along which external stress is applied have a significant on maximum RSSF and transformation strains. It has been reported in Ref. [69, 78, 79] that the [111]-oriented NiTi alloys are characterized as soft under tension since it demonstrated large transformation strain and low critical transformation stress levels. Conversely, the [001]-oriented NiTi revealed small transformation strain and stress induced transformation at a significantly higher stress under tension which is categorized as hard orientation. However, [111] orientation is hard and the [001] orientation is soft under compression. Thus, tension and compression loading favor different martensite variants and degree of detwinning, and consequently, lead to remarkably different transformation strains.

Table 1.1: Maximum theoretical strain, RSSF and experimental strain of NiTi under tension and compression.

	NiTi <011> type II					
	Compression			**Tension**		
	RSSF	CVP strain	$\varepsilon_{experimental}$	RSSF	CVP strain	$\varepsilon_{experimental}$
[001]	0.40	5.20%	> 5%	0.21	2.70%	> 2%
[011]	0.37	4.80%	> 4%	0.41	5.30%	≥ 6.5%
[111]	0.27	3.50%	≥ 3%	0.39	5.10%	> 7.5%
polycrystalline			> 3%			≥ 5.5%

It is reasonable to expect that the shape memory and superelastic behavior of SMAs depend on the orientation distribution of the grains in the material which know as texture. Texture can be introduced by thermomechanical processing, such as cold rolling or equal channel extrusion, and the specimen can be cut at certain angles to achieve strong texture close to the orientation exhibiting the best sets of shape memory and material properties. Polycrystalline SMAs with strong texture in a particular orientation would be expected to have similar behavior as a single crystal of that orientation. Thus, investigation of the shape memory properties of SMA single crystals is important since the shape memory properties could be optimize by texturing in a polycrystalline materials. It has been reported that the major texture in cold rolled NiTi is along the {110} orientation [78, 80].

NiTi has many properties desirable for low temperature actuator and superelastic components such as small hysteresis, high work output, stable microstructure and excellent corrosion resistance [57]. Although, the TTs can be adjusted by changing the stoichiometry of NiTi binary alloys or formation of precipitates but the temperature does not increase enough in order to be considered as a candidate for high temperature (above 100 °C) applications. The development of a shape memory material with properties similar to those of near equiatomic NiTi, but with higher strength and higher transformation temperatures, especially above 100 °C, is direly needed for a broad range of applications in the aerospace, automotive and oil & gas industries. The main interest is to use HTSMAs as solid state actuator since have many advantage, such as being more energy efficient, light weight and frictionless, as compared to hydraulic, pneumatic and any other mechanical driven systems [3]. Ternary element addition to NiTi alloys is the most promising method to obtain commercially available HTSMAs in the near future [5]. Ternary element addition should not only increase the TTs, but also help maintain the good mechanical properties of NiTi alloys. It has been found that the addition of Hf, Zr, Pd, Pt and Au elements to NiTi increases its TTs [3, 4]. It is worth to mention that Pd and Pt both substitute for Ni in the NiTi systems since they belong to the same family as Ni in the periodic table and for the same reason, Hf and Zr substitute for Ti in the NiTi alloys. Figure 1.12 shows the influence of the third element on TTs where the M_s or martensite peak temperature (M_p) linearly increase as the alloying element is above 10 at. %. Detailed investigation on shape memory properties other than increase of TTs with addition of Au has not been completed [81-84], therefore, a larger focus will be placed on the addition of Pd, Pt, Zr and Hf to NiTi.

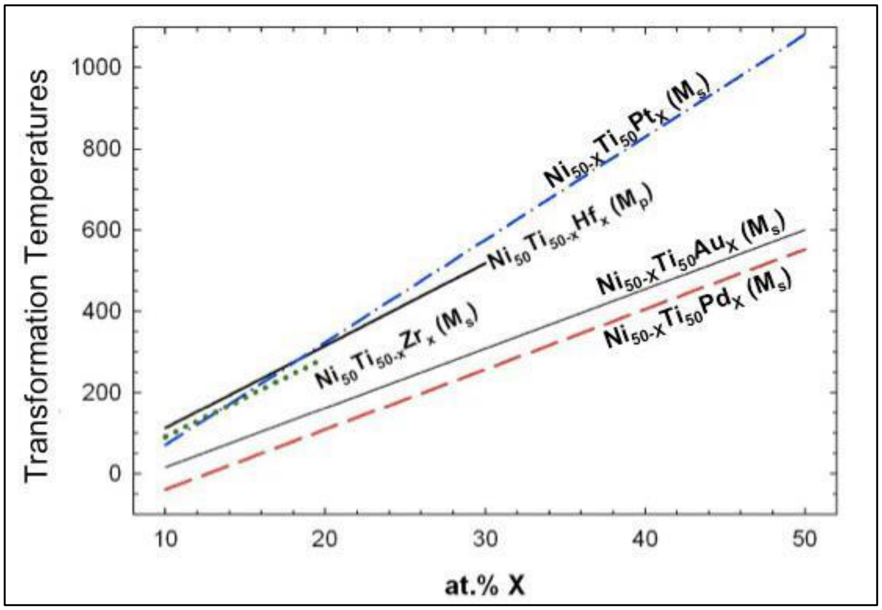

Figure 1.12: Dependence of transformation temperature on the content of third element [3].

1.4.2 NiTi (Pt, Pd, Zr) Systems

As mentioned before, Pd and Pt preferentially substitute for Ni in NiTi and change the transformation behavior. The benefits of NiTiPt alloys include increasing TTs up to 1000 °C (Figure 1.12), high work output and the ability to recover 3-4% strain [57, 85]. These properties, along with high yield strength [3] outweigh the high cost of Pt. In NiTiPt system, the alloy transform into the B19' martensite upon cooling from high temperature phase while two stage transformation of $B19' \rightarrow R \rightarrow B2$ occurs during reverse transformation when the concentration of Pt is lower than 10 at. %. However, for higher concentration of Pt (greater than 16 at. %), single step transformation of B2↔B19 takes place during cooling and heating [5, 85]. Furthermore, NiTiPt systems with Pt concentration greater than 30 at. % have drawbacks such as large thermal hysteresis and poor tensile ductility [86], thus, Pt is constrained to be less than 30 at. % for optimal balance of functional and structural properties.

NiTiPd has been studied as a promising SMAs for high temperature application since it has lower cost than Pt and Au, and also the M_s can be increased to above 500 °C for 50 at. % (Figure 1.12) [81]. At lower concentrations of the Pd (less than 10 at. %), two stage transformation of B2→R→B19' observe upon cooling while single step transformation of B19'→B2 occurs during heating. However, martensite structure change to B19 as Pd concentration becomes greater than 10 at. %. Similar to NiTi, the TTs drop rapidly with increasing the (Ni+Pd) concentration to more than 50 at. % while the shape memory properties improve due to presence of precipitates [87].

Goldberg et al. [15, 16] reported that the shape memory properties of $Ti_{50}Ni_{20}Pd_{30}$ HTSMAs improved remarkably after thermomechanical processing, which consisted of cold rolling up to 25% reduction in thickness and subsequent annealing at 400 °C for 1h. This treatment increased the yield strength of the martensite phase from ~200 to 400 MPa at 170 °C. Also, recoverable strain significantly improved, as 5.3% applied strain was fully recovered (under stress free conditions) when the samples were heated above the A_f in comparison to the mere 2.5% strain recovered for the solution treated alloy after tensile deformation at 170 °C. In addition, a type of linear superelastic behavior was reported for the first time in a NiTiPd alloy due to the thermomechanical treatment (cold working followed by annealing).

In studies on precipitation process showed that NiTiPt systems have precipitates similar to those of binary NiTi where the $Ti_2(Ni,Pt)_3$ phase was found on the (Ni+Pt) rich side of stoichiometry and $Ti_2(Ni,Pt)$ phase was found on the Ti-rich side of the stoichiometry [5]. However the alloy with composition close to stoichiometric illustrated a different precipitate phase than NiTi during aging which referred to as P-phase ($Ti_{11}Ni_9Pt_4$). The TEM micrographs and SAD pattern of P-phase is shown in Figure 1.13. The characteristic $\frac{1}{7}\langle 321\rangle_{B2}$ diffraction spot of Ni_4Ti_3 are not present in the SAD pattern of the $[111]_{B2}$ zone in Figure 1.13b. The precipitates in NiTiPd have a structure similar to the P-phase found in the NiTiPt system.

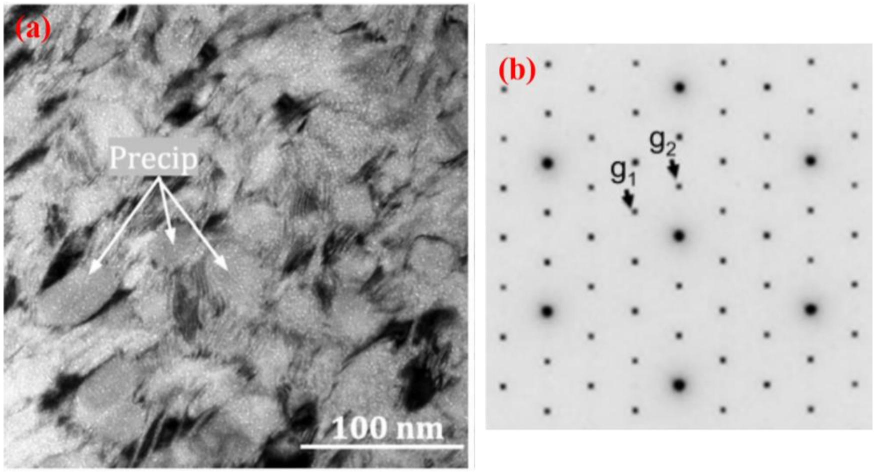

Figure 1.13: (a) TEM micrograph of precipitates after 500 °C-4h aging of $Ni_{20}Ti_{50}Pt_{30}$ and (b) SAD pattern of the P-phase precipitates [88].

Alloying Zr to NiTi was investigated due to its lower cost in compared to Pd and Pt. Similar to previously discussed HTSMAs, the concentration of Zr in NiTiZr alloys change the transformation process. When concentration of Zr is lower than 20 at. %, B2 transforms to B19’ during cooling, whereas at higher concentration of Zr (greater than 20 at. %) the martensite structure changes to B19 [5, 89]. The main issue of NiTiZr alloy is their low stability during cycles of transformation where TTs do not stabilize after 100 thermal cycles while as other SMAs would stabilize after a few cycles [89]. Although, there are not that many studies on mechanical behavior of NiTiZr but they can still be useful for microstructural analysis since the precipitates phases are similar to NiTiHf alloys which will be discussed in next section.

1.4.3 NiTiHf Systems

It is known that the elements Pd, Pt, and Au are very expensive and will limit the use of their respective ternary alloys to some critical applications only (i.e., aerospace) where performance is much more important than the cost, while Zr is associated with high oxygen affinity [3, 4]. Among the potential HTSMAs, NiTiHf seems to be the most promising HTSMA for a wide range of applications in the critical 100-300 °C temperature range due to its low cost, excellent shape memory properties and high work output [5]. It was also reported that Hf had a greater influence on TTs than Pd and Au for an equivalent concentration [4, 8, 90].

As mentioned previously that the TTs of NiTi based SMAs are highly composition dependent [5, 91], including the NiTiHf alloys [11, 92]. The transformation temperatures of NiTiHf alloys do not increase much up to 10 at. % Hf content, however, at chemical concentrations higher than 10 at. %, they tend to increase linearly up to 525 °C for 30 at. % Hf when Hf is added at the expense of Ti [11, 92]. Figure 1.14a shows the change in M_p (martensite peak temperature) as a function of Hf [11, 92, 93]. It is clear that M_p does not change up to 3 at. % addition of Hf and then increases after 5 at. %. Up to 10 at. % Hf, the increase of M_p is about 5 °C/at. % Hf. As the Hf increases beyond 10 at. %, there is an abrupt increase of M_p by almost 20 °C/at. % Hf in NiTiHf alloys and M_p reaches up to 400°C for 25 % Hf. Figure 1.14b shows the effect of Ni content on the M_p in NiTiHf alloys containing 10 at. % Hf. It is clear that M_p is not sensitive to Ni concentration up to 50 at. % and then drastically decreases to below 0 °C with Ni content.

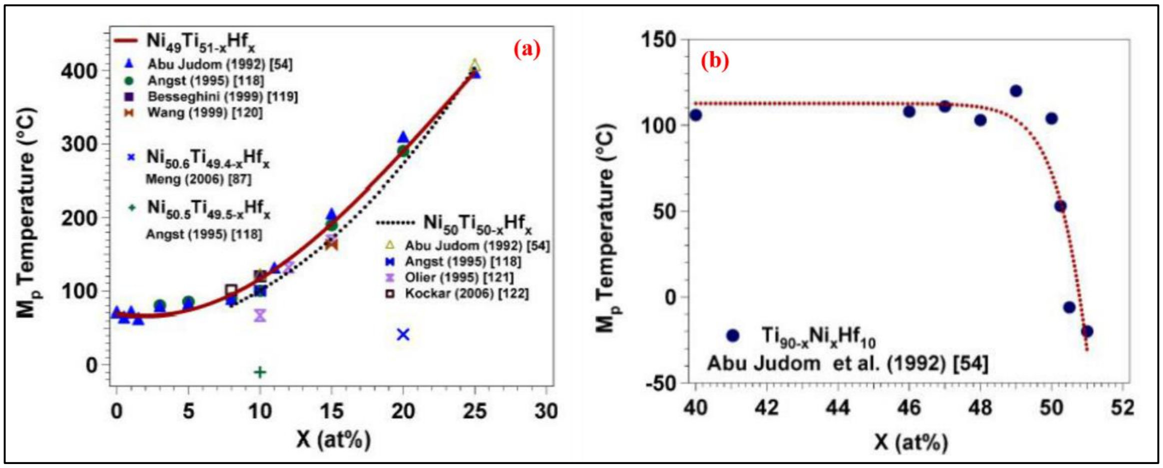

Figure 1.14: Dependence of Mp temperature on (a) Hf and (b) Ni concentration of NiTiHf [5].

In general, the crystal structures of austenite and martensite phases in NiTiHf alloys are cubic B2 and monoclinic B19′, respectively, which are similar to those in NiTi binary alloys. Zarinejad et al. [94] investigated the effect of Hf on the lattice parameters of the B19' martensite in NiTiHf alloys. The lattice parameters *a*, *b*, *c* and β angle of the martensite are plotted in Figure 1.15 as a function of Hf content for $Ni_{(100-x)/2}Ti_{(100-x)/2}Hf_x$, $Ni_{50-x}Ti_{50}Hf_x$ and $Ni_{50}Ti_{50-x}Hf_x$ (x = 5-20 at.%) alloys. The addition of Hf increased all the lattice parameters for the $Ni_{(100-x)/2}Ti_{(100-x)/2}Hf_x$ and $Ni_{50-x}Ti_{50}Hf_x$ alloys. On the other hand, when Ni is constant, the increase of Hf in the $Ni_{50}Ti_{50-x}Hf_x$ alloy increased *a*, *c* and β but decreased *b*. Potapov et al. [95] also observed a similar dependence of lattice parameters on the Hf content for $Ni_{49.8}Ti_{50.2-x}Hf_x$ (x = 8-25 at.%) alloys where the increase of Hf while Ni was kept constant to 49.8% slightly decreased the lattice parameter *b*, while it increased *a*, *c* and *β* of B19’ martensite. It was also reported that the addition of Hf increased the lattice parameter of B2 austenite [95]. The volume change during transformation was smaller than 0.5% which was similar to that in NiTi binary alloys (~0.3% or less) [96, 97]. It should be noted that in some studies, NiTiHf alloys with more than 15 at. % Hf in $Ni_{48.5}(Ti_{51.5-x}Hf_x)$ [98] and between 20 and 30 at. % Hf of $Ni_{50}(Ti_{50-x}Hf_x)$ [99] were reported to have orthorhombic B19 martensite.

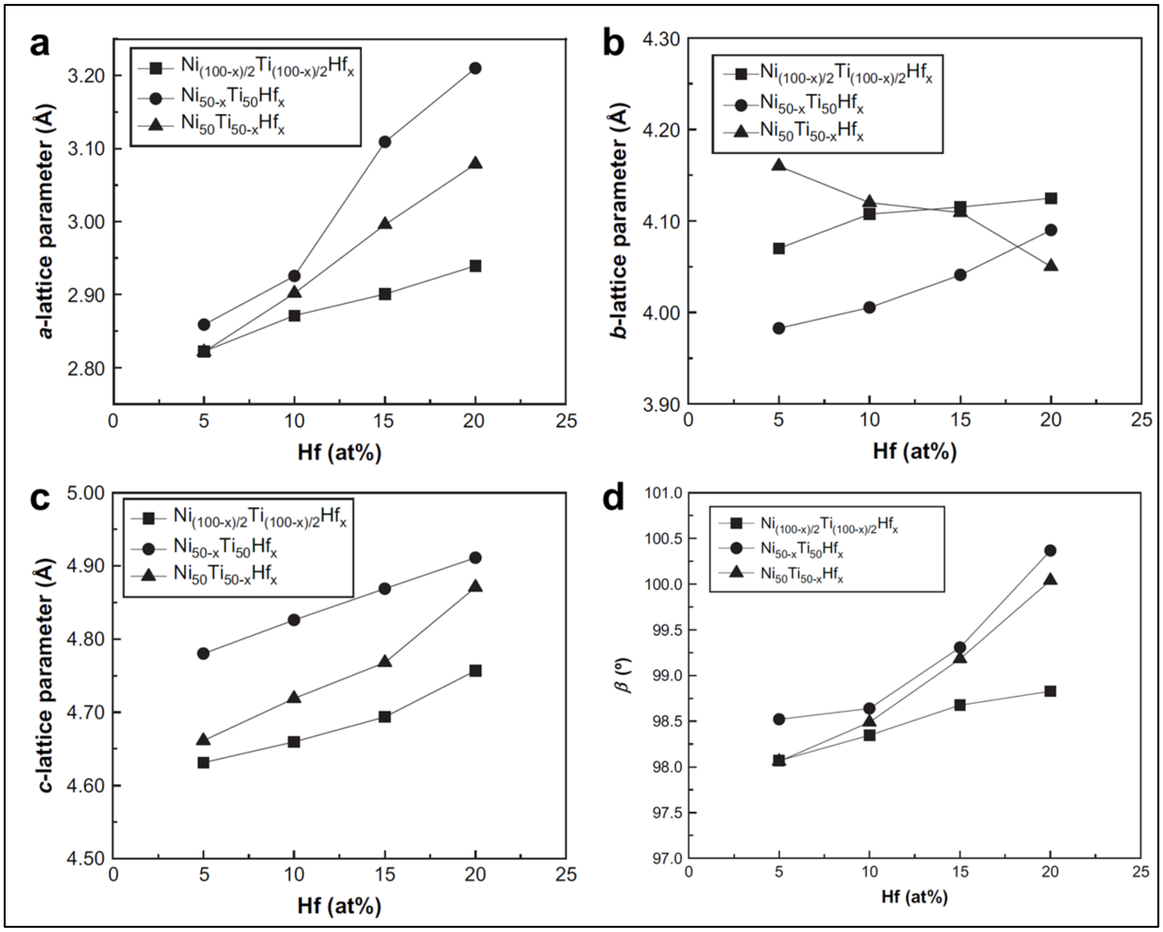

Figure 1.15: Lattice parameters (a) *a*, (b) *b*, (c) *c* and (d) *β* of B19′ martensite as a function of Hf in NiTiHf alloys [94] (Chemical compositions are in at. %).

Most HTSMA research was focused on (Ti+Hf)-rich NiTiHf alloys due to the low TTs of Ni-rich materials. However, the main disadvantages of (Ti+Hf)-rich NiTiHf alloys are their large hysteresis (> 50 °C), poor ductility at room temperature, lack of cyclic stability due to the high stress for the reorientation of martensite and detwinning, the low strength for slip and poor formability [3, 8]. Previously, Meng et al. [12] examined the tensile properties of (Ti+Hf)-rich NiTiHf alloys and did not observe a stress plateau at room temperature but rather observed continuous yielding with high work hardening, which can be attributed to the high resistance to martensite reorientation and the low stress needed for plastic deformation. To increase the resistance to dislocation slip, Kockar et al. [8] employed severe plastic deformation of (Ti+Hf)-rich NiTiHf alloys and reported an increase in the recoverable strain and a decrease in the irrecoverable strain levels under isobaric thermal cycling experiments. They also found that thermal cyclic stability improved and thermal hysteresis decreased. However, the large thermal hysteresis prevented the observation of a reversible superelastic response [8].

Unfortunately, the majority of prospective HTSMA systems are ordered intermetallic with limited ductility at low and intermediate temperatures, making it difficult and expensive to apply thermomechanical processing techniques to increase the material's strength. Thus, precipitate hardening becomes a more viable method for increasing the strength of difficult-to-work alloys. The precipitates act as obstacles in the path of dislocations, which must then either cut through the precipitate or bypass it to proceed. Of course, the strengthening ability of the precipitates depends on the size, volume fraction, interparticle spacing, and coherency of the second phase.

König et al. [100] fabricated NiTiHf thin films with a wide composition range by magnetron sputtering method and investigated their TTs, precipitate structure and thermal cycling properties. Multilayer thin films (individual layers ~15 nm thick) were sputtered from elemental targets and annealed at 550 °C for 1h in order to transform their multilayer structure into alloys. Figure 1.16 depicts the composition regions in which different precipitates are formed [100]. The relative intensity of one characteristic XRD peak belonging to the phase of interest was plotted color-coded within a section of the NiTiHf ternary phase diagram. Four different precipitates, i.e. HfNi(Ti), Ti_2Ni(Hf), Hf_2Ni(Ti) and Laves phase, were confirmed in (Ti+Hf)-rich composition regions. They concluded that the observation of reversible phase transformation was limited by the formation of Ti_2Ni(Hf), HfNi(Ti) and/or Hf_2Ni(Ti) precipitates. These precipitates restricted the transforming region to compositions with Ni contents above ~40 at. % and Hf contents below ~30 at. %.

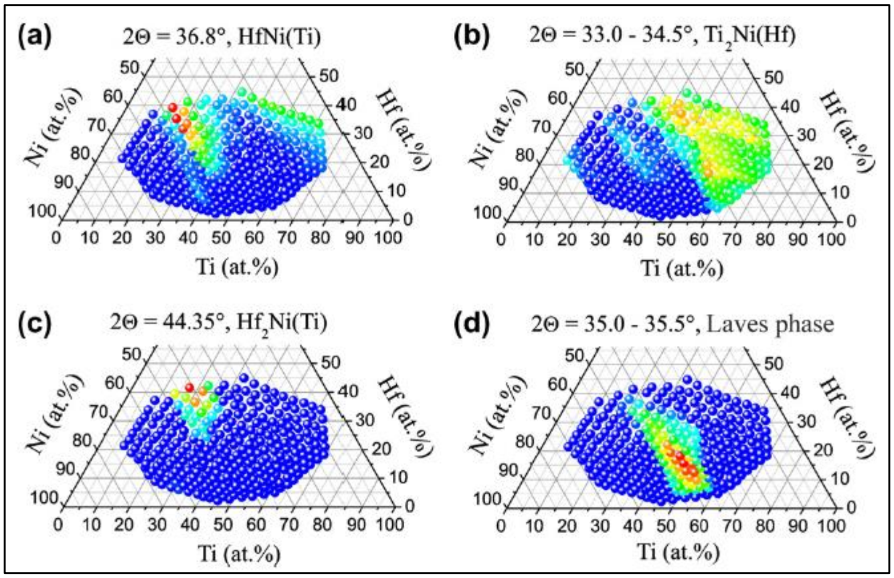

Figure 1.16: Composition regions in which different precipitate phases exist. The relative intensity of an X-ray diffraction peak for each phase is plotted color-coded within a section of the ternary Ni-Ti-Hf diagram for (a) HfNi(Ti), (b) Ti_2Ni(Hf), (c) Hf_2Ni(Ti), (d) Laves phase (Color code: red = high; green = medium; blue = low intensity.) [100].

The $Ti_2Ni(Hf)$ precipitates have also been observed by many other researchers in Ni-lean NiTiHf alloys [12, 101-104]. It has been reported that the volume fraction of the $Ti_2Ni(Hf)$ precipitates decreased with increasing the Ni content, although the $Ti_2Ni(Hf)$ precipitates were still observed in slightly Ni-rich compositions [91, 101]. Fine $Ti_2Ni(Hf)$ precipitates strengthen the matrix and improve shape memory and superelastic properties of NiTiHf-based alloys [12, 102]. It is important to note that the size of the $Ti_2Ni(Hf)$ precipitates are very effective to control the martensite morphology. It was found that $(001)_{B19'}$ compound twins were dominant when the material contained homogeneously distributed $Ti_2Ni(Hf)$ precipitates with 20–40 nm in diameter (Figure 1.16a). Similar martensite morphology has been observed in a Ti-rich NiTi thin film with a homogeneous distribution of fine Ti_2Ni precipitates [105]. Martensite domains with $(001)_{B19'}$ compound twins were also observed around the coarse $Ti_2Ni(Hf)$ precipitates. The spear-like and mosaic-like morphologies have been reported as typical morphologies of the martensite in Hf-added NiTi alloys [106, 107].

Meng et. al. [91] revealed that it was possible to form $(Ti,Hf)_3Ni_4$ precipitates in Ni-rich NiTiHf alloys and in the process restore TTs to a higher temperature. They also reported that these coherent precipitates increased the matrix strength and enhanced the thermal stability of the alloy [91, 108]. However, recently, it has been reported that a new precipitate which has a more complicated structure than that of $Ni_4(Ti,Hf)_3$ forms in Ni-rich NiTiHf alloys [109-111] and improves their shape memory and superelastic properties due to precipitation strengthening [112-114]. Initially, Han et al. [115] reported a precipitate with a face-centered orthorhombic lattice with a space group of F 2/d 2/d 2/d in an aged $Ni_{48.5}Ti_{36.5}Hf_{15}$ alloy. There are six different variants in this orthorhombic precipitate with habit planes of $(100)_P//\{001\}_{B2}$ and long axes of $[001]_P//<\bar{1}10>_{B2}$. However, they did not provide an atomic structure model for the observed precipitate.

Recently, Yang et al. [111] proposed an atomic structure model which contains of 192 atoms in an orthorhombic unit cell for the observed precipitate in Ni-rich NiTiHf alloys. The orthorhombic precipitate phase was named as “H-phase” and Figure 1.17a shows the unit cell of this precipitate [111]. In order to refine the structure model, ab initio density functional theory (DFT) calculations have also been performed to relax the structure model [110, 111]. SAD patterns obtained from a single large H-phase precipitate in a $Ni_{52}Ti_{28}Hf_{20}$ alloy are shown in Figures 1.17b-d [111]. All the SAD patterns revealed the orientation dependence between the precipitate and austenite B2 phase (the diffraction spots are indexed according to the austenite phase). There were additional reflections at 1/3 positions along $<110>_{B2}^{*}$ in reciprocal space as shown by arrows, which was a characteristic of the H-phase. The composition of the proposed H-phase was $Ni_{50}Ti_{16.7}Hf_{33.3}$, whereas it has been indicated by EDS analysis that the Ni content of the H-phase precipitate was always slightly richer than that of the nominal composition of Ni-rich NiTiHf alloys in contrast to the proposed Ni content of 50 at. % [110, 111, 116]. Therefore the formation of H-phase precipitates depleted Ni from the matrix and increased TTs. Yang et al. [111] observed anti-site defects within the precipitate which may slightly change the composition of the precipitate, and proposed that the H-phase did not have a unique composition. The effects of the alloy composition on the H-phase precipitation was investigated by Santamarta et al. [110]. They concluded that the H-phase precipitates grew faster in alloys with higher Ni content since the precipitates were richer in Ni content compared to the nominal composition of the alloys. Similarly, for a fixed Ni content, the growth of the H-phase became faster when the Hf content was increased.

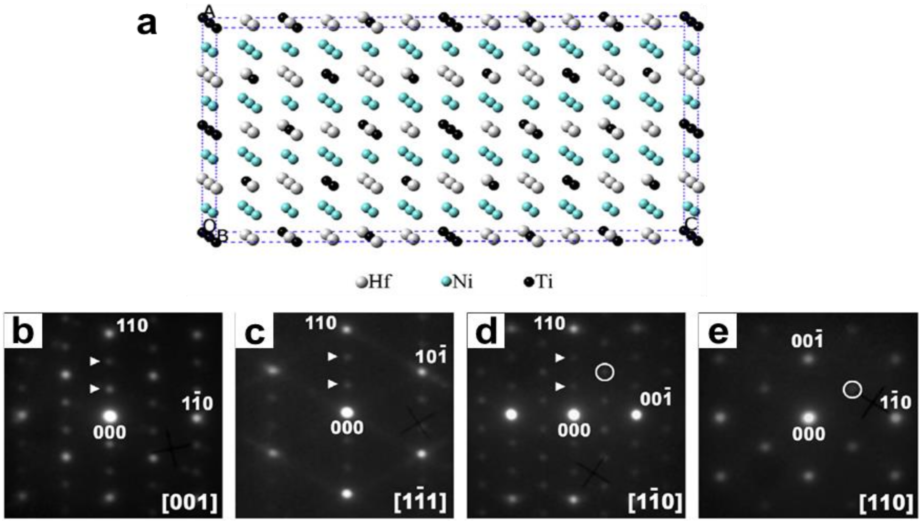

Figure 1.17: (a) Unit cell of unrelaxed orthorhombic model of the H-phase [111]. SAD patterns of the (b) $[001]_{B2}$, (c) $[1\bar{1}1]_{B2}$, (d) $[1\bar{1}0]_{B2}$ and (e) $[110]_{B2}$ zone axes obtained from a single large particle in a $Ni_{52}Ti_{28}Hf_{20}$ alloy [110]. The small arrows and circles mark the additional reflections arising from the precipitate.

The control of the size and interparticle distance of H-phase precipitates is important to obtain good shape memory and superelastic responses. It has been reported that the aging temperature and time significantly affected the size and interparticle distance of the precipitates formed in Ni-rich NiTiHf-based alloys [91, 110, 112]. Figures 1.18a-c illustrates the representative microstructure of $Ni_{50.3}Ti_{29.7}Hf_{20}$ alloys in as-extruded and aged conditions [114]. The bright-field image of the as-extruded $Ni_{50.3}Ti_{29.7}Hf_{20}$ alloy is shown in Figure 1.18a. Precipitate formation was not confirmed in the as-extruded condition. Figures 1.18b and c show TEM micrographs of the extruded $Ni_{50.3}Ti_{29.7}Hf_{20}$ alloy aged at 550 °C and 650 °C for three hours, respectively. Fine and coherent H-phase precipitates were formed in the 550 °C aged specimen. When the aging temperature increased from 550 to 650 °C, the precipitate size increased from about 20 nm to 40–60 nm. The interparticle distance also increased after three hours aging at 650 °C compared with the 550 °C-3h case.

The martensite morphology in Ni-rich NiTiHf alloys is affected by the size and interparticle distance of H-phase precipitates. The martensite variants in the as-extruded $Ni_{50.3}Ti_{29.7}Hf_{20}$ alloy show spear-like morphology and high density of twins can be seen inside the martensite plates (Figure 1.18a). Han et al. [106, 107] have reported two types of martensite morphologies; spear-like and mosaic-like in NiTiHf alloys and they also revealed that each martensite lath is consisted of $(001)_{B19'}$ compound twins. If the precipitates were small and interparticle distance was short, the growing martensite plates can absorb all the precipitates during growth as it can be seen in the 550 °C-3h aged $Ni_{50.3}Ti_{29.7}Hf_{20}$ alloys (Figure 1.18b). The large martensite plates were related by the $\{011\}_{B19'}$ type I twinning mode, which was confirmed by the SAD pattern shown in Figure 1.18d taken at the interface of the plates. It should be noted that no internal twins were observed in the large martensite plates in the 550 °C-3h aged specimen. On the other hand, when the precipitates were big and interparticle distance was large, martensite plates can be formed between the precipitates and the thickness of the plates was controlled by the interparticle distance of the precipitates (Figure 1.18c). However, Santamarta et al. [110] have also noted that {011} type I twinning was dominant in similar alloys with very fine precipitates and the (001)-compound and {011} type I twinning are more or less equally observed as the precipitates coarsened and martensite was constrained to form between larger particles.

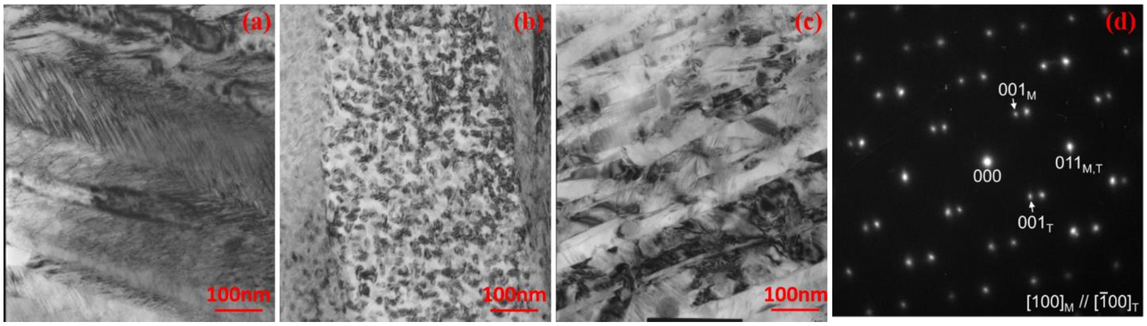

Figure 1.18: Bright-field images of the $Ni_{50.3}Ti_{29.7}Hf_{20}$ alloy (a) extruded at 900 °C, (b) aged at 550 °C for 3h (c) aged at 650 °C for 3h and (d) electron diffraction pattern taken from the martensite variants in (b) [112].

Dalle et al. [117] investigated the interface mobility of the martensite variants in $Ni_{49.8}Ti_{42.2}Hf_8$ after annealing at 800 °C for 1h. They suggested that the interface mobility was low due to distorted habit planes and the high density of fine $(001)_{B19'}$ compound twins inside the martensite. TEM observation was conducted for $Ni_{49.8}Ti_{42.2}Hf_8$ after 10% tensile deformation to investigate the morphology of reoriented martensite. They observed finer $(001)_{B19'}$ compound twins in the deformed material compared to the as-annealed material with self-accommodated martensite. They suggested that the detwinning of the $(001)_{B19'}$ compound twins is difficult and proposed that, instead of the detwinning, a supplementary $(001)_{B19'}$ mechanical twinning could take place during deformation by a mechanism of the repetition of the dislocation slip on the $(001)_{B19'}$ plane. In addition, Meng et al. [118, 119] investigated the morphologies of the stress-induced martensite (SIM) in $Ni_{49}Ti_{36}Hf_{15}$ which were solution-treated at 1000 °C for 1h and deformed in tension at 250 °C. Figure 1.19a shows the typical morphology of the preferentially oriented SIM variants and the SAD pattern taken from the area II for the 8% deformed $Ni_{49}Ti_{36}Hf_{15}$ [119]. $(001)_{B19'}$ compound twins were mainly observed in the SIM plates. The SAD pattern revealed that the SIM plates were twin-related with $\{011\}_{B19'}$ type I mode, which was similar to the thermally transformed martensite [106, 107]. The preferentially oriented SIM variants were disappeared and several martensite variants were intersected into each other after deformation. Figure 1.19b shows the variant-crashed/variant-intersected morphology of the after deformation of 16%. The interfaces of the martensite variants are blurred in the variant-crashed/variant-intersected morphology. They noted that the stress-induced martensitic transformation and dislocation slip occurred simultaneously during loading and suggested that the introduction of dislocations increases the martensite variants with the variant-crashed/variant-intersected morphology.

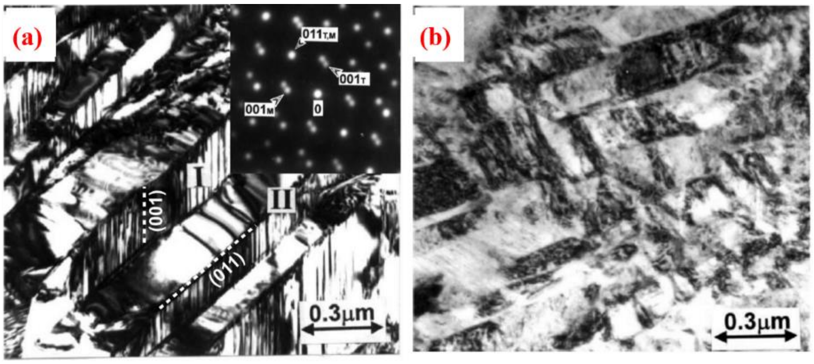

Figure 1.19: Bright-field image of $Ni_{49}Ti_{36}Hf_{15}$ (a) deformed to 8% at 250 °C and (b) deformed to 16% at 250 °C [119]. The SAD pattern shown in (c) was taken from area II.

Initially, properties of Ni-lean NiTiHf alloys were mainly investigated due to low TTs of Ni-rich NiTiHf alloys [91, 108]. SME with 3% recoverable strain or 80% recovery of 6% applied strain is observed in compression and bending [7, 120] while 80% recovery of 2.5% applied tensile strain is observed in $Ni_{50}Ti_{38}Hf_{12}$ produced by powder metallurgy. The poor SME is attributed to high stress (~500 MPa) for martensite reorientation and high work hardening rate (no plateau region observed) confirmed by tensile experiments [120, 121]. Although no superelasticity is observed in Ni-lean NiTiHf alloys [91, 119], 0.88% strain for TWSME has been observed [122]. Unstable cyclic behavior is a major problem in Ni-lean NiTiHf alloys where it has been demonstrated that TTs were decreased by 40 °C during stress free thermal cycling of $Ni_{49}Ti_{41}Hf_{10}$ after 20 cycles [123].

Effects of aging on the SME and superelastic behavior of Ni-rich NiTiHf alloys are shown in Figure 1.20. It is evident from Figure 1.20a that transformation strain was increased above 3% after aging at 550 °C-3h which can be attributed to absorption of precipitates by martensite plates during forward transformation as shown in Figure 1.18b. However, precipitates became larger in size after aging at 650 °C-3 h and growth of martensite variants was limited in the space between precipitates. It is clear that TTs, thermal hysteresis and transformation strain can be tailored by aging. Figure 1.20b shows the superelasticity responses of as extruded and aged $Ni_{50.3}Ti_{29.7}Hf_{20}$ alloys [114]. Perfect superelastic behavior with 4% recoverable strain was revealed at 240 ºC after aging at 550 °C for three hours in $Ni_{50.3}Ti_{29.7}Hf_{20}$. The improvement in superelastic behavior with aging can be attributed to the presence of coherent and fine H-phase precipitates which strengthen the matrix. Poor superelastic response after aging at 650 ºC-3h can be attributed to loss of the coherency of the coarsened precipitates. It is worth to note that beside the fully recoverable strain, Ni-rich NiTiHf exhibited high yield strength at high temperatures and the CC slopes were between 7-13 MPa/ ºC.

Quaternary alloying and precipitation strengthening have also been used to improve the overall behavior of NiTiHf polycrystalline and single crystal alloys. The shape memory properties of heat treated $Ni_{45.3}Ti_{29.7}Hf_{20}Pd_5$ (at. %) alloys in single crystalline and polycrystalline forms have been recently reported [112, 124-127]. The replacement of 5 % Pd with Ni in $Ni_{50.3}Ti_{29.7}Hf_{20}$ alloy resulted in a very high strength alloy that has high damping capacity of 35 J/cm^3 in polycrystalline form [112] and 44 J/cm^3 along [111] oriented single crystals [127]. Transformation strain of 2% was observed in aged [111] oriented $Ni_{45.3}Ti_{29.7}Hf_{20}Pd_5$ single crystals under a compressive biasing stress of 1500 MPa [126]. Moreover, perfect superelastic behavior with recoverable strain of 4.2% was observed in the solutionized condition even when compressive stress levels as high as 2.5 GPa were applied [127]. However, it is also known that $Ni_{45.3}Ti_{29.7}Hf_{20}Pd_5$ alloys are brittle, since they generally fail after limited plastic deformation in compression and during phase transformation in tension in superelasticity experiments [128].

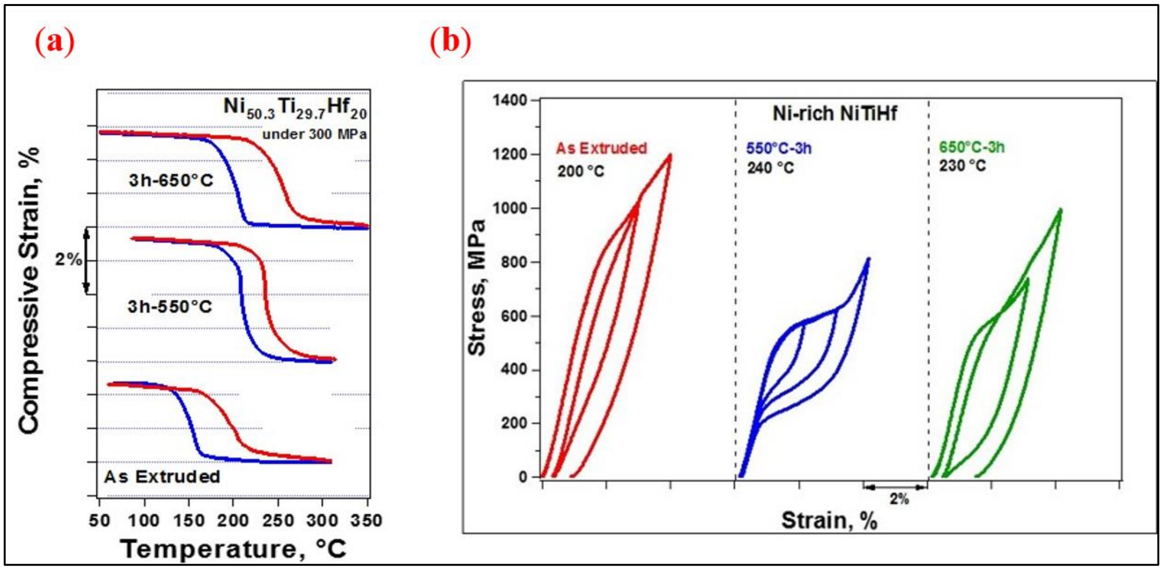

Figure 1.20: Aging effect on shape memory effect (a) and superelastic behavior (b) in $Ni_{50.3}Ti_{29.7}Hf_{20}$ SMAs.

It has been considered that low workability is one of the main problems with NiTiHf alloys for practical use. Kim et al. [129] reported that an addition of Nb to NiTiHf alloys caused the formation of a soft Nb-rich β phase and improved the cold workability, although the TTs and plastic strain in thermal cycling experiments under stress were decreased. Cu has been another alloying element to NiTiHf systems where, in general, it improved the glass forming ability and thermal stability of NiTiHf alloys while decreasing their TTs [102, 130]. NiTiHfCu alloys have also demonstrated TWSME [131]. It has recently reported that $Ni_{45.3}Ti_{29.7}Hf_{20}Cu_5$ alloys have the capability to recover compressive strains of 2 % above 100 °C and two-way shape memory strain of 0.8 % above 80 °C [132].

As part of the maturation process for Ni-rich NiTiHf alloys a more comprehensive and systematic study is needed to better understand the effects of chemical composition, aging time and temperatures, applied stress states and crystallographic orientation on shape memory properties. Amongst the common strengthening mechanisms precipitate strengthening through a simple aging treatment is the most practical and cost effective method to increase the strength of the material and as an added benefit can be used to tailor the TTs. Thus, in the present study, the effects of Ni content, aging time and temperatures on the microstructure and shape memory behavior of single crystal and polycrystalline Ni-rich NiTi-20Hf were investigated.

2 Experimental Procedure

The aim of this chapter is to describe details on the fabrication and processing of the materials as well as the experimental methods used in characterization of NiTiHf polycrystalline and single crystal alloys. The details of material preparation, calorimetric measurements, mechanical testing and microstructural analysis will be presented throughout the chapter. Most of the experiments of this research were performed at the Smart Material's Laboratory (RGAN 019) at the Mechanical Engineering Department of University of Kentucky.

2.1 Materials Fabrication

All of the polycrystalline alloys were produce by induction melting or arc melting of high purity elemental constituents (99.98 wt. % Ni, 99.95 Ti, 99.5 Hf). The NiTiHf alloys were arc melted as 100g buttons using high purity elemental constituents. The nominal compositions of the alloys were (in at. %) $Ni_{50.3}Ti_{29.7}Hf_{20}$ (50.3Ni), $Ni_{50.7}Ti_{29.3}Hf_{20}$ (50.7Ni), $Ni_{51.2}Ti_{28.8}Hf_{20}$ (51.2Ni), $Ni_{52}Ti_{28}Hf_{20}$ (52.0Ni). The buttons were homogenized at 1000 °C for 48h in a vacuum furnace followed by furnace cooling. The average cooling rate between 950 °C and 800 °C was 10 °C /s falling to half that rate by 600 °C. This condition is referred to as "furnace cooled" throughout the text. The nominal composition of the alloys and ingot weight after melting are listed in Table 2.1. It is clear that very little loss in material was observed. In addition, a $Ni_{50.3}Ti_{29.7}Hf_{20}$ (at. %) alloy was induction melted using a graphite crucible and cast into a 1″ diameter copper chill mold. The ingot was homogenized at 1050 °C for 72 hours and then extruded at 900 °C with a 7:1 reduction in area. This condition is referred to as "as-extruded" throughout the text.

The single crystal samples were grown by the Bridgman technique in He atmosphere by using a prealloyed starting material with nominal composition of $Ni_{50.3}Ti_{29.7}Hf_{20}$ (at. %), which was fabricated by vacuum induction melting. The composition of the as-grown single crystals were determined by inductively coupled plasma atomic emission spectroscopy to be $Ni_{50.4}Ti_{29.9}Hf_{19.3}$ with 0.4 at. % Zr. The single crystal ingots were oriented along [001], [011] and [111] to study the orientations dependence of NiTiHf alloys.

Table 2.1: The nominal composition of the NiTiHf alloys.

Alloy Designation	Alloy Composition (at. %)	Ingot weight (g)
50.3Ni	$Ni_{50.3}Ti_{29.7}Hf_{20}$	100
50.7Ni	$Ni_{50.7}Ti_{29.3}Hf_{20}$	99.99
51.2Ni	$Ni_{51.2}Ti_{28.8}Hf_{20}$	100
52.0Ni	$Ni_{52}Ti_{28}Hf_{20}$	99.98

2.2 Materials Preparation

The extruded rods and ingots for each alloy were cut by electrical discharge machining (EDM) in various shape for different purpose. EDM is a manufacturing process whereby a desired shape is obtained using electrical sparks and is shown in Figure 2.1a. Compression samples (4 mm× 4mm× 8 mm) and dog bone shaped tensile samples were cut for mechanical testing which the geometries are illustrated in Figure 2.1b. The thickness of dog bone shape tensile sample was 1.5 mm. Also small pieces were cut to determine the TTs of the material, microstructure analysis, and hardness test by using EDM.

Lindberg/Blue M BF514541 Box furnace used to carry out all heat treatments on the alloys. The size of chamber is 38.1×38.1×38.1 Cm with the maximum temperature reaches to 1200 °C. The furnace came with factory installed air/atmosphere port with a capability of running most gases such as nitrogen, argon, and helium however the furnace was not designed to be gas-tight atmosphere. The furnace was also equipped with a vent at the top to help remove contaminants from the furnace chamber. The furnace was set to the desired temperature and allowed to reach the set temperature before the sample was put in the furnace. After putting the sample in the furnace, the time was noted once the temperature reached the set temperature again. The heat treatments were followed by quenching the sample into water at room temperature. It is important to mention that for heat treatments above 500 °C, the samples were encapsulated under vacuum in a quartz tube for each aging cycle to avoid the oxidation process and then quartz tube was broken and quenched in water bath.

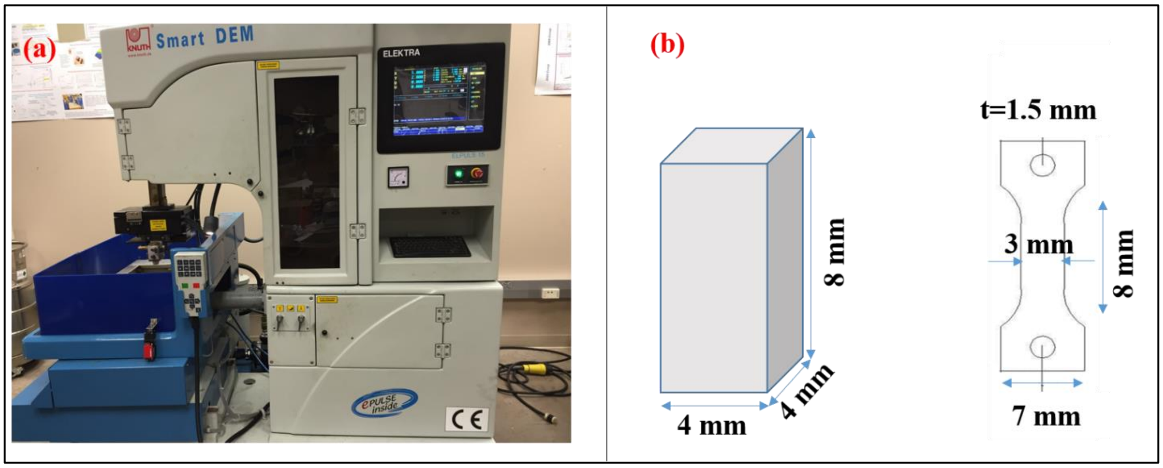

Figure 2.1: (a) Electrical discharge machining and (b) geometries of compression and tensile samples.

2.3 Calorimetry Measurements

Stress-free phase transformation temperatures (martensite finish, M_f; martensite start, M_s; austenite start, A_s; and austenite finish, A_f) were measured using a Perkin-Elmer Pyris 1 differential scanning calorimeter (DSC) as shown in Figure 2.2. Typical temperature range is from -150 to 600 °C and the heating/cooling rate was kept at 10 °C/min in nitrogen atmosphere. The temperature scale is calibrated by using two-point (or more) calibration method where the onset temperatures for the melting points of high purity Indium and Zinc standard provided by Perkin Elmer were measured. In addition, the furnace was calibrated by using the furnace calibration feature in Pyris software.

Sample preparation greatly affects the measured TTs due to residual stresses that can develop in sample during preparation process. Sample must be polished to establish good thermal contact with the bottom of the pan and its weight should be in the range of 20-40 milligrams. Both the sample weight and heating rate affect the DSC response since increasing the sample weight and/or heating rate increase the temperature gradients in the sample, resulting in decreased signal quality and resolution.

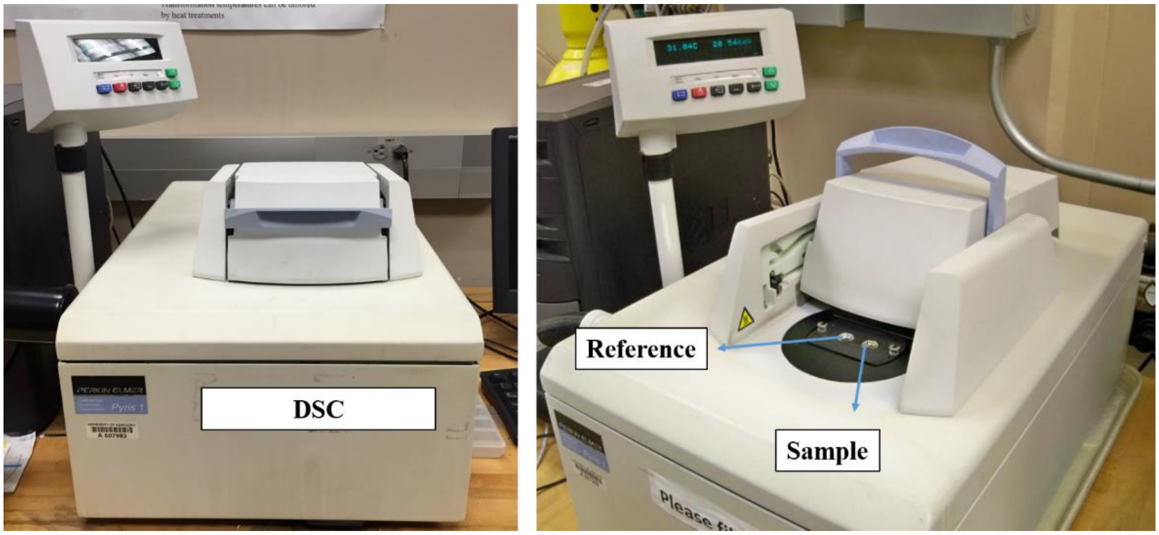

Figure 2.2: Pyris I DSC to measure the stress free phase transformation temperatures.

The basic principle of the operation of the DSC is the measurement of the rate at which heat energy is supplied to the specimen in comparison to a reference material to maintain a constant temperature rate [133]. Sample is thermally cycled and the difference of the supplied heat power is recorded as showed in Figure 1.3a. The net amount of heat released (ΔH) during phase transformation was calculated form the area under the transformation peaks. The TTs measured as the intersection of the base line and the maximum gradient line of a transformation peak. The martensite peak (M_p) and austenite peak (A_p) were measured as the points in the transformation for which the slope of the curve is equal to zero. In addition, thermal hysteresis was determined as the difference between the A_p and M_p ($\Delta H = A_p - M_p$).

2.4 Hardness Test

Hardness is the property of a material that measures its resistance to plastic deformation by penetration. Figure 2.3 shows that an indenter is pressed into the surface of the metal to be tested under a specific load for a definite time interval, and a measurement is made of the size or depth of the indentation. There are three principal standard test methods for expressing the relationship between hardness and the size of the impression; Brinell, Rockwell and Vickers. In the Vickers hardness test, accurate readings can be taken, and just one type of indenter is used for all types of metals and surface treatments.

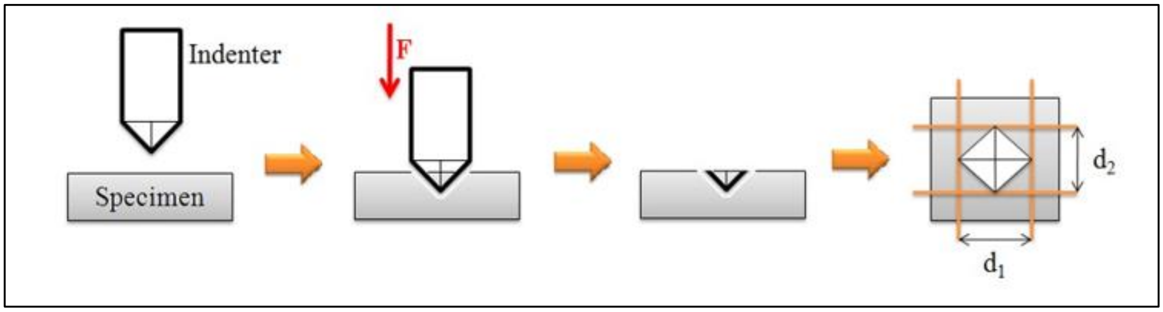

Figure 2.3: Schematic of Vickers hardness measurement.

In this project, hardness measurements were obtained using Sun-tec model FM-7 Vickers microhardness testing setup. Samples mounted in epoxy were polished to mirror finish prior to measurements. Pyramidal indenter of 136º tip was used with a 100 gram force and 15 seconds dwell time. Ten reading were taken for each sample, the highest and the lowest reading were omitted and the average of the remaining 8 readings were reported. The Vickers hardness (HV) was calculated by the ratio of applied force over the area of indentation by using following equations:

$$Area\ of\ Indentation\ (A) = \frac{d^2}{2\sin\frac{136}{2}} \approx \frac{d^2}{1.854} \quad (2.1)$$

$$HV = \frac{F}{A} = 1.854\frac{F}{d^2} \quad (2.2)$$

where d is the mean of d_1 and d_2 (Figure 2.3) and F is load in kgf. In shape memory alloys, hardness depends on the testing temperature and could be different for martensite and austenite phases.

2.5 Mechanical Testing

The thermo-mechanical experiments were conducted using an MTS Landmark servohydraulic test frame with custom compression/tension grips which is shown in Figure 2.4. The applied force was measured by a 100 kN capable load cell and the axial strain was measured by an MTS high temperature extensometer with a gauge length of 12 mm. Heating of the sample was achieved by conduction through the compression/tension plates at a rate of 10 °C/min and liquid nitrogen fellow through copper coils wrapped around the grips to cool the system at a rate of 5 °C/min. A PID driven Omega CN8200 series temperature controller ensured stable heating/cooling rates with K-type thermocouples attached to both the specimen and grips. A cryogenic grade, on/off solenoid valve commanded by the temperature controller was used to control the flow of liquid nitrogen. The experimental setup allowed testing of sample in compression or tension at temperature range between -100 to 600 °C. This enabled mechanical characterization of the sample in austenite and martensite phases (stress-strain test) as well as testing over a range of temperatures during thermal cycling under applied stress.

The compression/tension sample was polished mechanical with a 600 grit paper to remove the surface residue left after being cut by EDM. A K-type thermocouple was attached to the sample and the specimen was placed between the test setup in proper position. Unless indicated, otherwise the rate of $8x10^{-4}$ mm/sec for loading and 100 N/sec for unloading was used in mechanical tests.

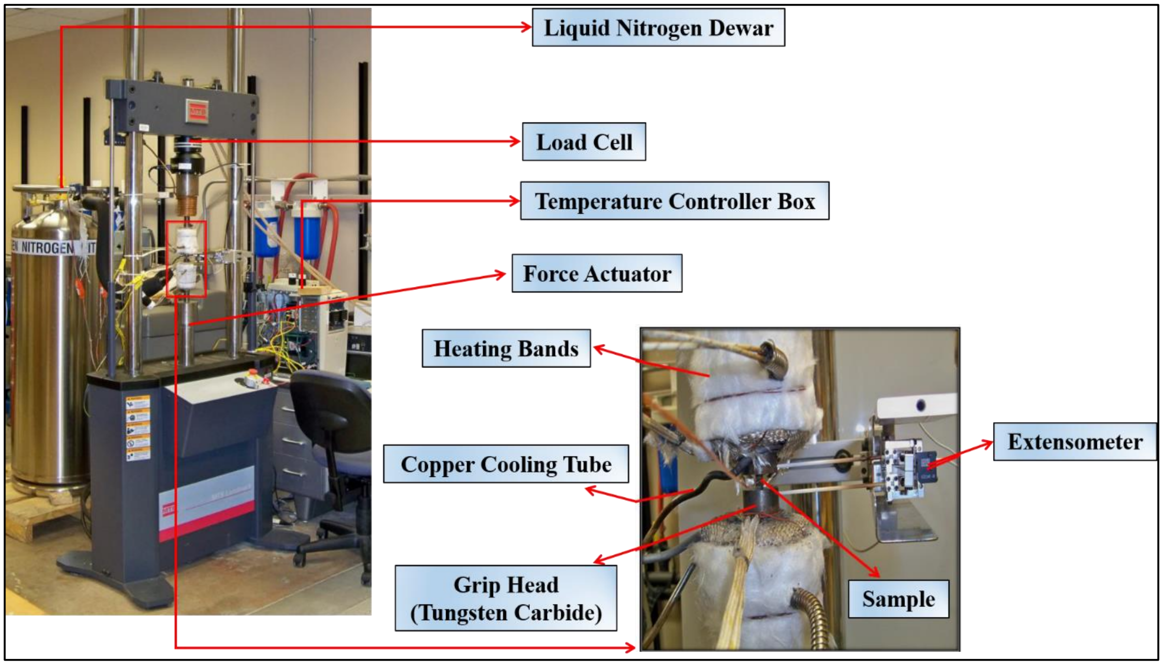

Figure 2.4: MTS Landmark system.

2.6 Microstructural Analysis

Microstructural analysis of the sample was conducted by transmission electron microscope (TEM) using a JEOL 2010F instrument operated at 200 kV. Samples for TEM investigation consisted of 3mm discs were cut by EDM from selected samples and subsequently ground to ~ 0.1 mm thickness and electro-polished in a solution of 30 % nitric acid in methanol at -30 ºC and 13 V. In collaboration with Universitat De les Illes Balears, Conventional and high resolution TEM observations were performed in a Hitachi H600 100 kV and a Jeol 2010 200 kV (0.19 nm point to point resolution) microscopes, respectively.

3 Effects of Chemical Composition

3.1 Introduction

One of the major areas of the thrust of this project was in the field of design of new SMAs based on the atomic bonding when new element are added to the alloys system. It is known that in metallic materials the delocalized valence electrons hold the non-valence electrons which nuclei of atoms together and form metallic bonds. This concept has been utilized to find possible combination of metal which can be added to get the desire properties from the SMAs. Two methods have been employed to design the alloys. First method is the number of valance electron per atom of the alloy (e_v/a) and the second one is valance electron concentration (C_v).

Zarinejad et al. revealed a practical relationship between the chemical composition and TTs by considering the number and concentration of valence electrons in NiTi-based alloys [134]. The number of d and s electrons is accepted as the number of valence electrons for an atom in transition metals while the number of valence electrons is considered to be p and s electrons for an atom in non-transition metals [135]. The number and average concentration of valence electrons of alloys can be calculated with the following equation [135];

$$\frac{e_v}{a} = f_A e_v^A + f_B e_v^B + f_C e_v^C + \cdots \tag{3.1}$$

$$C_v = \frac{e_v}{e_t} = \frac{f_A e_v^A + f_B e_v^B + f_C e_v^C + \cdots}{f_A Z_A + f_B Z_B + f_C Z_C + \cdots} \tag{3.2}$$

where f_A, f_B and f_C and are atomic fractions of A, B and C elements, Z_A, Z_B and Z_C are the atomic numbers of elements A, B and C, respectively and e_v^A, e_v^B, e_v^C are the related valence electrons for the elements in an alloy system. It has been shown that the TTs do not have a clear trend with e_v/a while they generally decrease with increasing c_v [94, 135]. Based on the study conducted from the literature available, following compositions listed in Table 3.1 were found to be promising in the direction of this research.

Table 3.1: Composition of Ni-rich NiTiHf alloys.

Ni-rich NiTiHf (at. %)					
Alloy Designation	**Ni**	**Ti**	**Hf**	**e_v/a**	**C_v**
50.3Ni	**50.3**	**29.7**	**20**	**7.018**	**0.200**
50.7Ni	**50.7**	**29.3**	**20**	**7.042**	**0.201**
51.2Ni	**51.2**	**28.8**	**20**	**7.072**	**0.202**
52.0Ni	**52.0**	**28.0**	**20**	**7.120**	**0.203**

In addition, changing in composition of an alloy could be resulted in solid solution strengthening which is a technique to increase overall mechanical strength of the material. The reason behind this phenomenon is that when an impurity is added to metal, the impurity imposes a lattice strain on the surrounding atoms. These lattice strain interact with the dislocations and as a result the dislocation movement is inhibited.

In this chapter, a systematic investigation is conducted to reveal the changes in microstructure (martensite morphology and precipitation characteristics) and shape memory properties (transformation strain and temperature, hysteresis, superelastic behavior) of four selected Ni-rich NiTiHf alloys in the furnace cooled condition. In this series of alloys, Hf content was fixed at 20 at. % and Ni was increased form 50.3 at% to 52 at%. Hereafter, the four alloys studied in this investigation will be generally referred to as NiTi-20Hf, but specific alloys will be designated by their Ni content (i.e., 50.3Ni, etc.).

3.2 Experimental Results

3.2.1 Stress-free Phase Transformation Temperatures

The DSC responses of the Ni-rich NiTiHf alloys in the furnace cooled condition are shown in Figure 3.1a and the TTs, which were extracted from DSC responses, are summarized in Table 3.2. It is clear that TTs are composition dependent and the transformation peaks became broader as the Ni content increased. The sample with lowest Ni content (50.3Ni) had an M_p of 142 °C and A_p of 174 °C. As the Nickel content was increased to 50.7 at. %, M_p decreased to 105 °C. Thermal hysteresis in both the 50.3Ni and 50.7Ni samples, which was defined as the difference between A_P and M_p ($\Delta T = A_p – M_p$), was as low as ~30 °C. When the Nickel content was increased to 51.2 at. %, the M_p and A_p were determined to be 122 °C and 182 °C, respectively. But the reverse transformation (martensite to austenite) in the 51.2Ni alloy was not very well defined and occurred over a broad temperature range. In 52.0Ni, both transformation peaks were very broad and difficult to detect, but careful examination of the curves revealed that M_p and A_p were about 93 °C and 106 °C, respectively. It is interesting to note that as the Nickel content increased, the difference between A_f and A_s was became much larger than the difference between M_s and M_f, which means that the reverse transformation was much more difficult to complete than the forward transformation as the Ni content increased.

Figure 3.1b demonstrates the hardness of the NiTiHf alloys and transformation peak temperatures as a function of the Ni content. The hardness values were determined at room temperature, with all alloys consisting of a martensitic matrix phase. As summarized in Figure 3.1b, hardness increased from 420 HV to the maximum value of 650 HV with increasing Nickel content. On the other hand, the transformation peak temperatures were not a consistent function of Ni content, although it is clear that 50.3Ni had the highest and 52.0Ni had the lowest M_p, while 51.2 Ni had the highest value for A_p and an intermediate value for M_p.

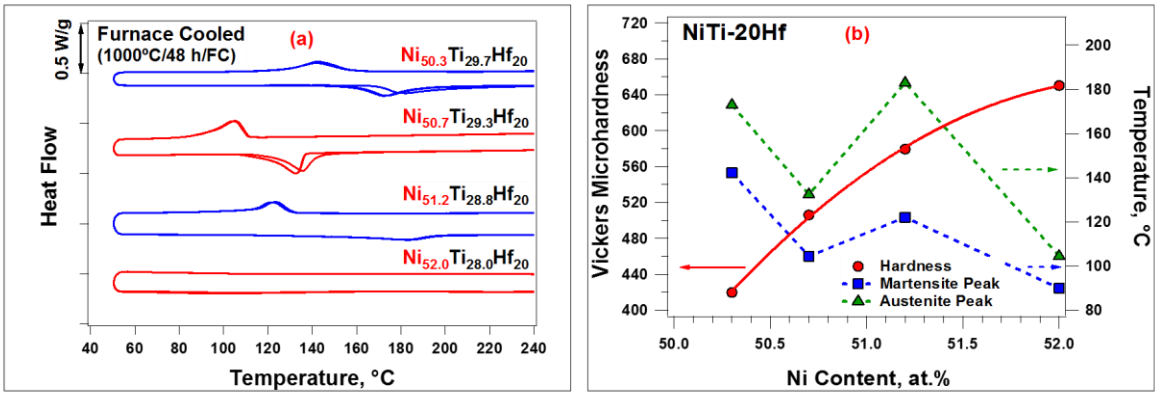

Figure 3.1: (a) DSC responses of the furnace cooled NiTi-20Hf alloys and (b) Vickers microhardness and transformation peak temperatures of the Ni-rich NiTi-20Hf alloys as a function of Ni content.

Table 3.2: Transformation temperatures for the Ni-rich NiTi-20Hf alloys in the furnace cooled condition.

Alloy designation	Alloy composition	M_s(°C)	M_f(°C)	M_p(°C)	A_s(°C)	A_f(°C)	A_p(°C)
50.3Ni	$Ni_{50.3}Ti_{29.7}Hf_{20}$	156	128	142	160	189	174
50.7Ni	$Ni_{50.7}Ti_{29.3}Hf_{20}$	111	91	105	113	137	133
51.2Ni	$Ni_{51.2}Ti_{29.8}Hf_{20}$	131	115	122	157	197	182
52.0Ni	$Ni_{52.0}Ti_{28.0}Hf_{20}$	107	79	93	84	160	106

3.2.2 Microstructure

Figure 3.2 illustrates the representative microstructures of the furnace cooled Ni-rich NiTiHf alloys at room temperature. Conventional TEM images of 50.3Ni revealed the formation of relatively large martensite plates (~0.5 µm in width), with arrays of dislocations localized in several areas, as shown in Figure 3.2a. The selected area diffraction patterns (SADP) confirmed that 50.3Ni has B19' martensitic structure (Figure 3.2b), as well as the rest of the alloys in this work. No precipitates were observed in this alloy in spite of the furnace cooled condition, which was confirmed by the SADP.

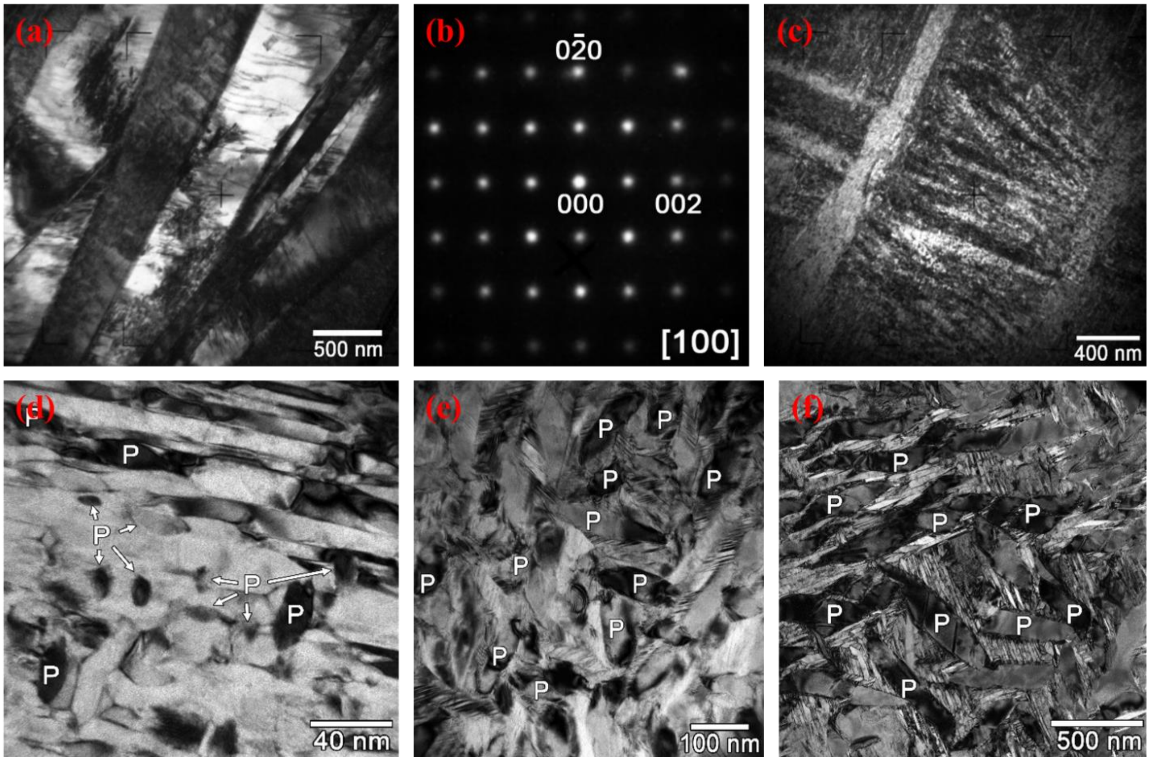

Figure 3.2: TEM images of (a) furnace cooled $Ni_{50.3}Ti_{29.7}Hf_{20}$, (b) SADP of $Ni_{50.3}Ti_{29.7}Hf_{20}$, (c,d) TEM images of furnace cooled $Ni_{50.7}Ti_{29.3}Hf_{20}$, (e) $Ni_{51.2}Ti_{28.8}Hf_{20}$, and (f) $Ni_{52}Ti_{28}Hf_{20}$.Some of the precipitates present in the micrographs are labelled with a "P".

The 50.7Ni alloy exhibits notably thinner martensite plates (Figure 3.2c) than 50.3Ni and a blurred contrast in the two-beam condition images recorded at low magnification. Figure 3.2d shows a TEM micrograph of 50.7Ni at higher magnification, where nanometric precipitates with lenticular shape of 5–15 nm in width and 15–35 nm in length can be observed. These nanometric particles were responsible for the blurred contrast at low magnifications (Figure 3.2c). The same precipitates were present in 51.2Ni and 52.0Ni, except that they were notably larger in size (~75–250 nm in width and ~200–750 nm in length), as shown in Figures 3.2e and 2f, respectively. The martensitic morphology is also notably different in the 51.2Ni and 52.0Ni samples as compared to 50.3Ni and 50.7Ni alloys. In the former samples, the size of the precipitates hinders the growth of large martensite plates, like those observed in 50.3Ni and 50.7Ni alloys. Instead, the formation of the martensite is constrained to those areas between the H-Phase particles promoting smaller martensite plates.

The SADPs and high resolution TEM (HRTEM) images obtained from the precipitated phase show the characteristic features of the H-phase [110, 111]. For instance, Figure 3.3a shows a SADP obtained from an individual precipitate of 52.0Ni (together with a small portion of surrounding matrix) containing the characteristic n/3<110> satellite spots of H-phase, located at 1/3 and 2/3 of the distance of the fundamental spots along a crystallographic direction corresponding to the $<110>_{B2}$ direction of cubic austenite (the satellites are marked by triangles in Figure 3.3a). In addition, other zone axes show the $n/4<210>_{B2}$ superlattice spots, which are also typical of the H-phase [110]. Concomitantly, the HRTEM images of individual precipitates exhibited an enhanced contrast every three $\{110\}_{B2}$ planes when observed along zone axes perpendicular to these plane, as revealed in Figure 3.3b, which was obtained along the $[111]_{B2}$ zone axis. Table 3.3 presents the results of energy dispersive spectroscopy (EDS) microanalysis performed on 51.2Ni and 52.0Ni alloys from the large particles and matrix. The precipitates are found to have compositions richer in Ni and Hf and poorer in Ti compared to the surrounding matrix, in agreement with the compositions previously reported for the H-phase [110, 111].

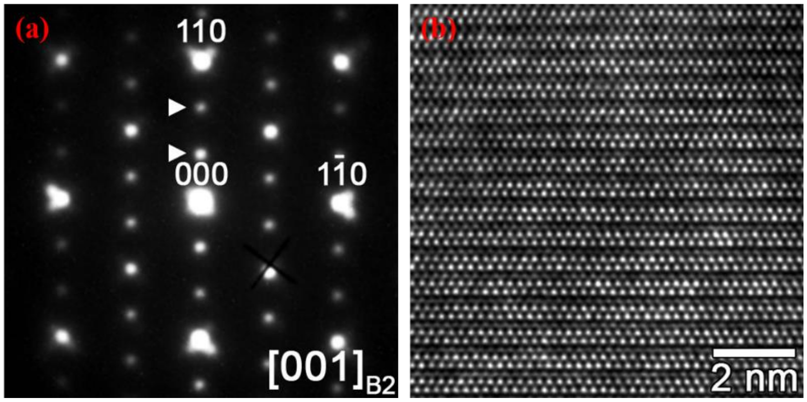

Figure 3.3: (a) Selected area diffraction pattern and (b) high resolution TEM image of an individual H-Phase precipitate in $Ni_{52}Ti_{28}Hf_{20}$.

Table 3.3: Composition of matrix and H-Phase as determined by EDS microanalysis (average of 5 different measurements in each phase).

Sample – phase	**Ni (at. %)**	**Ti (at. %)**	**Hf (at. %)**
51.2Ni – matrix	49.5	27.9	22.6
51.2Ni – precipitates	52.1	20.0	27.9
52.0Ni – matrix	50.5	29.1	20.3
52.0Ni – precipitates	52.9	18.6	28.5

3.2.3 Shape Memory Behavior

Figure 3.4 represents the shape memory responses of the Ni-rich NiTi-20Hf alloys determined by thermal cycling under constant compressive stress. Specimens were loaded to selected stress levels at a temperature above A_f, the stress was then held constant and the sample was thermally cycled through the transformation regime. Once the upper cycle temperature was reached, the stress level was increased and the process was repeated. For 50.3Ni, M_s was raised from 160 to 180 °C and the thermal hysteresis widened from 19 to

50 °C when the stress was increased from 100 to 1000 MPa. Recoverable strain of 1% with no irrecoverable strain was observed under 500 MPa, while irrecoverable strain reached the maximum value of 0.6% at 1000 MPa. As Ni content increased to 50.7 at. %, M_s decreased to 120 °C under 100 MPa and perfect dimensional stability with recoverable strain of 2.1% was obtained at 700 MPa. Irrecoverable strain was 0.3% at 1000 MPa, whereas further loading to 1500 MPa produced a large irrecoverable strain of 2.4%. In addition, the thermal hysteresis of 50.7Ni was increased from 21 to 40 °C as stress increased from 100 to 1000 MPa. Thus in the furnace cooled condition, thermal hysteresis and dimensional stability improved while the TTs decreased as Ni content increased from 50.3 to 50.7 at. %.

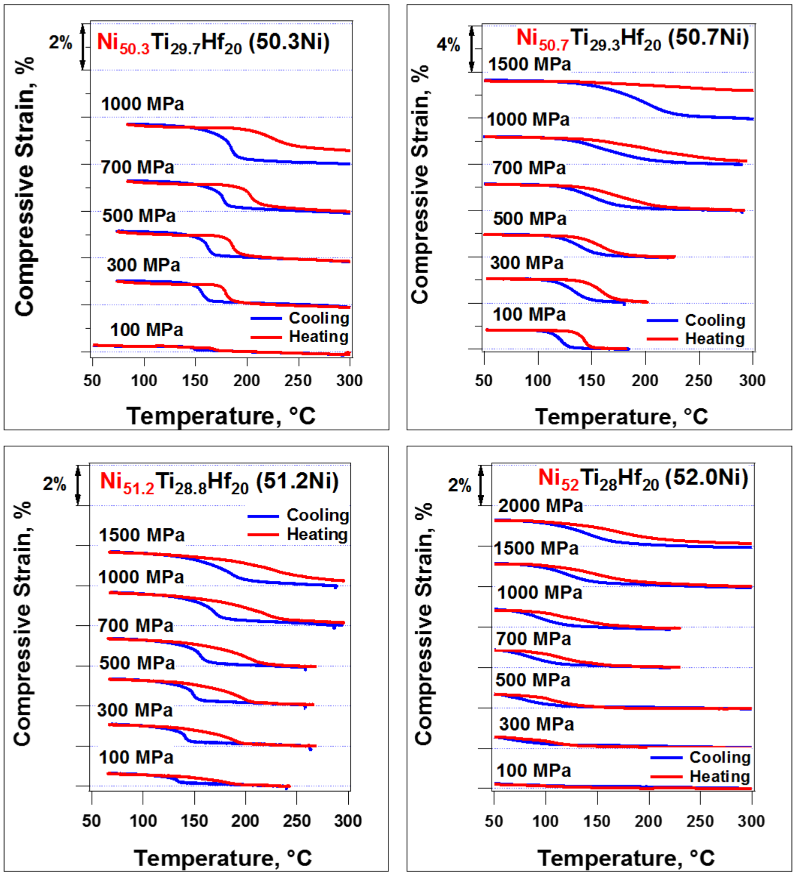

Figure 3.4: Shape memory response of the furnace cooled NiTi-20Hf alloys determined by thermal cycling under constant stress.

The strength of the material was further improved and almost fully recoverable shape memory effect with recoverable strain of 1% at 1500 MPa was achieved as Ni content increased to 51.2 at. %. In this alloy, thermal hysteresis only increased from 33 to 45 °C as the applied stress increased from 100 to 1500 MPa. It should be also noted that the reverse transformation for 51.2Ni occurred over a wide temperature range, which is in a good agreement with the DSC results shown in Figure 3.1a. In the 52.0Ni alloy, a low recoverable strain of 0.8% was observed as the sample was thermally cycled at 1500 MPa. This behavior can be attributed to the fact that it was difficult to select and/or grow martensite variants when the precipitates were present in such a high volume fraction. However, the 52.0Ni alloy did exhibit near perfect dimensional stability with a total strain of 1.1% and small irrecoverable strain of 0.2% under a very high stress level of 2000 MPa. Also, temperature hysteresis only increased from 20 to 36 °C with stress increasing from 300 to 2000 MPa.

In summary, as Nickel content of the NiTi-20Hf alloys increased, the volume fraction of precipitate phase and strength increased, resulting in a decrease in recoverable strain, but an increase in the stress carrying capability of the alloy. The high-stress properties of these alloys make them promising candidates for high strength thermal actuator applications where stress capability may be more critical than strain.

The stress cycling responses of the Ni-rich NiTiHf alloys at selected temperatures are shown in Figure 3.5. It should be noted that before running each test, the samples were heated above A_f+50 °C and then cooled to the testing temperature. Before loading, 50.3Ni is partially martensite at 140 °C while it is fully austenite at 160 °C and 180 °C. However, it is important to note that for the 50.3Ni alloy, all three testing temperatures are below A_f

due to the hysteresis. Therefore, the residual strains observed at the end of each mechanical cycle at each of the selected temperatures can be attributed to residual martensite. This was confirmed by thermally recovering all the residual strain in each case.

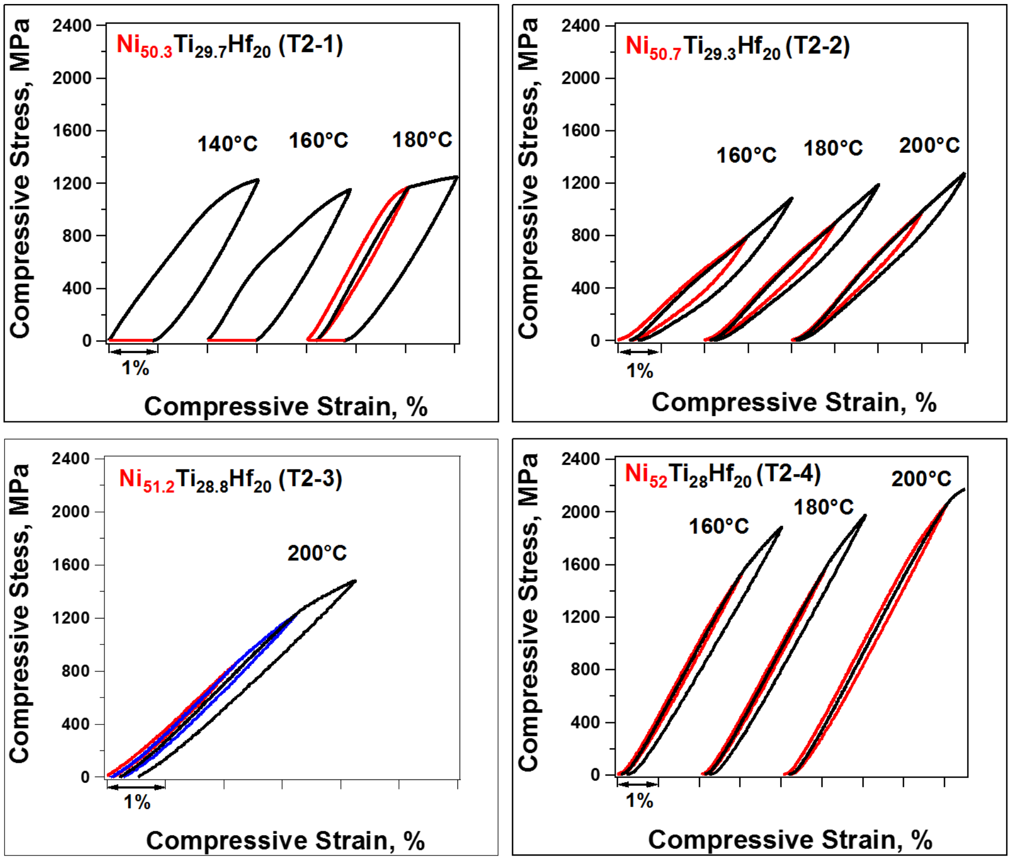

Figure 3.5: Stress-strain responses of the furnace cooled Ni-rich NiTi-20Hf alloys.

In 50.7Ni, all the tests were performed above A_f, where full recovery of 4% strain was accomplished between 180–200 °C. However, the stress-strain curves exhibited very high slopes in the superelastic regime during the phase transformation. As Ni content increased above 51 at. %, no superelasticity was observed due to fact that the critical stress for the phase transformation was higher than the stress for plastic deformation. The 52.0Ni sample failed in compression at 200 °C at a strain of 4% as the stress level exceeded 2000 MPa. It is clear from Figure 3.5 that the high stresses required to induce the martensitic transformation in the 51.2Ni and 52.0Ni alloys result in plastic deformation before superelastic behavior can occur.

3.3 Discussion

The formation of H-phase precipitates, which was observed in the furnace cooled 50.7Ni, 51.2NIi and 52.0Ni alloys, can be attributed to the moderate cooling rate from 1000 °C and the high driving force for precipitation in these more Ni-rich alloys. Since the H-phase is richer in Ni [110], the precipitation process was enhanced by an increased Ni content, resulting in larger precipitate size and volume fraction.

The H-phase precipitates are fully coherent with the austenitic matrix. However, when the matrix transforms to martensite, this perfect coherency is lost due to the transformation strain associated to the martensitic transformation [110]. Therefore, in presence of H-phase precipitates, the martensitic matrix has to accommodate the non-transforming particles. When precipitates are small, the strain due to the mismatch between martensite and a full precipitate can still be accommodated, and relatively large martensite plates can form and absorb the precipitates during its growth. However, stress and strain fields are developed at the precipitate/matrix interface as the transformation proceeds, which restricts the plate growth in relation to the precipitate-free material (compare Figures 3.2a and 3.2c). When precipitates are large, as in the 51.2Ni and 52.0Ni alloys, the transformation strain around a large particle can no longer be accommodated and the martensite plates form between the particles, which become impenetrable obstacles to further martensite plate growth. The furnace cooled 50.7Ni sample seemed to result in a precipitate size between these two limiting cases. Note that in Figure 3.2e, the martensite plates are stopped by the largest particles, but for slightly smaller precipitates, an individual martensite plate can absorb many particles.

The compositional change due to precipitation results in depletion of Ni and Hf, and enrichment of Ti in the matrix. If only the nominal alloy composition is considered, it is well known that increasing the Ni content decreases the TTs. However, as Ni-rich precipitates form, they tend to increase the TTs by depleting the matrix of Ni. Comparing the TTs of all the furnace cooled alloys as a function of Ni content (Figure 3.1b), there is no clear trend due to the fact that the furnace cooled alloys already contain varying levels and sizes of precipitates making any direct comparison meaningless. The broad transformation peaks observed in the DSC response of 52.0Ni can be attributed to compositional inhomogeneity of the matrix due to large H-phase precipitates.

Figure 3.6a illustrates the recoverable and irrecoverable strains as a function of applied compressive stress obtained from the thermal cycling results shown in Figure 3.4. The presence of H-phase precipitates strongly modifies the shape memory response of the Ni-rich NiTiHf alloys as demonstrated in Figure 3.4. Formation of small precipitates (tens of nm in length) in 50.7Ni results in the largest recoverable strain of 2.1% since the martensite plates readily absorb the precipitates during the martensitic transformation. However, the recoverable strain decreases and irrecoverable strain increases at stresses above 800 MPa due to plastic deformation. The lower recoverable strain of 50.3Ni compared to 50.7Ni is attributed to the formation of relatively larger martensite plates with internal twins, together with higher plastic deformation in the 50.3Ni alloy.

As the non-transformable precipitates account for a larger volume fraction of the alloy, as in the 51.2Ni and 52.0Ni alloys, the recoverable strain is reduced to less than 1%

(Figure 3.6a), while strength of the material is improved (Figure 3.1b) resulting in smaller irrecoverable strains (less than 0.3%) under stress levels as high 1500-2000 MPa. It has been illustrated that the (001) compound twinning as lattice invariant shear and (011) type I twinning modes are the most frequently observed in NiTiHf alloys [110, 136]. In the samples where the martensite plates are constrained between large precipitates, i.e. 51.2Ni and 52.0Ni, both types of twinning are observed more or less equally and in some regions (001) compound twins are the predominant twinning mode in relation to (011) type I twins [110]. However, the most frequently observed twinning mode in the samples containing nano-size precipitates is (011) type I twins [110, 136]. In turn, the well-known precipitation hardening effect is typical for small and coherent precipitates but large particles are usually indicative of over-aging and a decrease in strengthening. Consequently, the improvement in strength observed in 51.2Ni and 52.0Ni alloys in presence of large particles could be related to the change in martensite plate size and twinning mode observed in these samples.

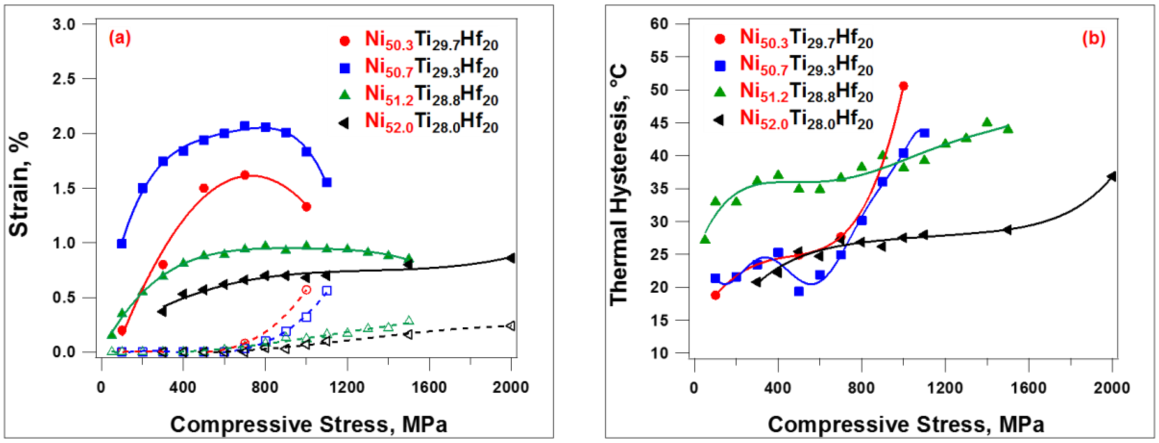

Figure 3.6: (a) Recoverable (solid line) and irrecoverable (dashed line) strains and (b) thermal hysteresis of Ni-rich NiTiHf alloys as a function of applied compressive stress.

Thermal hysteresis of Ni-rich NiTiHf alloys as a function of compressive stress is summarized in Figure 3.6b. It is clear that thermal hysteresis is highly composition and applied stress dependent. Thermal hysteresis is initially less than 25 °C in 50.3Ni and 50.7Ni alloys but it increases to more than 40 °C for applied stresses above 800 MPa, which correlates with the change in irrecoverable strain with stress as shown in Figure 3.6a. The generation of defects during phase transformation increased with stress, in turn leading to increased energy dissipation and wider hysteresis. As Ni content increased to 51.2 at. %, the morphology of the martensite changed, with growth of martensite plates limited to the space between large precipitates. Thus, additional energy would be dissipated due to the interaction between the interphases of martensite and H-phase precipitates, resulting in an increased thermal hysteresis (30–45 °C) in the 51.2Ni alloy. Similar effects of the microstructure on thermal hysteresis under stress have been observed in NiTiHf/Zr alloys [137, 138]. The decrease in thermal hysteresis as Ni content reached 52 at. % can be attributed to the high strength of the alloy where small irrecoverable strain (less than 0.2%) was obtained even at a stress level of 2 GPa. In this case, dissipation of energy due to defect generation during phase transformation can mostly be neglected.

The high strength of the alloys can be attributed to a combination of solid-solution and precipitation hardening. The 50.3Ni alloy has no precipitates and has lower strength compared with the other alloys, but is still considerably stronger than single phase Nitinol compositions. However, it has been previously reported that the strength of 50.3Ni can be increased substantially by nano precipitation after aging and perfect shape memory and superelastic behavior can be obtained [113, 114, 139, 140]. The furnace cooled 50.7Ni was already precipitation hardened and almost full shape recovery is observed under 1000 MPa. The 51.2Ni and 52.0Ni alloys had an even higher volume fraction of precipitate phase in the furnace cooled condition and they were capable of exhibiting shape memory effect under 1500 and 2000 MPa, respectively. Since the precipitates in these two alloys are very large, high strength can be attributed to a number factors including the contribution from solid solution hardening, constraints due to the large interfacial area and a change in martensite morphology and type of twinning.

Figure 3.7a illustrates the M_s temperature of the Ni-rich NiTiHf alloys as a function of applied stress, extracted from the results shown in Figure 3.4. The extrapolation of the data to zero stress provides the M_s in the stress-free conditions, which is in a good agreement with the M_s determined from the DSC results shown as hollow markers in Figure 3.7a. It is worth to mention that the M_s for 52.0Ni in stress free condition is between 80–100 °C. The linear behavior shown in Figure 3.7a is consistent with CC (Equation 1.3) Nevertheless, the experimental slopes of the curves in Figure 7a, vary significantly across the various samples, which is difficult to explain with the CC equation alone.

The CC relationship is obtained from Equilibrium Thermodynamics as applied to first order phase transformations. In the case of martensitic transformations, the strict applicability is restricted to “clean” experiments, *i.e.* single phase and single crystal microstructure and stress-induced transformation to obtain a single martensite variant [32]. For the present study, only the 50.3Ni alloy even approaches these requirements, as it represents a single phase microstructure. In the case of 50.7Ni, 51.2Ni and 52.0Ni, the internal stress fields created by the precipitates introduce local variables that are not accounted for by Equilibrium Thermodynamics, which restricts the quantitative accuracy of the CC equation. In ref. [141] a thermodynamical analysis including elastic and dissipative energy terms is presented, which can explain the lower CC slopes exhibited by samples containing precipitates in spite of their lower transformation strain. The very different slopes exhibited by the stress vs. M_s lines for the 50.3Ni and 50.7Ni alloys results in an intersection of the lines at about 170 °C (Figure 3.7a). Thus for higher temperatures, the stress needed to stay in martensitic phase is lower in the 50.7Ni alloy than in 50.3Ni, in spite of the fact that the M_s (at zero stress) for the 50.7Ni alloy is notably lower.

It is clear from Figure 3.7a that M_s does not change significantly with applied stress, resulting in a large CC slope of 42.5 MPa/ °C in the 50.3Ni alloy, while the CC slope is ~12 MPa/ °C in 50.7Ni. In fact, the 50.7Ni alloy has the lowest CC slope and the highest recoverable strain (Figure 3.6a) of the NiTi-20Hf alloys investigated. Also, the CC slope is in the range of 22–25 MPa/ °C for the 51.2Ni and 52.0Ni alloys.

The lack of superelasticity in the present Ni-rich NiTi-20Hf alloys is likely due to the high CC slopes and high stress-strain slope during transformation (transformation hardening), allowing plastic deformation to occur before significant transformation behavior can be induced. Since the CC slopes are relatively high, the required stress to induce martensitic transformation increases quickly with temperature and as a consequence shrinks the temperature window over which superelastic behavior can occur. In addition, the stress-strain slope in the transformation region increases with Ni concentration, requiring higher stress levels to complete the transformation, increasing the chance for plasticity to occur instead. Thus the likelihood of exhibiting superelasticity is extremely diminished, particularly in the more Ni-rich compositions. The difficulty for detwinning can stem from the strong internal stress fields developed around the big precipitates, and difficulty to move $(001)_{B19'}$ compound twins. When the stress fields around the precipitates are not along the direction of the external stress, the effective bias stress acting in the transformable regions (located in between the large precipitates) is diminished, and larger applied external stresses are needed to reorient martensite variants. This is evidenced in Figure 3.6a, which shows that the recoverable strain is saturated and starts to decrease at about 700-800 MPa in 50.3Ni and 50.7Ni, but for 51.2Ni and 52.0Ni the recoverable strain increases continuously with the external stress.

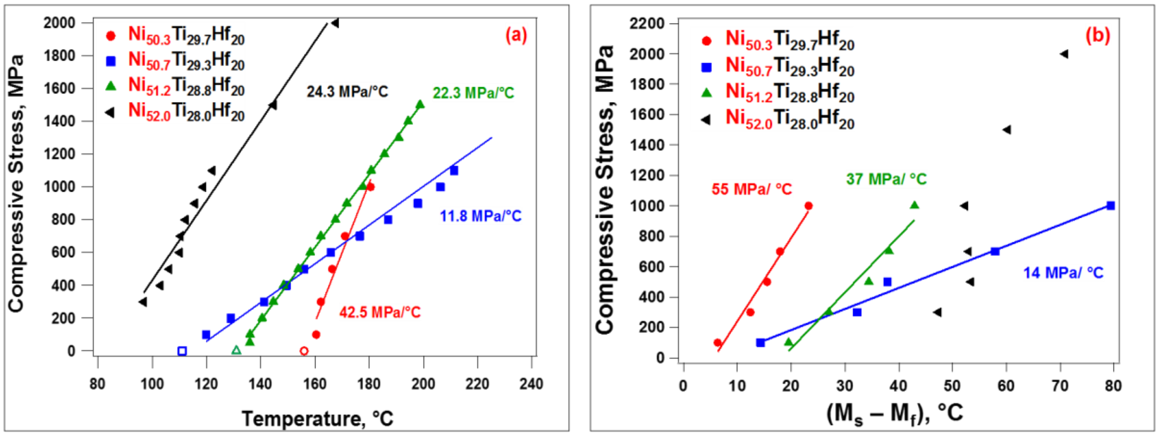

Figure 3.7: Stress vs. M_s temperature (a) and M_s–M_f (b) of Ni-rich NiTi-20Hf.

The difference between M_s and M_f at different stress levels for the furnace cooled Ni-rich NiTi-20Hf alloys are plotted in Figure 3.7b. It is clear from thermal cycling responses (Figure 3.4) that the martensitic transformation behavior is highly dependent on Ni content and the resulting characteristics of the microstructure. The M_s is lower than A_s for 50.3Ni while M_s becomes greater than A_s as Ni content was increased above 50.7 at. %. This change in transformation behavior can be attributed to the effects of precipitates to store elastic energy during the forward transformation. It is also evident from Figures 3.4 and 3.7b that the difference between M_s and M_f increases more rapidly with stress in 50.7Ni. This indicates a low strain-temperature slope during cooling in thermal cycling responses (Figure 3.4) that result in an increased elastic energy storage during forward transformation. Stored elastic energy helps the martensite to austenite transformation and less overheating is needed to initiate the reverse transformation, resulting in a shift of A_s

to lower temperatures. It is clear from Figure 3.7b that the difference between M_s and M_f is not linear in the 52.0Ni alloy and is instead related to the applied stress in a more complicated fashion, having little dependence on stress between 500 and 1000 MPa, but much more sensitive to stress at lower and higher levels. At low stress levels (<300 MPa), the martensitic transformation is not detected in the load-biased thermal cycling response, since the applied stress is not sufficient to reorient martensite variants as shown in Figure 3.4, leading to a self-accommodated structure. However, similar to 50.7Ni, the difference between M_s and M_f becomes greater at high stress levels resulting in more elastic energy stored in the matrix during the forward transformation, which then helps promotes the reverse transformation.

3.4 Conclusion

In this chapter the effects of stoichiometry (Ni content) on the shape memory properties and microstructure of furnace cooled Ni-rich NiTi-20Hf alloys were investigated. The findings can be summarized as follows:

1. H-phase precipitates were formed in the $Ni_{50.7}Ti_{29.3}Hf_{20}$, $Ni_{51.2}Ti_{28.8}Hf_{20}$ and $Ni_{52}Ti_{28}Hf_{20}$ alloys during furnace cooling after homogenization. The $Ni_{50.3}Ti_{29.7}Hf_{20}$ alloy was precipitate free under the same condition. The size and volume fraction of H-phase precipitates increased with Ni content. The composition of the H-phase was richer in Hf, poorer in Ti, and slightly richer in Ni as compared to the nominal composition of the matrix.
2. The Nickel content of the NiTi-20Hf alloys and the volume fraction of H-phase precipitates are the two main factors that affect transformation temperatures.

However, there is no clear trend for the TTs of the furnace cooled Ni-rich NiTi-20Hf with composition due to the fact that the furnace cooled alloys have different starting compositions and amounts of precipitate phase.

3. Martensite morphology varied with Ni content of the Ni-rich furnace cooled NiTi-20Hf alloys, as a consequence of the different microstructures. Nanometer size precipitates are readily absorbed by martensite plates in $Ni_{50.7}Ti_{29.3}Hf_{20}$. In contrast, the nucleation and propagation of martensite variants is limited in the space between larger H-phase precipitates for the 51.2Ni and 52.0Ni alloys. In addition, (011) type I twins was the dominant twinning mode in the alloys with nanosize precipitates while (001) compound and (011) type I twins were observed in the alloys where the martensite plates were constrained between precipitates.

4. The strength and shape memory properties of NiTi-20Hf alloys are highly composition dependent. As Ni content increased, the recoverable strain decreased while the strength of the material increased. Considerable plastic deformation took place at a stress level of 700 MPa in precipitation free $Ni_{50.3}Ti_{29.7}Hf_{20}$, while near perfect dimensional stability with less than 1% recoverable strain was observed at stress levels greater than 1500 MPa in the $Ni_{52}Ti_{28}Hf_{20}$ alloy. The decrease in recoverable strain with Nickel content in furnace cooled NiTi-20Hf alloys can be attributed to the increased volume fraction of non-transformable H-phase precipitates. The higher strength of NiTiHf compared to NiTi can be attributed to solid solution hardening, precipitation hardening, and changes in martensite twinning behavior.

5. Poor superelastic behavior of the furnace cooled Ni-rich NiTi-20Hf alloys is due to high CC slopes and a high stress-strain slope during transformation, which increases with Ni content. Both factors favor plastic deformation instead of transformation behavior.

4 Effects of Heat Treatments

4.1 Introduction

The most efficient method for increasing material strength and tailor the shape memory properties is precipitation hardening. Heat treatments could result in precipitation formation in SMAs that could be utilized to control TTs and increase material strength. The strengthening ability of the precipitates depends on the size, composition and interparticle distance. The precipitates act as an obstacle in the path of dislocation which dislocation must cut through the precipitate or must loop around it.

In the early stage of precipitation formation in the alloy, precipitates are small in size and are dispersed finely within the alloy which are expected to be coherent with matrix. In this stage, the dislocation has to shear across the precipitates (cut through them) to propagate that requires additional stresses, hence, inhibits the slip motion. In case of larger precipitates with larger interparticle distance, dislocation could bypass the precipitates by looping around them which is related to Orowan looping mechanism. As dislocation passes through, it leaves behind a dislocation ring around the particle while stress fields further inhibit the next passing dislocation motion. The change in mechanical strength as a function of volume fraction of precipitates is mathematically represented by the following equation;

$$\Delta\tau = \alpha_{\varepsilon} G \varepsilon^{3/2} \left(\frac{\rho}{b}\right)^{\frac{1}{2}} \tag{4.1}$$

where b is the magnitude of burger vectors, ρ is the volume fraction of precipitates, ε is the constrained lattice mismatch and α_{ε}. Also, the change in strength due to Orowan looping is represented by;

$$\Delta\tau = K\frac{1}{(L-2r)}\frac{Gb}{2\pi\sqrt{1-v}}\ln\left(\frac{2r}{r_0}\right) \quad (4.2)$$

where v is the matrix Poisson's ration, L is the interparticle distance, r is the mean particle radius, G is the matrix shear modulus, r_0 is the dislocation core radius and b is the burgers vector.

As part of the maturation process for Ni-rich NiTiHf alloys a more comprehensive and systematic study is needed to better understand the effects of aging temperature and time on precipitate growth and the subsequent impact on shape memory properties. Amongst the common strengthening mechanisms, precipitate strengthening through a simple aging treatment is the most practical and cost effective method to increase the strength of the material and as an added benefit can be used to tailor the TTs. The effect of aging on the microstructure and properties of the $Ni_{50.3}Ti_{29.7}Hf_{20}$ alloy have been previously investigated in some detail [109, 113, 114]. In this chapter, the effects of heat treatments on the precipitation characteristics and the corresponding shape memory behavior of a Ni-rich $Ni_{50.7}Ti_{29.3}Hf_{20}$, $Ni_{51.2}Ti_{28.8}Hf_{20}$ and $Ni_{52}Ti_{28}Hf_{20}$ alloys are investigated. In the previous chapter, it was shown that the furnace cooled Ni-rich NiTiHf alloys contain H-phase precipitates. In order to investigate the effects of thermal treatments on these alloys, they were solution treated at 900 °C for three hours followed by water quenching to avoid formation of precipitates in the solutionized condition.

4.2 Result and Discussion: $Ni_{50.7}Ti_{29.3}Hf_{20}$

4.2.1 Transformation Temperatures and Hardness

The TTs for $Ni_{50.7}Ti_{29.3}Hf_{20}$ alloy after various thermal treatments were determined via DSC using the tangent line method. All samples were thermally cycled three times in the DSC to determine the stability of the peaks. The DSC responses of the $Ni_{50.7}Ti_{29.3}Hf_{20}$ alloy as functions of aging temperatures and times are shown in Figure 4.1. The furnace cooled samples were aged at temperatures ranging from 300 to 700 °C for a fixed time of three hours (Figure 4.1a) and at 500 °C for times between 3 to 24 hours (Figures 4.1b). It is immediately obvious that for furnace cooled conditions, martensite transforms to austenite above 100 °C but the stability of the transformation peaks was highly heat treatment dependent.

Figure 4.1a shows an initial decrease in the TTs when the alloys were aged for three hours at 300 °C. After the initial drop, TTs increased with aging temperature up to 600 °C and then decreased with further increase in aging temperature. After aging at 500 °C, the alloy had M_f of 130 °C, which qualifies it as a HTSMA. The peaks were very distinct and stable, which can be attributed to the increased strength of the matrix due to the precipitation hardening. Transformation peak temperatures were reached to their maximum values of 155 ºC and 190 ºC for M_p and A_p, respectively, after 600 °C-3h aging. Thermal hysteresis increased from 23 to 48 °C as aging temperature raised from 300 to 700 °C. Figure 4.1b illustrates the effects of aging time (from 3 to 24 hours) at 500 °C. When the samples were aged at 500 ºC, TTs slightly increased with aging time up to 1 hour while they increased for longer durations.

In order to broaden our knowledge of the effects of aging on shape memory properties of $Ni_{50.7}Ti_{29.3}Hf_{20}$ alloy, the alloy was solution treated at 900 °C for three hours followed by aging at selected temperatures from 400 to 700 °C for three hours. The resulting DSC responses over three cycles are illustrated in Figure 4.1c. After an initial decrease in TTs from the solutionized condition, TTs increased with aging temperature up to 650 °C and then decreased slightly with aging at 700 ºC. In particular, the transformation peaks were very sharp and stable after 550 °C-3h aging where thermal hysteresis had its lowest value of 33 °C. Forward transformation peak was below 100 °C for aging up to 450 °C-3h while it reached the maximum of ~160 °C after 650°C-3h aging.

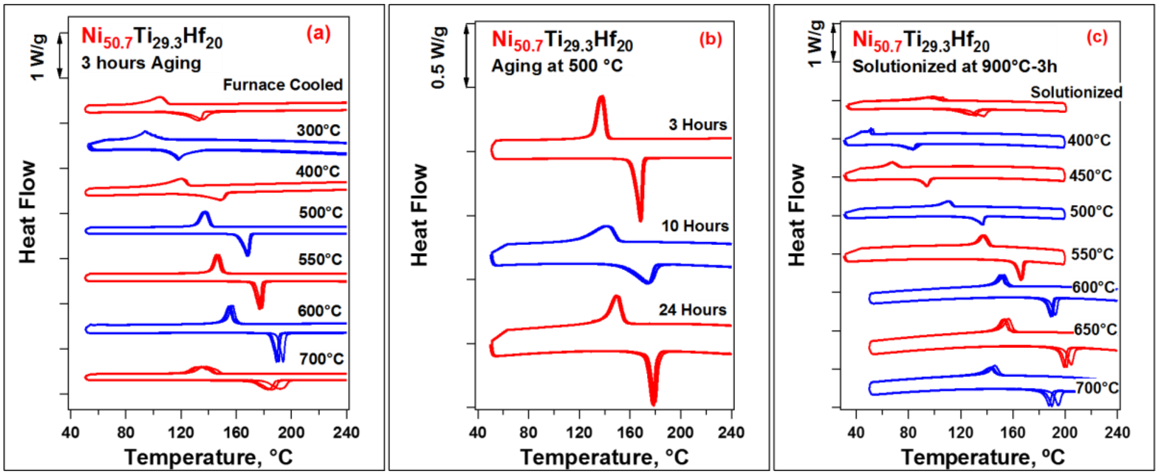

Figure 4.1: DSC curves for Ni$_{50.7}$Ti$_{29.3}$Hf$_{20}$ (a) aged for three hours at different temperatures after furnace cooled, (b) heat treated at 500 °C for various time and (c) three hours aging after solution treated.

Figure 4.2 represents the hardness measurements and transformation peak temperatures obtained from Figure 4.1 for the Ni$_{50.7}$Ti$_{29.3}$Hf$_{20}$ alloys aged after furnace cooled (Figure 4.2a) and solution treated (Figure 4.2b). Hardness increased from 506 HV in the furnace cooled condition to a maximum value of 580 HV after 500 °C-3 h aging, and then decreased with further increase in aging temperature. In solution treated condition, hardness increased from 337 HV to a maximum value of 560 HV for the sample aged at 600 °C-3h. It is clear from Figure 4.2 that the hardness and peak transformations in solutionized case is lower than the ones in furnace cooled samples which can be attributed to the size and volume fraction of precipitates. It has been shown in Chapter 3 that nanosize precipitates already existed in the furnace cooled 50.7Ni and further aging could alter the volume fraction of the precipitates which could be the reason for higher TTs in contrast with solutionized case.

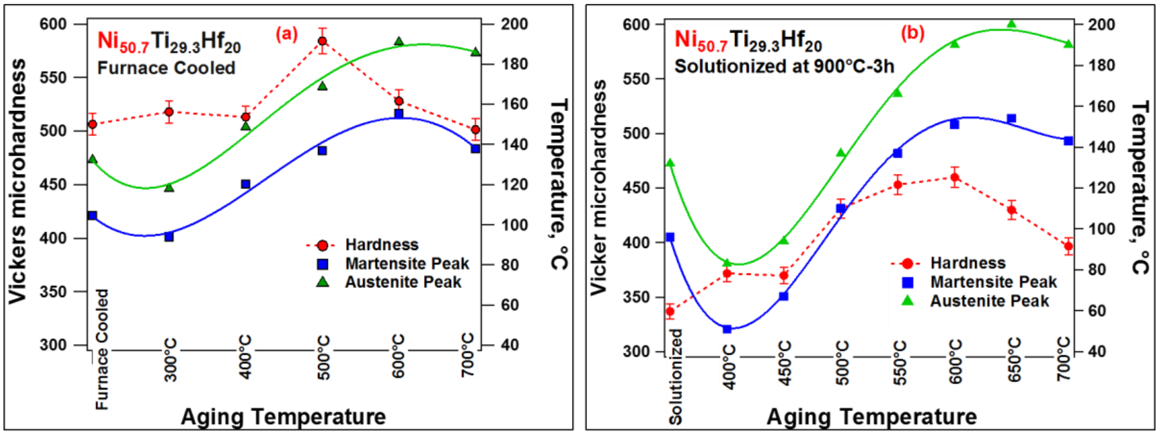

Figure 4.2: Vickers hardness measurements and transformation peak temperatures of $Ni_{50.7}Ti_{29.3}Hf_{20}$ as a function of three hours aging temperatures for (a) furnace cooled and (b) solutionized conditions.

Hardness, an indicative parameter of material strength, has a complex dependence on the size and distance between the precipitates [5, 13]. The material strength, as observed from the hardness results, reaches to its maximum value after three hours aging at 500-600 °C, which can be attributed to the formation of fine, densely spaced and coherent precipitates. The size of the precipitates and also the interparticle distance are a function of aging temperature. Moreover, the precipitates would tend to become semicoherent or incoherent as their size become large. At higher temperatures, the precipitates become larger in sized and consequently the interparticle distance increases, therefore, the strength of the alloy decreases.

The initial drop in TTs at low aging temperatures, compared to the furnace cooled or solutionized condition, is likely due to the formation of very small (a few nanometers in size) and finely spaced precipitates in the material. In this case there are two competing effects to be considered: the need for additional strain energy for nucleation and propagation where the matrix can transform to martensite and envelope the fine precipitates (which requires additional undercooling and thus lowers the TTs) and the depletion of Ni from the matrix, which would result in an increase in TTs [110, 116]. In the case of the low aging temperatures and times, the precipitates are small and strain energy dominates compositional affects resulting in an initial decrease in TTs, as previously demonstrated for similar NiTiHf and NiTiZr alloys [110, 116]. It has also been recently observed [142] that a precursor precipitate phase, H', to the typically observed H-phase [110, 111] occurs at low aging times and temperatures in this alloy under the same conditions where this drop in TTs is generally observed.

The eventual increase in the TTs with an increase in aging temperature is attributed to the growth of the precipitates, which further diminishes the Ni content in the matrix, such that compositional effects dominate and TTs increase. The final decrease in the TTs for aging temperatures beyond 600 °C is subsequently attributed to a reduced volume fraction of precipitate phase as the solvus temperature is approached resulting in less Ni-depletion of the matrix compared to intermediate aging conditions.

4.2.2 Microstructural Analysis

Figure 4.3a presents a high magnification micrograph of the $Ni_{50.7}Ti_{29.3}Hf_{20}$ alloy after 500 ºC-3h aging. Nanometric precipitates similar to those present in the furnace cooled 50.7Ni can be distinguished. By comparing Figures 3.2d and 4.3a, it is found that aging of the furnace cooled material results in an increased number of precipitates, but their size decreased after aging, being about 4–10 nm in width and 10–25 nm in length. Thus, the aging treatment modified the microstructure in the furnace cooled sample by decreasing the precipitate size and increasing the precipitate density. The smaller precipitate size in the aged $Ni_{50.7}Ti_{29.3}Hf_{20}$ alloy facilitated their absorption by the growing martensite plates, resulting in notably larger martensite plates in the aged samples (Figure 4.3b), compared to the furnace cooled condition (Figure 3.2c). Interestingly, 500 °C-3h aging of the furnace cooled 50.7Ni resulted in an increased density of precipitates and decreased precipitate size, relative to the original furnace cooled material. This would indicate that the nucleation rate of the precipitation reaction was significantly higher at 500 °C than at more elevated temperatures, while the growth rate was slower (in furnace cooled 50.7Ni the precipitates start to grow at temperatures above 500 °C during the furnace cooling treatment). TTs of $Ni_{50.7}Ti_{29.3}Hf_{20}$ were increased after aging for three hours at various temperatures due H-phase precipitation and resulting Ni depletion of the matrix.

Figure 4.3c is representative of TEM micrograph of the solution treated specimen at 900 °C for three hours. Similar to furnace cooled sample, the martensite observed in the solutionized case was identified as monoclinic B19'. In addition, The large martensite plate is related to the $(001)_{B19'}$ compound twinning mode, which is confirmed by the selected area diffraction pattern inserted in Figure 4.3c.

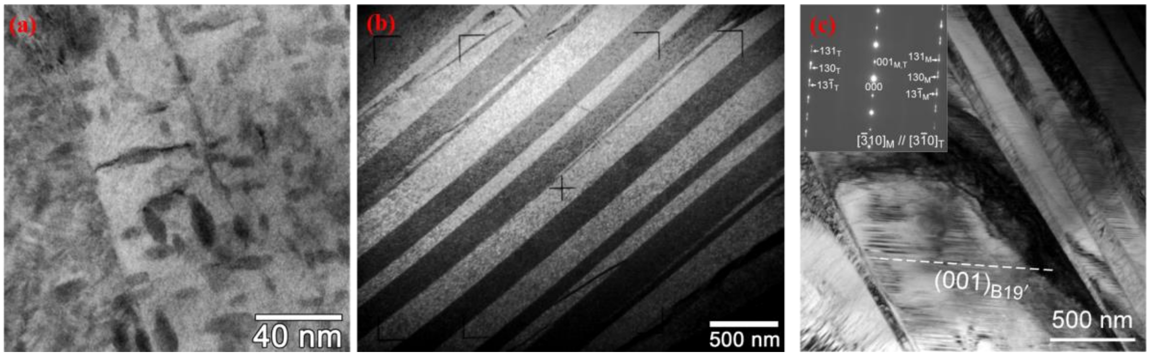

Figure 4.3: (a) High magnification, (b) lower magnification micrographs of $Ni_{50.7}Ti_{29.3}Hf_{20}$ aged at 500 ºC for 3h and (c) TEM micrograph of solutionized at 900 °C-3h.

4.2.3 Thermal Cycling and Isothermal Stress-Strain Behavior

Figure 4.4 illustrates the thermal cycling response of solution treated, 450 °C-3h aged and 550 °C-3h aged $Ni_{50.7}Ti_{29.3}Hf_{20}$ under applied constant compressive stress levels. It is good to notice that the heat treatments was done after material was solutionized at 900 °C. The stress was isothermally applied above the A_f temperature and then the sample was thermally cycled between a temperature below the M_f and a temperature above the A_f at a constant stress. After thermal cycle was completed, the stress was increased to the next level and the thermal cycling was repeated.

In agreement with the DSC results shown in Figure 4.1c, the TTs at 100 MPa were lower for 450 °C-3h aged condition and were higher for sample aged for three hours at 550 °C compared to the solutionized case. There was also the typical stress effect on TTs where the M_s for the solution treated material increased from 110 to 118 °C when stress raised from 100 to 500 MPa. Similarly the M_s was 85 °C at 100 MPa and increased linearly to 108 °C at 500 MPa for the 450 °C-3h aged sample. Also, the M_s had its maximum value of 148 °C when stress reached to 1000 MPa in 450 °C-3h aged samples. Furthermore, the M_s was shifted to the higher temperatures after 550 °C-3h aging where it increased from 143 °C at 100 MPa to 172 °C at 500 MPa and the M_s was more than 200 °C for applied stress of 1000 MPa.

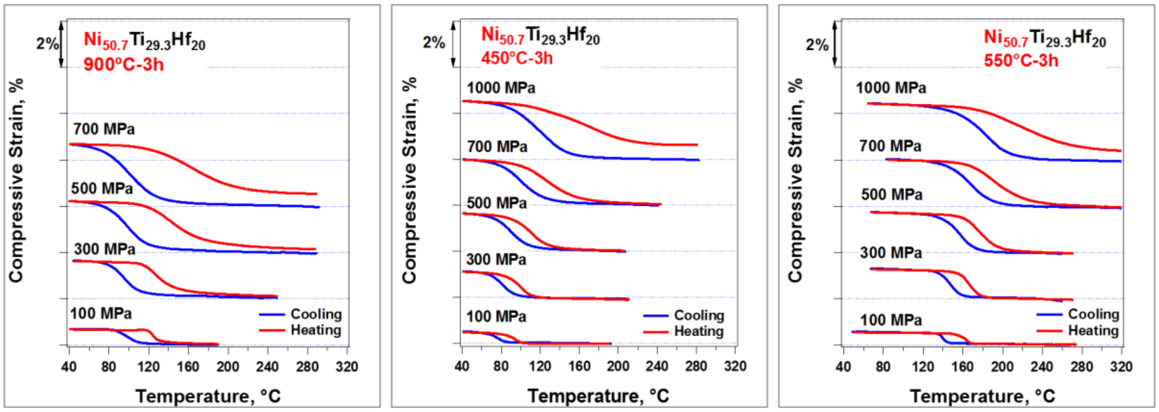

Figure 4.4: The strain vs. temperature response of $Ni_{50.7}Ti_{29.3}$ Hf_{20} in the solution treated, 450 °C-3h, and 550 °C-3h aged conditions.

At low stress levels, only a small shape change was observed due to the high stress required to reorient and/or detwin the martensite variants; however, at elevated levels of stress, a greater fraction of favorable martensite variants can form resulting in a greater net shape change. The total strain, increased from 0.6 to 1.9% and the thermal hysteresis increased from 27 to 49 °C when applied stress was increased from 100 to 500 MPa for the solution treated sample. A fully recoverable strain of 0.4% at 100 MPa and 1.4% at 500 MPa was observed in the 450 °C-3h aged sample. No irrecoverable strain was observed in the 450 °C-3h aged sample for an applied stress of 500 MPa and the thermal hysteresis was found to be below 30 °C for all stress levels except for 1000 MPa, where the hysteresis increased to 59 °C and irrecoverable strain of 0.6% was achieved. The recoverable strain was 0.4% at 100 MPa and 1.6% at 500 MPa for the alloy aged three hours at 650 °C. No irrecoverable strain was observed under 500 MPa while increasing stress to 1000 MPa resulted in total strain of 2.2% with corresponded irrecoverable strain of 0.5%. The thermal hysteresis for this sample was 22 °C at 500 MPa and reached to a maximum of 53 °C as stress increased to 1000 MPa.

The isothermal compression (superelastic cycling) result for the solution treated material is shown in Figure 4.5a. The alloy is not in fully austenite at temperatures below 130 °C, therefore, when the sample was loaded to a total strain of 4%, a residual strain was observed upon unloading. This residual strain was completely recovered after heating the unstressed sample above A_f. Almost fully recoverable cycle with 3% stain was observed at temperatures 130 °C and 150 °C where the critical stress for the forward martensite transformation (σ_{SIM}) was as high as 660 and 790 MPa, respectively. As the test temperature increases, σ_{SIM} increases accordingly, but the level of stress required for plastic deformation (σ_p) decreases [109]. Thus, the high σ_{SIM} and lower σ_p could result in some plastic deformation concurrent with the phase transformation, resulting in the irrecoverable strain observed after superelastic cycling at higher temperatures. For example, in the solution treated sample, a poor superelastic behavior with 0.8% residual strain was observed when the sample was loaded to 4% at 150 °C.

The stress-strain behavior of the 450 °C-3h aged sample is shown in Figure 4.5b. In contrast to the solutionized material, near perfect superelastic response with recoverable strain of 4% was observed at 110 °C. However, a further increase in test temperature with a concomitant increase in σ_{SIM} led to an irrecoverable strain after loading to 4% at temperatures above 130 °C. The σ_{SIM} achieved a high stress level of ~1000 MPa where the irrecoverable strain was 0.6% after 4% deformation at 170 °C.

The superelastic behavior of the 550 °C-3h aged sample is shown in Figure 4.5c. Loading to ~1000 MPa at 150 °C resulted in 0.5% residual strain. Upon heating the residual strain was fully recovered. When the same test was conducted at 170 °C, perfect superelastic behavior with 4% recoverable strain was observed. Full recovery of 3% strain was also experimented at 190 °C and 210 °C while the plastic strain increased as the sample was loaded to higher strain levels at this temperatures.

Nevertheless, the improvement of the superelastic behavior with aging can be attributed to the presence of coherent and fine precipitates, which strengthens the matrix. However, the superelastic window is very narrow since the material is not strong enough and plastic formation instantaneously was occurred with stress induced martensitic transformation as temperature increased. For instance, the superelastic behavior was just limited to one temperature for aged alloys.

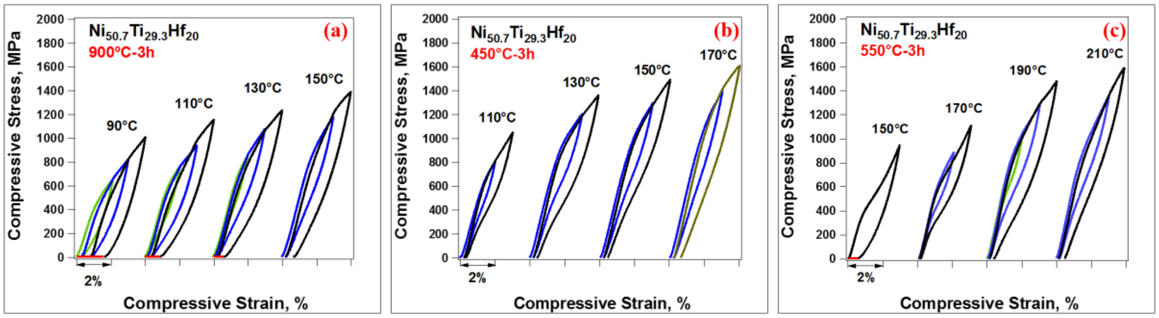

Figure 4.5: Stress-strain behavior in compression for the of $Ni_{50.7}Ti_{29.3}Hf_{20}$ alloy as a function of temperature for the (a) solution treated, (b) 450 °C-3h and (c) 650 °C-3h aged conditions.

4.2.4 Shape Memory Properties

Figure 4.6a illustrates the recoverable and irrecoverable strains of the solutionized and aged samples as functions of compressive stress extracted from the thermal cycling experiments shown in Figure 4.4. The recoverable strain (ε_{rec}) was minimum at the lowest applied stress level (100 MPa) for all specimen conditions. This is not surprising as ε_{rec} usually reaches a maximum at some intermediate stress level for all SMAs, as the amount of oriented martensite for maximum strain capability saturates. Therefore, for the

$Ni_{50.7}Ti_{29.3}Hf_{20}$ at 100 MPa, the microstructure would be expected to be a combination of oriented and some self-accommodated variants. The ε_{rec} increased steeply until 700 MPa and then saturated for most cases, as the ability to form oriented martensite variants saturated.

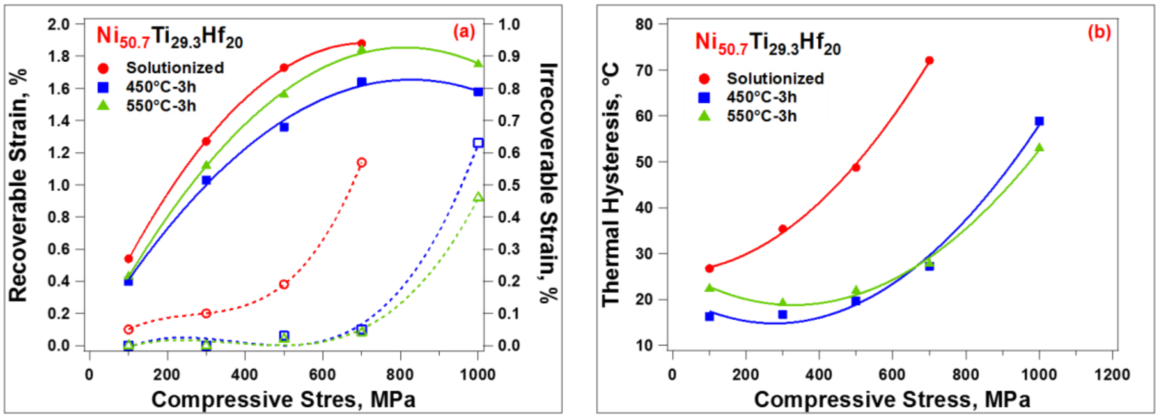

Figure 4.6: (a) Recoverable (solid line) and irrecoverable (dashed line) strains and (b) thermal hysteresis of $Ni_{50.7}Ti_{29.3}Hf_{20}$ as a function of applied compressive stress.

In the case of the solutionized sample, the ε_{rec} increased from 0.5% at 100 MPa to 1.7% at 500 MPa, where the value was nearly saturated, increasing further to only 1.8% by 700 MPa. What is noteworthy for the solutionized case is the existent irrecoverable strain (ε_{ir}) even at 100 MPa and increased to 0.6% when applied stress was 700 MPa due to low strength of the material. In contrast, the thermal cycling response of the aged samples exhibited a lower ε_{rec} since volume fraction of transforming regions decreased due to formation of non-transformable precipitates. A ε_{rec} of 0.4% was observed at 100 MPa and it increased to a maximum of 1.6% at 700 MPa, and upon further loading the strain was observed to decrease slightly while the ε_{ir} reached its highest amount of 0.6%. The thermal cycling response for the specimen aged at 550 °C for three hours shows that the ε_{re} increased slightly in comparison to the 450 °C-3h aged specimen, with only 1% ε_{re}

observed at 100 MPa. Almost Fully stable shape recovery was experienced only up to 700 MPa, while further loading to 1000 MPa resulted in ε_{ir} of 0.5%.

In martensitic transformations, there are two key energy dissipative processes that govern the hysteresis. The first process is the energy dissipated in the form of frictional work and the second one is the dissipation of energy due to plastic deformation. The magnitude of the total energy dissipation is reflected in the thermal or stress hysteresis. It should be kept in mind, in actuator type applications, energy dissipation negatively impacts the efficiency of SMA devices.

Figure 4.6b shows the effects of aging and stress on the thermal hysteresis of the Ni-rich $Ni_{50.7}Ti_{29.3}Hf_{20}$ alloys. The thermal hysteresis was generally observed to increase with stress for the solutionized case while remained nearly constant with stress up to 500 MPa and then increased for the aged conditions. The maximum thermal hysteresis observed was for the solutionized condition, which increased from 27 °C at 100 MPa to 72 °C at 700 MPa. This increase in thermal hysteresis with stress is consistent with the greater plastic deformation observed in solution treated sample. In contrast, it is clear that aging results in a much stronger matrix as demonstrated by the increased hardness values (Figure 4.2b) and little or no irrecoverable strains during thermal cycling up to 700 MPa, which in turn results in a small thermal hysteresis.

Figure 4.7 shows the stress dependence of the M_s temperature, determined from the thermal cycling results shown in Figure 4.4. The results indicate that the critical stress for initiating the forward transformation has a linear relationship with temperature which satisfies the CC relation. Based on this relationship, the CC slope is 23.7 MPa/°C, 13.8 MPa/°C and 13.7 MPa/°C for the solutionized, 450 °C-3h and 650 °C-3h aged conditions, respectively. The results are in the good agreement with DSC responses where the TTs decreased with aging at 450 °C-3h and then increased for 550 °C-3h aged sample. In contrast with furnace cooled $Ni_{50.7}Ti_{29.3}Hf_{20}$, higher CC slopes and lower strength of the material (Figure 4.2) could be the reasons for poor superelastic behavior in solutionized condition.

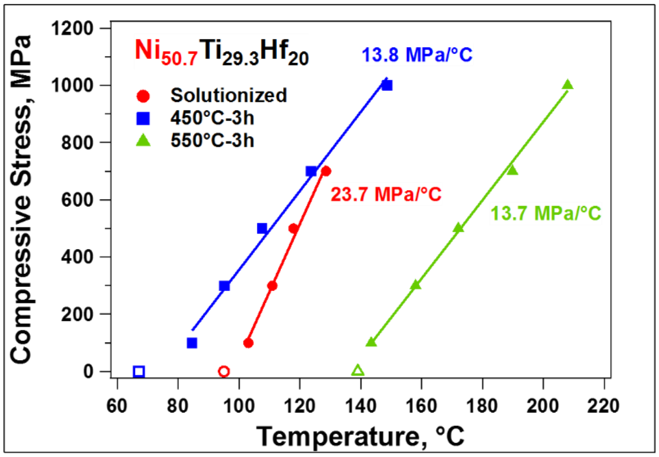

Figure 4.7: Applied stress vs. M_s for the $Ni_{50.7}Ti_{29.3}Hf_{20}$ alloy

4.2.5 $Ni_{50.7}Ti_{29.3}Hf_{20}$ Conclusions

The effects of various heat treatments on the shape memory properties of a polycrystalline $Ni_{50.7}Ti_{29.3}Hf_{20}$ alloy were investigated and the main findings can be summarized as follows:

(1) TTs of $Ni_{50.7}Ti_{29.3}Hf_{20}$ were raised after three hours aging due to Ni depletion of the matrix due to formation of Ni-rich precipitates. Aging for three hours at 600 °C increased the martensite peak temperature from 104 °C in the furnace cooled condition to 155 °C. After solution treated, TTs decreased and the strength of the material diminished. TTs were particularly stable during repeated thermal cycling after three hours aging at temperatures 500 °C and 550 °C.

(2) Thermal treatments can be used to alter the size and coherency of the precipitates, which in turn can affect the morphology of the resulting martensite phase, and both factors directly influence the shape memory and mechanical properties of the Ni-rich $Ni_{50.7}Ti_{29.3}Hf_{20}$. In particular, it was found that 500 °C-3h aging resulted in notably larger martensitic plates since the volume fraction of precipitates increase while the size of them decreased in compared with furnace cooled sample. Also $(001)_{B19'}$ compound internal twins was observed in solutionized condition.

(3) Aging improved the shape memory and mechanical properties of the solutionized $Ni_{50.7}Ti_{29}Hf_{20}$ alloy. In aged conditions, the alloy exhibits good shape memory behavior with less 2% recoverable strain at stress levels up to 700 MPa without training. Perfect superelastic behavior at temperatures as high as 170 °C with 3% recoverable strain was observed for 550 °C-3h aged sample while the superelastic window was very narrow.

4.3 Experimental Results: $Ni_{51.2}Ti_{28.8}Hf_{20}$

4.3.1 Transformation Temperatures

The DSC responses of three hours heat treated $Ni_{51.2}Ti_{28.8}Hf_{20}$ alloys are shown in Figure 4.8a. The DSC curves for solution-treated and samples heat treated up to 500 °C have not been shown in Figure 4.8a since no martensitic transformation was observed even when they were cooled down to –100 °C. Transformation peak temperatures were shifted to above room temperature as heat treatment temperature was elevated above 550 °C. Also, transformation peaks show excellent thermal stability after three hour aging at 550–650 °C, while aging at higher temperatures deteriorated the thermal stability of transformation peaks, as clearly illustrated in Figure 4.8a.

Figure 4.8b presents Vickers microhardness, M_p and A_p of aged samples as a function of heat treatment temperature. Hardness, which measures the resistance of the material to deform plastically, reached its maximum value of 678 after 550 ºC-3h aging and then drastically decreased to 528 as aging temperature was increased to 750 ºC. It is worth to mention that the alloy is austenite at room temperature after aging at low temperatures, while it is martensite as heat treatment temperature was increased above 550 °C. Figure 4.8b clearly shows that M_p was increased from 14 °C to the maximum value of 89 °C with increasing aging temperature from 550 to 650 °C. It is obvious that A_p followed the same trend as M_p and it was increased from 73 to 147 °C as the aging temperature was increased from 550 to 650 °C.

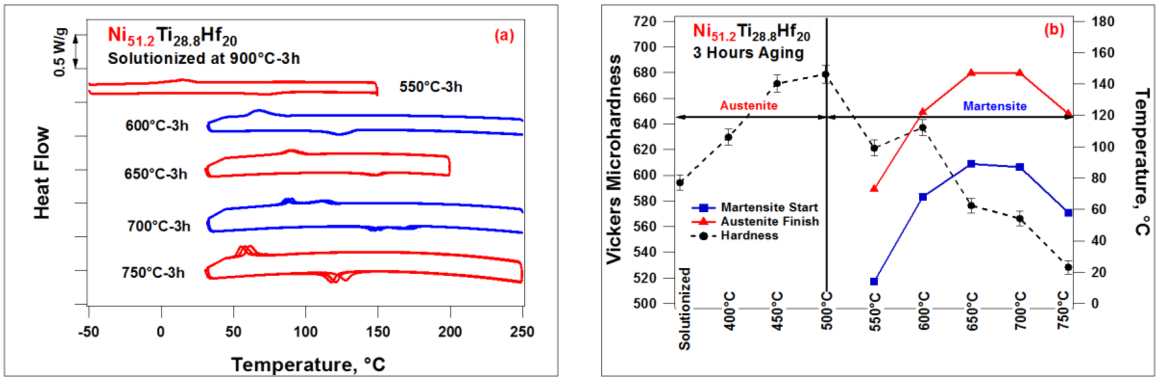

Figure 4.8: (a) DSC responses of $Ni_{51.2}Ti_{28.8}Hf_{20}$ after three hours aging at various temperature of 550 to 750 °C and (b) Vickers microhardness and transformation peak temperatures as a function of three hours aging.

The higher hardness value after three hours aging at 450 °C can be attributed to the fact that the material is austenite at room temperature. Whereas, martensitic transformation took place at around room temperature for 550 °C-3h and TTs reached its maximum values after aging at 650 °C-3h. The increase of TTs is attributed to formation of precipitates which alters the composition of the matrix where more Ni content was depleted from the matrix. However, three hours aging above 650 °C decreased the TTs, which indicates that the volume fraction of precipitates decrease at higher temperatures. Thus, three heat treatment temperatures of 450 °C, 550 °C and 650 °C were selected to study the effects of precipitates characteristics on shape memory behavior of Ni-rich $Ni_{51.2}Ti_{28.8}Hf_{20}$.

4.3.2 Microstructural Analysis

TEM observations were conducted to investigate the effects of aging on the microstructure of $Ni_{51.2}Ti_{28.8}Hf_{20}$. Figure 4.9 shows a bright-field image and the corresponding SAD pattern obtained from the sample solution-treated at 900 °C for three hours. Precipitate formation is not confirmed in Figure 4.9a and there are no other diffraction spots except for those of B2 austenite phase in Figure 4.9b. It is worth noting that diffuse streaks can be seen around the austenite reflections in the SAD pattern. Similar diffuse streaks have been reported in $Ni_{52}Ti_{42}Zr_6$ [143] and $Ni_{45.3}Ti_{39.7}Hf_{10}Pd_5$ [125] alloys, suggesting the formation of extremely fine precipitates (H or H' phase) that are difficult to be observed by conventional TEM observation. High resolution TEM observations are now in progress to determine the size and the crystal structure of the fine precipitates.

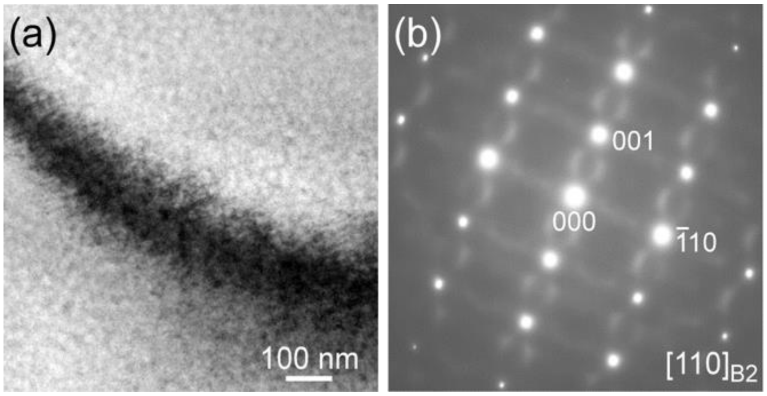

Figure 4.9*:* (a) Bright-field TEM image and (b) the corresponding SAD pattern of $Ni_{51.2}Ti_{28.8}Hf_{20}$ solution-treated at 900 °C for three hours.

The microstructure of the 450 °C-3h aged condition is shown in Figure 4.10a and its higher magnification image is shown in Figure 4.10b. Aging at 450 °C for three hours produced very fine precipitates with less than 15 nm in size. The high hardness of the 450 °C-3h aged sample (Figure 4.8b) could be attributed to the formation of the homogeneously distributed fine and coherent precipitates. In the SAD pattern shown in Figure 4.10c, in contrast to the solution-treated condition, a lot of small diffraction spots of precipitates are clearly observed in addition to strong austenite reflections. The fine precipitates formed after 450 °C-3h aging were identified as H-phase according to the diffraction pattern. The representative reflections of H-phase are at 1/3 positions along $<110>_{B2}^*$ in reciprocal space.

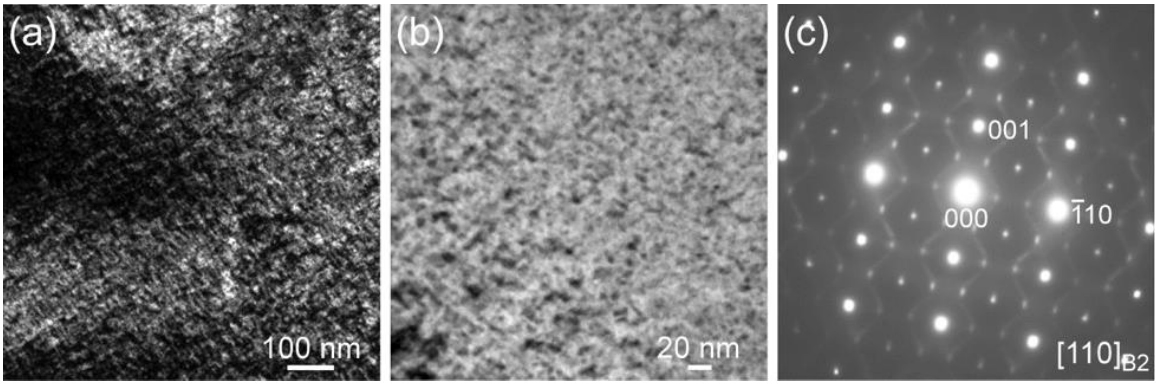

Figure 4.10: (a and b) Bright-field TEM images and (b) the corresponding SAD pattern of $Ni_{51.2}Ti_{28.8}Hf_{20}$ aged at 450 °C for three hours.

Figures 4.11a and b show the low and high magnification bright-field images obtained from the 550 °C-3h aged condition, respectively. Aging at 550 °C for three hours resulted in the formation of larger precipitates (~15–20 nm) with lower density when compared to 450 °C-3h aging. Figure 4.11c is a bright-field image showing almost the same area in Figure 4.11b but taken under a condition that the sample was tilted to make martensite satisfy Bragg’s law so that martensite plates are visible. Thin martensite plates are formed between fine precipitates. Figure 4.11d and e show the corresponding SAD pattern and the key diagram, respectively. The SAD pattern consists of diffraction spots of

H-phase precipitates and twinned B19′ martensite. According to the diffraction pattern, the martensite plates shown in Figure 4.11c are related to $(0\bar{1}1)_{B19'}$ type I twinning.

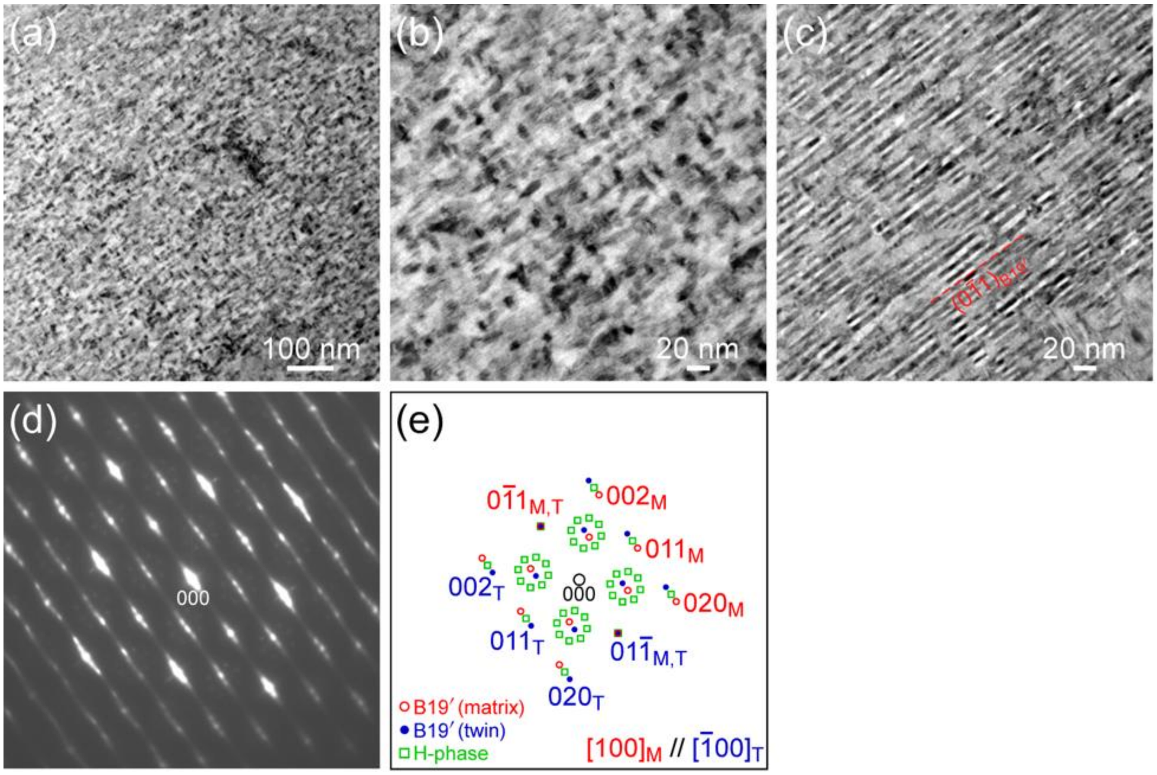

Figure 4.11: Bright-field TEM images showing (a and b) H-phase precipitates and (c) martensite in $Ni_{51.2}Ti_{28.8}Hf_{20}$ aged at 550 °C for three hours. (c) SAD pattern and (d) the corresponding key diagram where subscripts M and T indicate matrix and twin, respectively.

Figure 4.12 shows a TEM micrograph of the 650 °C-3h aged condition. Comparing Figure 4.12a to Figures 4.10a and 4.11a, it is clear that high temperature aging increases precipitation size and decreases the volume fraction of precipitates. H-phase precipitates with ~40–70 nm in size were observed after aging at 650 °C for three hours. Figure 4.12b is a higher magnification image showing martensite plates formed between precipitates. The martensite plates in the 650 °C-3h aged condition are thicker than those of the 550 °C-3h aged condition (Figure 4.11c), which is due to larger interparticle distance after aging at higher temperature. $\{011\}_{B19'}$ type I twinning is observed at the intervariant boundaries of martensite in Figure 4.12b. Figure 4.12c is the corresponding SAD pattern showing reflections of H-phase precipitates and $\{011\}_{B19'}$ type I twins.

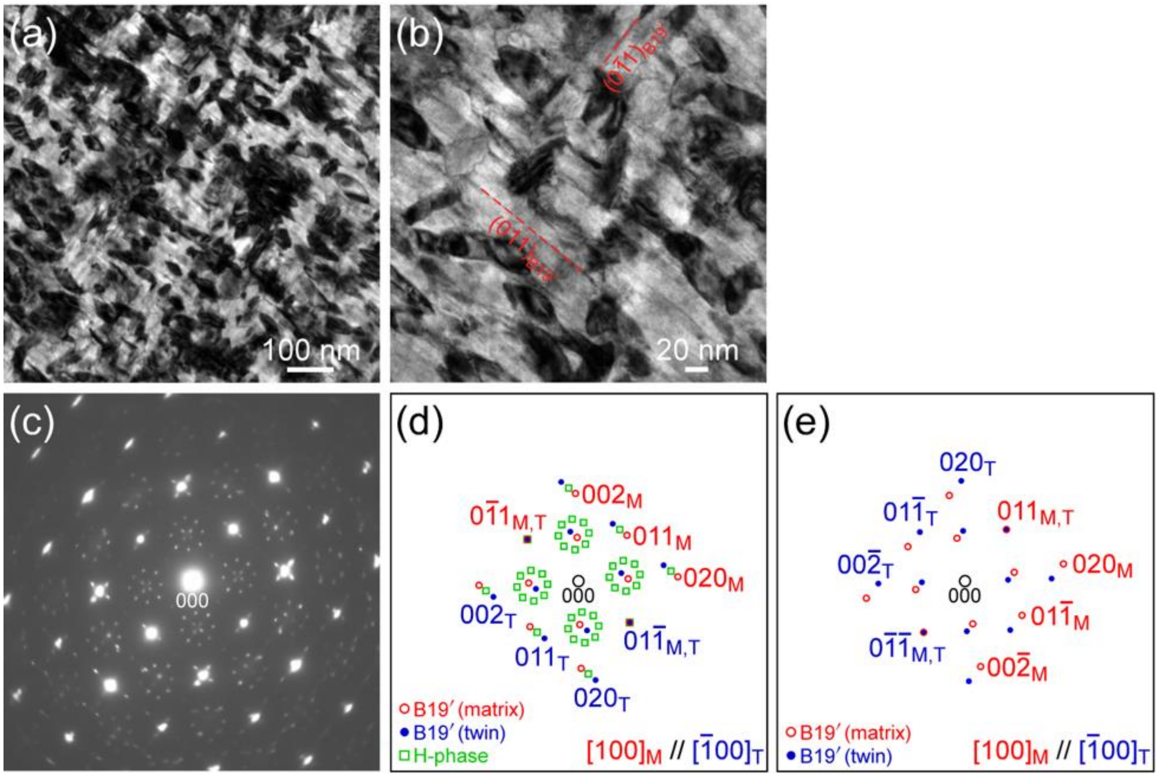

Figure 4.12: (a and b) Bright-field TEM images of $Ni_{51.2}Ti_{28.8}Hf_{20}$ aged at 650 °C for three hours. (c) SAD pattern and (d and e) the corresponding key diagrams where subscripts M and T indicate matrix and twin, respectively.

Figures 4.12d and e represent the key diagrams of the SAD pattern, where Figure 4.12d shows the reflections of H-phase and $(0\bar{1}1)_{B19'}$ type I twinning and Figure 4.12e shows those of $(011)_{B19'}$ type I twinning. As a result, it is concluded that the thickness of martensite plates depends on interparticle distance and intervariant boundaries are related to $\{011\}_{B19'}$ type I twinning in $Ni_{51.2}Ti_{28.8}Hf_{20}$.

4.3.3 Shape Memory Effect under Stress

Thermal cycling under compressive stress responses of $Ni_{51.2}Ti_{28.8}Hf_{20}$ after three hours aging at 450 °C, 550 °C and 650 °C are illustrated in Figure 4.13. The shape memory effect behavior of solution-treated cannot be observed due to low TTs. Shape memory behavior was not clearly experimented under low stresses below 700 MPa for 450 °C-3h aged sample as shown in Figure 4.13a. This could be attributed to the fact that the applied stress level was not sufficient to form favorable martensite variants and also low TTs. The M_s was raised from –20 to 76 °C as stress was increased from 700 to 1700 MPa and almost perfect dimensional stability with recoverable strain of ~1.3% was observed under high stress level of 1500 MPa. The total strain was 1.4% with a corresponding irrecoverable strain of 0.1% as the applied stress was increased to 1700 MPa. In addition, thermal hysteresis decreased from 28 to 22 °C when stress was elevated from 700 to 1700 MPa.

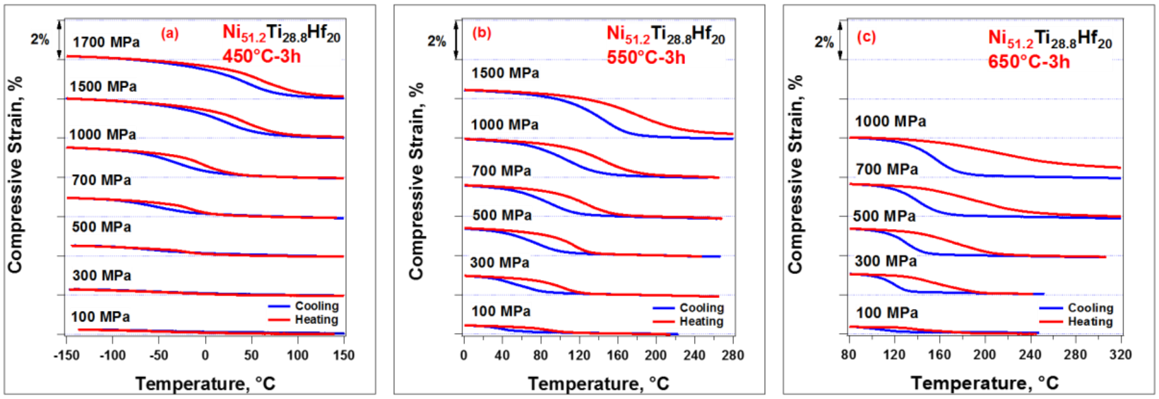

Figure 4.13: Thermal cycling under compressive stress of $Ni_{51.2}Ti_{28.8}Hf_{20}$ in (a) 450 °C-3h, (b) 550 °C-3h and (c) 650 °C-3h aged conditions.

It is clear from Figure 4.13b that the shape memory behavior can even be observed at low stress levels after 550 °C-3h aging. The M_s was 55 °C under 100 MPa and increased to 172 °C under 1500 MPa. Total strain was increased from 0.3% to its maximum value of

2.1% when applied stress was raised from 100 to 1500 MPa. Whereas, irrecoverable strains of 0.03% at 700 MPa and maximum of 0.3% at 1500 MPa were observed. Thermal hysteresis was decreased from 40 to 36 °C when the stress was increased from 100 to 700 MPa and it reached to its maximum value of 45 °C at 1500 MPa. In contrast, only 0.05% irrecoverable strain was observed at 1500 MPa and thermal hysteresis was lower when the sample was aged at 450 °C-3h.

Figure 4.13c shows the SME under compressive stress of $Ni_{51.2}Ti_{28.8}Hf_{20}$ after 650 °C-3h aging. It is clear that the TTs were increased to the temperatures above 100 °C which qualifies the material as HTSMAs. The M_s was raised from 125 to 176 °C with increasing stress from 100 to 1000 MPa. On the other hand, material exhibited a poor dimensional stability under 1000 MPa where the total strain of 1.8% and a corresponding irrecoverable strain of 0.5% were observed. Thermal hysteresis were raised from 34 to 80 °C as stress level was increased from 100 to 1000 MPa, which is higher than the values observed for the other two aged conditions.

4.3.4 Superelastic Behavior

Isothermal stress vs. strain responses of solutionized and aged $Ni_{51.2}Ti_{28.8}Hf_{20}$ alloys at the selected temperatures are shown in Figure 4.14. It is clear that mechanical responses of $Ni_{51.2}Ti_{28.8}Hf_{20}$ alloys are highly test and aging temperature dependent. In solutionized samples, almost full recovery with a negligible irrecoverable strain was observed up to 4% deformation in the temperature range of –20 to 20 °C. The σ_{SIM} was increased from 780 to 880 MPa as the test temperature was elevated from –20 to 20 °C. Alternatively, aging at 450 °C-3h was resulted in full recovery of 4% deformation for the temperature window from –40 to 40 °C. The σ_{SIM} was increased from 890 to 1250 MPa when the test temperature was amplified from –40 to 40 °C. Full recovery was even observed when a high stress level of 2 GPa was achieved and the dissipation of energy during the phase transformation was lower than the solution-treated condition.

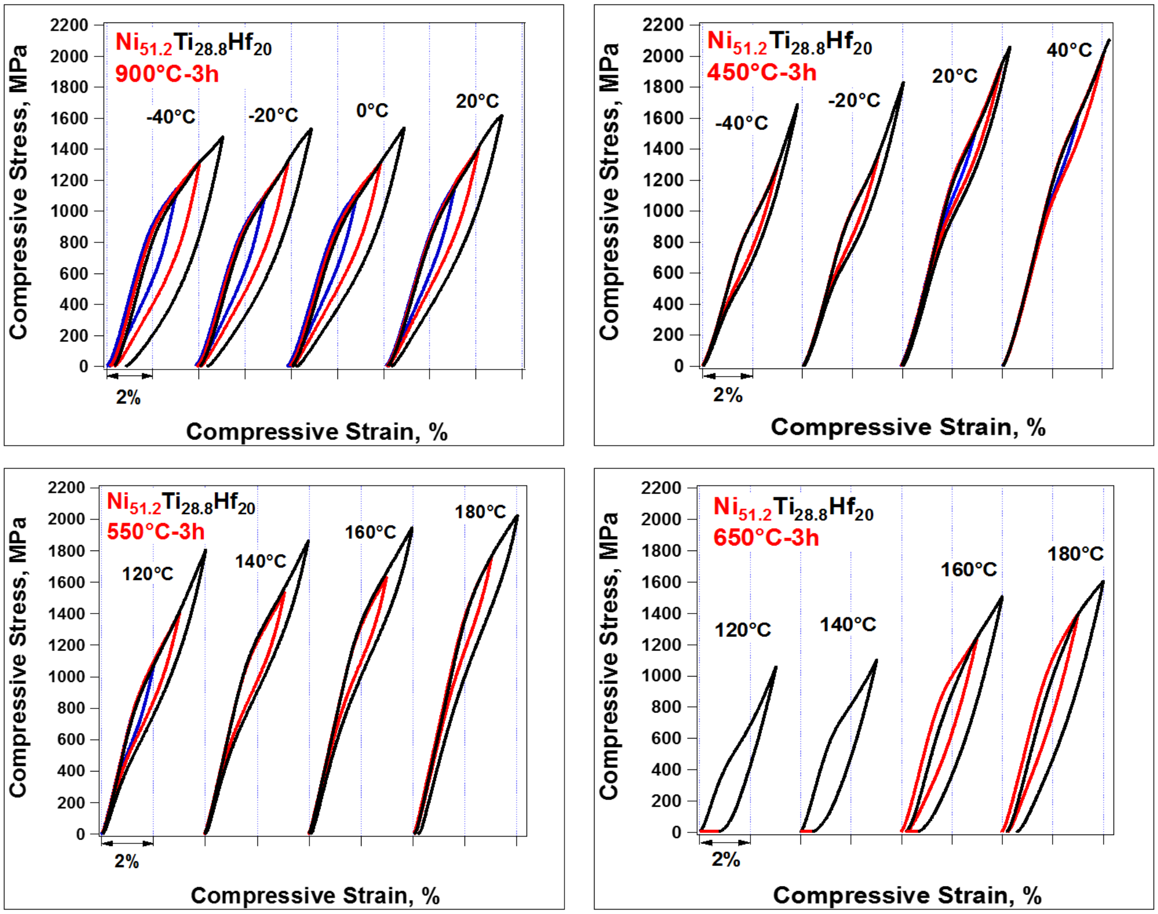

Figure 4.14: Isothermal stress vs. strain behavior of $Ni_{51.2}Ti_{28.8}Hf_{20}$ for solutionized, 450 °C-3h, 550 °C-3h and 650 °C-3h aged conditions at the selected temperatures.

Perfect superelastic behavior was observed at high temperatures from 120 to 160 °C with full recovery of 4% strain after 550 °C-3h aging. At 180 °C, total strain of 3% was fully recovered while further deformation to 4% produced a small irrecoverable strain of 0.15% upon unloading while the material was loaded to 2 GPa. The critical stress to initiate the martensitic transformation was increased from 525 to 1415 MPa as test temperature was elevated from 120 to 180 °C. It is clear that the stress-strain cycles were very stable after 450 °C-3h and 550 °C-3h aging while the mechanical hysteresis was increased with strain in solutionized condition. Further aging at 650 °C-3h was resulted in poor superelastic behavior as shown in Figure 4.14. Remained strains were 0.8% and 0.6% after loading to 1000 MPa at 120 and 140 °C, respectively, and fully recovered upon heating above A_f. The stresses required for austenite to transform to martensite phase were 365 MPa and raised to 990 MPa as temperature was increased from 120 to 180 °C, while irrecoverable strain of 0.4% was observed after 4% deformation at 180 °C.

4.4 Discussion of Results: $Ni_{51.2}Ti_{28.8}Hf_{20}$

4.4.1 Transformation Characteristics

Martensitic transformation of $Ni_{51.2}Ti_{28.8}Hf_{20}$ highly depends on the precipitation characteristics. At low aging temperatures, very fine H or H’ phase precipitates with short interparticle distances were homogenously distributed throughout the structure and suppress the nucleation of martensite. It has been also shown that stress was not sufficient to initiate the nucleation of martensite and select the favorable martensite variants at low stress levels after 450 °C-3h aging. Above 500 MPa the volume fraction of favorably oriented martensite variants increased gradually with stress but still the transformation strain was low. On the other hand, TTs were shifted to the higher temperatures as precipitates became larger in size after 650 °C-3h aging where martensite plates could form in the space between the precipitates. As mentioned in the introduction of this chapter, the strength of material strongly depends on the precipitate size and the space between them. Fine coherent precipitates with short interparticle distances formed in the material after aging at low temperatures which they act as obstacles against dislocation motion and improve the strength of the alloy. The size and space between the precipitates increase after aging at high temperatures (> 550 °C) and the strengthening effect diminishes. The high strength can also be attributed to twinning morphology in this material. In addition, It has been reported [62] that small precipitates are sheared by dislocation cutting through them which new interface between precipitates and matrix is produced and increased the interfacial energy, hence, the strength of material improved. In the case of bigger precipitates with longer interparticle distances, dislocations could bypass the precipitates by looping around them instead of cutting through them.

Recoverable strains were determined as the difference between the total and irrecoverable strains which were extracted from the thermal cycling under stress results shown in Figure 4.13 and they are plotted in Figure 4.15a. The recoverable strains were increased with stress and reached its maximum value of 1.3% and 1.8% at 1500 MPa for 450 °C-3h and 550 °C-3h aged conditions, respectively, and they were saturated above 1200 MPa for both conditions. Whereas, recoverable strain reached to its peak value of 1.4% at 700 MPa and then decreased instantaneously with stress for the 650 °C-3h aged sample, which has the lowest strength. Initial increase of recoverable strain with applied stress is attributed to the increase in the volume fraction of favorable martensite variants with stress. The decrease of recoverable strain at high stress levels can be ascribed to formation of plastic deformation during the martensitic transformation, hence, increased amount of irrecoverable strain.

It is known that the transformation strain depends on the size and volume fraction of the precipitates in NiTiHf alloys [114, 137]. For $Ni_{51.2}Ti_{28.8}Hf_{20}$, very fine precipitates with small interparticle spacing are formed after low temperatures aging as shown by the

TEM images in Figure 4.10. It should be noted that when the precipitate size and interparticle distance is small, large martensite plates form to absorb the particles [110, 136-138]. At high aging temperatures, the precipitates became larger in size with longer interparticle distances and martensite plates could nucleate and propagate in the space between the precipitates (Figure 4.12). The recoverable strain slightly increased with aging temperature, which can be attributed to a slight decrease in volume fraction of non-transformable precipitates with aging temperature which was previously observed in NiTi alloys [34, 61, 144]. As mentioned before, the strength of material diminishes with increase in precipitate size and interparticle distance. Irrecoverable strains were negligible at low stress levels and then increased as transformation strain saturates at stress levels above 1200 MPa for 450 °C-3h and 550 °C-3h aged conditions. However, irrecoverable strain was drastically increased when stress was raised above 700 MPa and reached to 0.5% under 1000 MPa after 650 °C-3h aging.

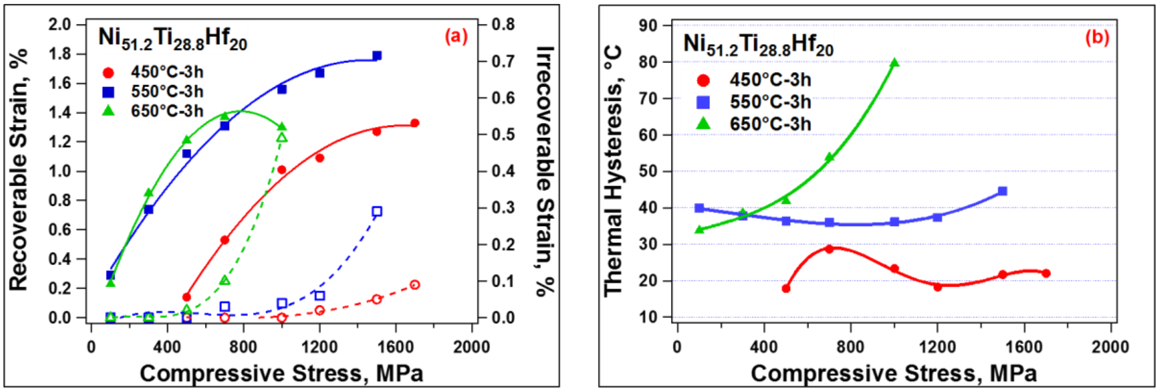

Figure 4.15: (a) Recoverable (solid line) and Irrecoverable (dashed line) strains and (b) Thermal hysteresis of $Ni_{51.2}Ti_{28.8}Hf_{20}$ in 450 °C-3h, 550 °C-3h, and 650 °C-3h aged conditions.

Figure 4.15b illustrates the thermal hysteresis of aged $Ni_{51.2}Ti_{28.8}Hf_{20}$ which was determined as the difference between the midpoints of cooling and heating curves of thermal cycling under stress results shown in Figure 4.13. Thermal hysteresis was below 30 °C for the 450 °C-3h aged sample where the maximum irrecoverable strain was 0.1% at the high stress of 1700 MPa. However, thermal hysteresis was increased above 30 °C and large irrecoverable strains of 0.3% and 0.5% were obtained at the stress levels of 1500 and 1000 MPa, after 550 °C-3h and 650 °C-3h aging, respectively. The low thermal hysteresis and irrecoverable strain after 450 °C-3h aging can be attributed to the high strength of the material due to formation of fine precipitates which act as pinning sites against dislocation movement. It is clear that the decrease in thermal hysteresis with stress is due to the increase of volume fraction of favorable martensite variants, which results in decreased of dissipation energy due to less interaction between martensite variant interfaces. On the other hand, thermal hysteresis was increased with stress in 650 °C-3h aged samples, which linked to the lack of precipitation hardening due to the formation of large particles that leads to increase of plastic deformation with stress. It is worth to mention that the mechanical and thermal hysteresis are in a good correlation with each other where the mechanical hysteresis has the lowest value for 450 °C-3h aged condition and high stress hysteresis was observed after 650 °C-3h aging.

4.4.2 Martensitic Transformation Behavior

Transformation temperatures were determined from thermal cycling responses by using the tangent line method and phase diagrams of aged samples are illustrated in Figure 4.16. The TTs were shifted to the higher temperatures with stress and aging temperature. It is significant to mention that the A_s was lower than the M_s for all the aged samples which can be attributed to the high elastic strain stored during martensitic transformation [124, 145, 146]. Although, the difference between the M_s and M_f is greater after 450 °C-3h aging in contrast to 650 °C-3h aged condition. This indicates that larger undercooling is needed to complete the forward transformation after 450 °C-3h aging and the low strain-temperature slope during the forward transformation designates the high elastic energy storage during austenite to martensite transformation. During heating, stored elastic energy helps the back transformation that results in decreased A_s. The high stored elastic energy can be due to i) the variation in lattice parameters of the transformation phases, ii) alteration in martensite morphology (e.g. twining types) and iii) strong internal stresses due to precipitation. It is clear from Figure 4.16 that, M_s and A_s are close to each other at low stress levels while the difference between them (M_s–A_s) increases with stress. Thus, two types of transformations that are classified as type I ($A_s > M_s$) and type II ($A_s < M_s$) transformations [39] are observed in this alloy system. Similar behavior was observed in furnace cooled 50.7Ni and 52.0Ni (Figure 3.4) where M_s was greater than A_s at stress levels above 500 MPa. This behavior can be explained by thermodynamical analysis where M_s and A_s are conveyed by the following equations [33]:

$$M_s = T_0 - \frac{\Delta G_{el}^{i}}{|\Delta S|} - \frac{\Delta G_{dis}}{|\Delta S|} \tag{4.3}$$

$$A_s = T_0 - \frac{\Delta G_{el}^{f}}{|\Delta S|} + \frac{\Delta G_{dis}}{|\Delta S|} \tag{4.4}$$

In the equations 4.3 and 4.4, T_0 is the chemical equilibrium temperature, ΔS is the change in the chemical entropy, ΔG_{dis} is the dissipation energy, ΔG_{el}^{i} is the initial elastic energy during nucleation of martensite variants and ΔG_{el}^{f} is the total elastic energy when martensitic transformation fully completed. It is evident form Figure 4.16 that the transformation behavior in the aged $Ni_{51.2}Ti_{28.8}Hf_{20}$ alloys can be categorized as type II (A_s

< M_s) transformation at high stress levels above 300 MPa. The temperature different between M_s and A_s, $\Delta T_{(Ms\text{-}As)}$, can be expressed as :

$$\Delta T_{(Ms-As)} = \left(\Delta G_{el}^{f} - \Delta G_{el}^{i}\right) - 2\Delta G_{dis} \tag{4.5}$$

Equation 4.5 clearly shows that the difference between M_s and A_s is related to stored elastic strain and dissipation energies of the system. Type I transformation is associated with the negative $\Delta T_{(Ms\text{-}As)}$ which indicates that the amount of dissipation energy is larger than stored elastic energy. Alternatively, for positive $\Delta T_{(Ms\text{-}As)}$, the stored elastic energy is greater than twice of dissipation energy.

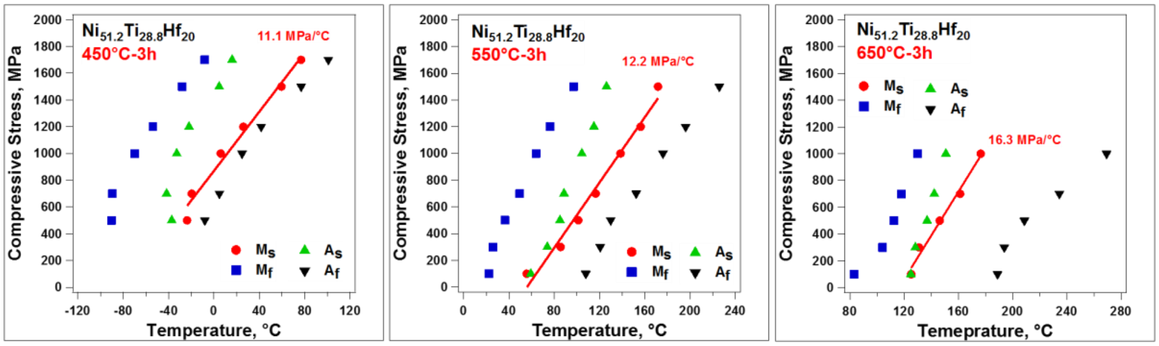

Figure 4.16: Phase diagrams of $Ni_{51.2}Ti_{28.8}Hf_{20}$ in 450 °C-3h, 550 °C-3h, and 650 °C-3h aged conditions.

The experimental values of $\Delta T_{(Ms\text{-}As)}$ as functions of applied stress and aging conditions are summarized in Table 4.1. Mostly, type II transformation is observed except in the 550 °C-3h aged alloys where M_s is less than A_s under 100 MPa (type I transformation). The $\Delta T_{(Ms\text{-}As)}$ parameter increases with stress as shown in Table 4.1. Based on equation 4.5, the difference between the total stored elastic energy and the dissipation energy increases with stress since the difference between M_s and A_s is greater at higher stress level as shown in Table 4.1. Meanwhile, $\Delta T_{(Ms\text{-}As)}$ is decreased from 38 to 25 °C at

1000 MPa as the aging temperature increased from 450 to 650 °C. This could be attributed to the effects of precipitates on the morphology of martensite, compatibility of transforming phases and strength of material. The strength of material was improved due to formation of nanosize precipitates with short interparticle distances after 450 °C-3h aging, as a consequence, no plastic deformation was produced during thermal cycling under 1000 MPa and low thermal hysteresis (< 30 °C) was observed in this case in contrast to other aged conditions as illustrated in Figure 4.15. Thus, improvement of the strength of the matrix after 450 °C-3h aging increased the elastic energy storage and decrease the dissipation of energy during forward transformation. However, the strength of the alloy diminished as the size of precipitates and distance between them increased after 650 °C-h aging, hence, large plastic deformation of 0.3% and high thermal hysteresis of 80 °C was observed at 1000 MPa. In contrast to low aging temperatures, high applied stress increased the stored elastic energy and also dissipation energy where the difference between M_s and A_s decreased. In addition, formation of H-phase precipitates may alter the lattice parameters of transforming phases, martensite morphology (i.e. twinning type and density) and compatibility of the transforming phases, which in turn affect the amount of stored elastic energy and dissipation energy.

Table 4.1: Transformation temperatures (M_s and A_s) and $\Delta T_{(Ms\text{-}As)}$ at different stress levels.

	450 °C-3h			**550 °C-3h**			**650 °C-3h**		
Stress	**M_s**	**A_s**	**$\Delta T_{(Ms\text{-}As)}$**	**M_s**	**A_s**	**$\Delta T_{(Ms\text{-}As)}$**	**M_s**	**A_s**	**$\Delta T_{(Ms\text{-}As)}$**
100	_	_	_	56	59	–3	125	125	0
300	_	_	_	86	77	9	131	128	3
500	–24	–37	13	101	85	16	146	137	9
700	–20	–42	22	117	89	28	161	142	19
1000	6	–33	39	139	104	35	176	151	**25**
1500	59	5	54	172	126	**46**	_	_	_
1700	77	16	**61**	_	_	_	_	_	_

Figure 4.16 shows that the M_s was linearly increased with stress and CC slopes increased from 11.1 to 16.3 MPa/ ºC as aging temperature was elevated from 450 to 650 °C. It should also be noted that A_f is both aging temperature and stress dependent. The A_f increases almost linearly for all aged conditions while it increases more rapidly with stress for the low strength 650 °C-3h aged samples due to plastic deformation. The superelasticity can only be observed above A_f and the σ_{SIM} depends on the difference between A_f and M_s and CC slope. The poor superelastic behavior of the 650 °C-3h aged sample could be attributed to the high CC slope, large difference between M_s and A_f and the low strength of matrix due to the formation of large particles. However, formation of fine precipitates and relatively low CC slope and A_f–M_s after 450 °C-3h and 550 °C-3h aging resulted in perfect superelasticity at low (–20 to 40 °C) and high (120 to 160 °C) temperatures, respectively.

4.5 $Ni_{51.2}Ti_{28.8}Hf_{20}$ conclusions

Important finding of the effects of thermal treatments on the microstructure and shape memory properties of Ni-rich $Ni_{51.2}Ti_{28.8}Hf_{20}$ can be summarized as follows:

1. They have the ability to show shape memory behavior under ultra-high stress levels at room and high temperatures. The high strength of the alloy is due to presence of fine precipitates with small interparticle distance after three hours aging at 450 and 550 °C which make them unique candidates for various applications in medical, aerospace, automotive and energy industries.
2. Thermal treatments can be used to tailor the precipitation characteristics and shape memory properties. Homogeneous distribution of fine H-phase precipitates (< 15 nm) with small interparticle distance was observed after aging at 450 °C-3h which

improved the strength of the matrix and suppress the martensitic transformation. These nanosize precipitates were absorbed by martensite plates during propagation. However, size of precipitates increased to ~40-70 nm and propagation of martensite variants was limited in the space between the precipitates. Also, $(011)_{B19'}$ Type I twining mode was observed at the intervariant boundaries.

3. Near perfect dimensional stability with negligible irrecoverable strain and low thermal hysteresis (< 30 °C) was demonstrated during thermal cycling at high compressive stress level of 1700 MPa after aging at 450 °C-3h. Further three hours aging at 550 °C result in almost full recoverable strain under 1500 MPa with thermal hysteresis in range of 30–40 °C. The M_s increased above 100 °C while poor dimensional stability with noticeable irrecoverable strain and high thermal hysteresis was observed during thermal cycling after aging at 650 °C-3h
4. The CC slope increased from 11.1 to 16.3 MPa/ ºC when three hours aging temperature raised from 450 to 650 °C. Although, perfect superelastic behavior with 4% fully recoverable strain was experimented at temperature ranges of –40 to 40 °C and 120 to160 °C as material aged at 450 °C-3h and 550 °C-3h, respectively.
5. In all aged conditions, A_s was lower than M_s during thermal cycling experiment resulting in high stored elastic strain during forward transformation which simply helped the reverse transformation.

4.6 Results and discussion: $Ni_{52}Ti_{28}Hf_{20}$

4.6.1 Transformation Temperature and Microstructure

DSC response of solution treated $Ni_{52}Ti_{28}Hf_{20}$ samples were conducted after three hours aging at various temperatures ranging from 400 to 750 °C to clarify the effects of aging temperature on the TTs and strength of the material. The sample solutionized at 900 °C for three hours to achieve a single phase microstructure since it has been shown that the furnace cooled sample had very large precipitates (Figure 3.2f). Figure 4.17a shows the DSC responses of solutionized $Ni_{52}Ti_{28}Hf_{20}$ heat treated for three hours at different temperatures from 500 to 750 °C. DSC samples were cycled three times in order to reveal the thermal stability of transformation peaks. No martensitic transformation was observed for solutionized and aged samples up to 450 °C even when they were cooled down to -100 °C and their DSC results have not been shown in Figure 4.17a. It is clear that the TTs have a complex relationship with aging temperature and the transformation peaks are broad.

Figure 4.17b illustrates the Vickers hardness and transformation peak temperatures as a function of aging temperature. It is clear that solutionized and samples aged up to 450 °C for three hours are in austenite while aged samples above 500 °C are in martensite at room temperature. This could be a possible reason for high hardness value of solutionized and samples aged up to 450 °C which is in the range of 720-730. The hardness was below 700 for aging temperature above 450 °C where the material is in martensite. In addition, M_p and A_p reached to the maximum temperatures of 53 °C and 106 °C after 500 °C-3h aging, respectively. M_p was decreased to –10 °C for 550 °C-3h aged condition while it increased to 32 °C after 650 °C-3h aging. Further aging above 650 °C resulted a decreased in transformation peak temperatures.

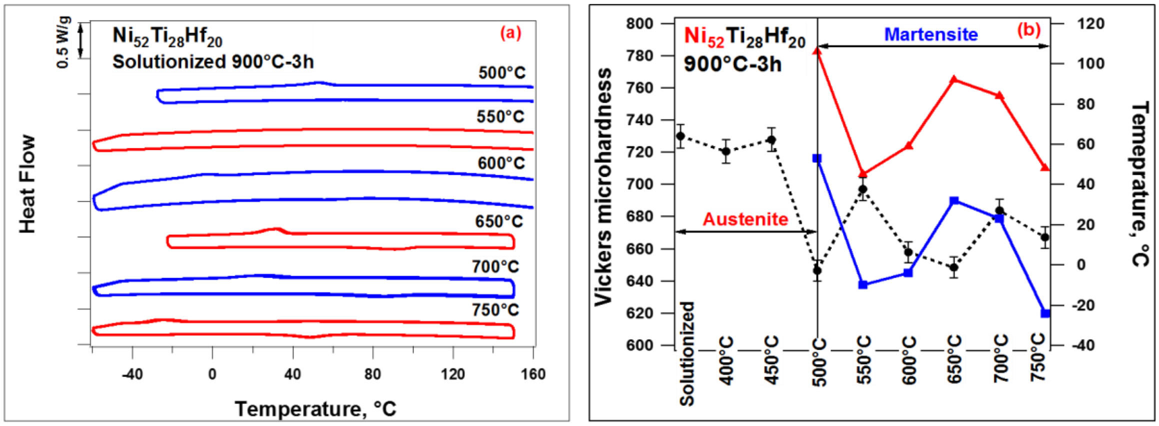

Figure 4.17: (a) DSC responses of $Ni_{52}Ti_{28}Hf_{20}$ after three hours aging at various temperature from 500 to 750 °C and (b) Vickers microhardness and transformation peak temperatures as a function of three hours aging.

TEM micrograph and corresponding SAD pattern obtained from solution treated $Ni_{52}Ti_{28}Hf_{20}$ are presented in Figure 4.18. It is clear that the large second phases are existed in the alloy even after solutionized at 900 °C. The diffraction pattern from matrix region confirmed the B2 austenite for solution treated sample at room temperature. Furthermore, the SAD pattern from the second phase along [100] zone axis was not evidence of an H-phase precipitate. EDS analysis revealed that the average composition of a second phase was 58.5 at. % Ni, 29.1 at. % Hf and 12.3 at. % Ti. It is possible that new precipitate phase of $Ni_{10}(Hf,Ti)_7$ type is presented in solution treated $Ni_{52}Ti_{28}Hf_{20}$. Thus, the complex behavior of TTs with aging temperatures (Figure 4.17b) could be attributed to presence of different phases in solution treated material and detail microstructural analysis is needed.

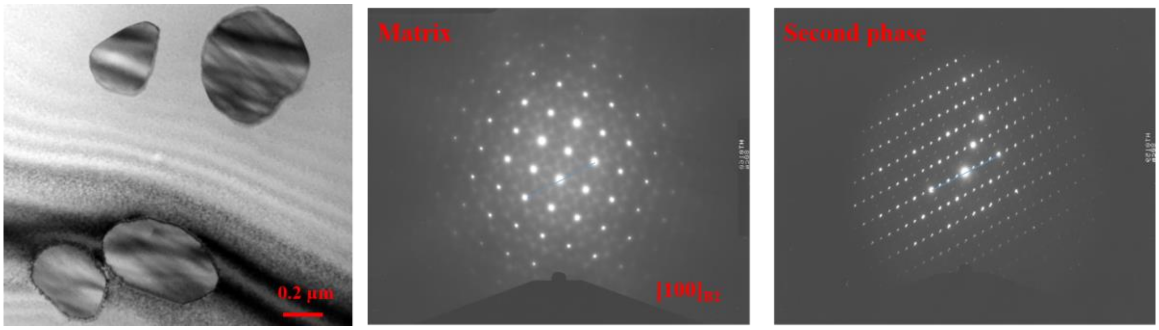

Figure 4.18: TEM micrograph and corresponding SAD pattern of matrix and second phase of solutionized $Ni_{52}Ti_{28}Hf_{20}$.

4.6.2 Shape Memory Effect and Superelasticity

Thermal cycling under stress responses of the $Ni_{52}Ti_{28}Hf_{20}$ SMAs in solutionized and aged conditions are shown in Figure 4.19. The specimens were strained at temperatures above A_f followed by thermal cycling between temperatures below M_f and above A_f under the selected compressive stress. It is clear that TTs and shape memory strains increase with the externally applied stress in the all tested $Ni_{52}Ti_{28}Hf_{20}$ samples as shown in Figure 4.19. No martensitic transformation was observed under 100 MPa for solution treated sample while the M_s was increase from 72 °C at 100 MPa to 142 °C at 1500 MPa as shown in Figure 4.19a. Full recovery of strain was illustrated up to 1000 MPa, however, irrecoverable strain of 0.27% was experimented at high stress level of 1500 MPa for solution treated condition. The total strain was less than 1% and temperature hysteresis increased from 13 °C at 500 MPa to 43 at 1500 MPa.

It is obvious from Figure 4.19b that shape memory effect was not clearly experimented at low stress levels up to 300 MPa after 450 °C-3h aging. As described before, this could be attributed to that the stress was not sufficient to select favorable martensite variants and also low TTs. The M_s was raised from –8 to 80 °C with increasing stress from 500 to 2000 MPa. The strength of material was improved after 450 °C-3h where almost perfect dimensional stability with recoverable strain of less than 1% was observed at ultra-high stress level of 2000 MPa. In addition, the thermal hysteresis was below 20 °C which made this material an excellent candidate for high strength actuator.

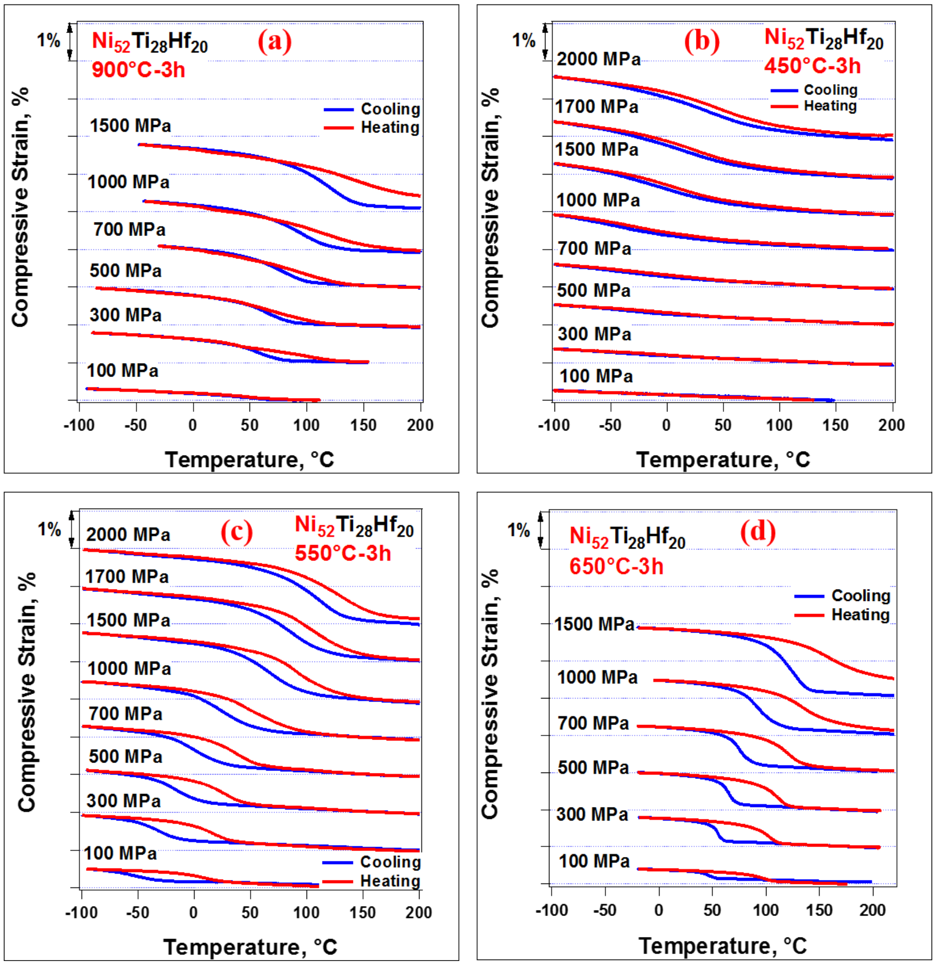

Figure 4.19: Shape memory effect under compressive stress for (a) solutionized, (b) 450 °C-3h, (c) 550 °C-3h and (d) 650 °C-3h aged $Ni_{52}Ti_{28}Hf_{20}$.

Shape memory behavior can even be observed at low compressive stress levels for 550 °C-3h aged sample as clearly shown in Figure 4.19c. The M_s was below room temperature for stresses below 700 MPa while it was greater than 100 °C as stress increased above 1500 MPa. Total strain was increased from 0.3% at 100 MPa to a maximum of 1.2%

at 2000 MPa. Perfect dimensional stability was observed up to 1700 MPa while irrecoverable strain of 0.17% was obtained as stress was increased to 2000 MPa. It is worth to mention that thermal hysteresis was decreased from 52 to 23 °C with increasing stress from 100 to 2000 MPa.

Figure 4.19d illustrates the thermal cycling under compressive stress of 650 °C-3h aged sample where TTs shifted to higher temperatures in contrast to other conditions. The M_s was 53 °C at 100 MPa and increased to 139 °C under 1500 MPa. It is clear the strength of the material diminished where large irrecoverable strain of 0.4% was obtained at 1500 MPa. Total strain was raised from 0.2 to 2.4% while thermal hysteresis was increased from 40 to 53 °C as stress increased from 100 to 1500 MPa.

Isothermal stress-strain responses of $Ni_{52}Ti_{28}Hf_{20}$ for solution treated and aged conditions are shown in Figure 4.20. It is clear that the deformation behavior of the alloy is dependent on test and aging temperatures. Solutionized sample was fully in martensite at –25 °C and the deformation resulted in reorientation of martensite variants. The remain strain after unloading at –25 °C and 80 °C was fully recovered by heating up the sample to 200 °C. Almost prefect superelastic behavior was observed after 3% deformation at 100 °C while further loading to 4% strain caused failure where the stress was reached to ~2100 MPa in solutionized condition.

Perfect superelastic with 4% recoverable strain behavior was experimented at temperature range between –60 to 0 °C after 450 °C-3h aging. The stress level for the onset of martensitic transformation was increased from 930 to 1250 MPa with temperature raising from –60 to 0 °C. The strength of solution treated material was improved after 450 °C-3h aging where maximum achievable stress for all selected temperatures was ~ 2200.

It is clear that the stress-strain slope in transformation region is high as ~495 MPa/1% while the dissipation of energy during loading/unloading cycle, i.e. mechanical hysteresis, is low which it is in a good correlation with thermal hysteresis for 450 °C-3h aged sample.

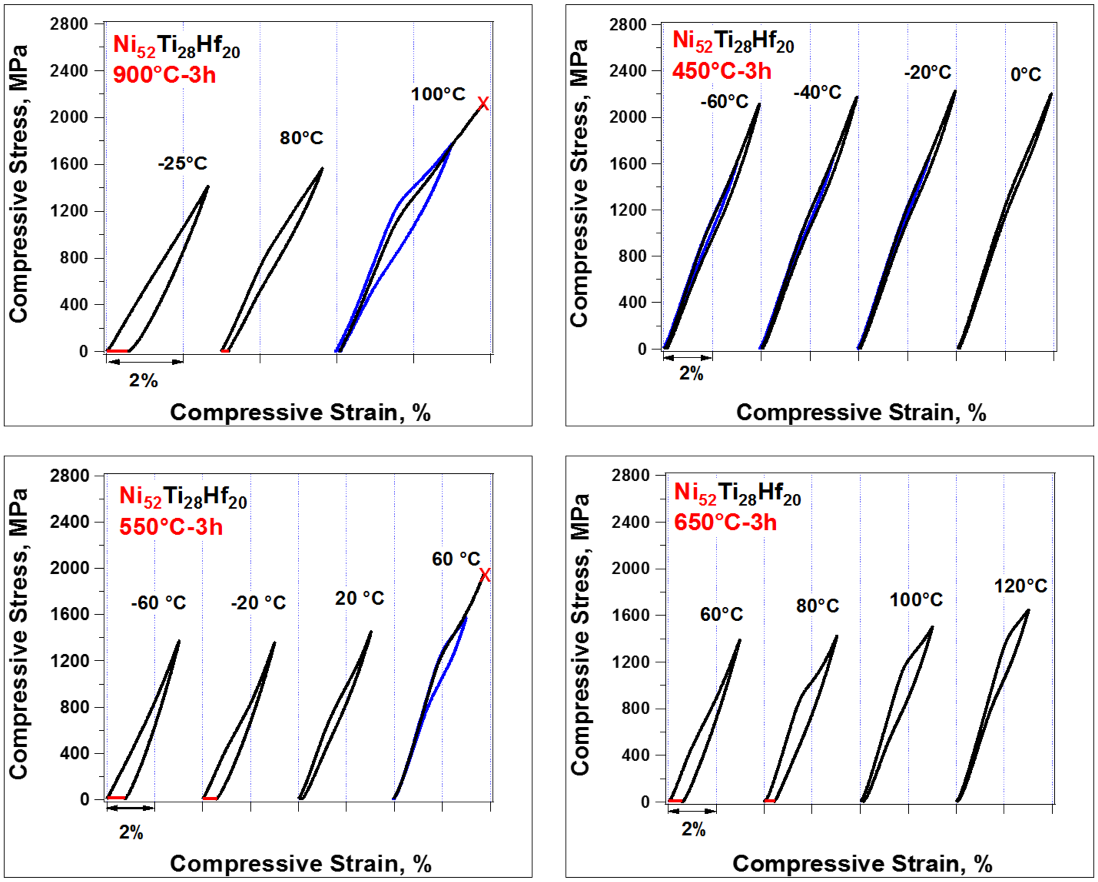

Figure 4.20: Stress vs. strain responses of $Ni_{52}Ti_{28}Hf_{20}$ for solutionized and aged conditions.

The 550 °C-3h aged $Ni_{52}Ti_{28}Hf_{20}$ was not fully above A_f at temperatures –60 °C and –20 °C and the remain strains upon unloading were fully recovered by heating up the sample to 200 °C. Almost full recovery was observed after 3% deformation at 20 °C where the required stress to induced martensitic transformation was ~700 MPa. Perfect superelastic with 3% recoverable strain was experimented at 60 °C while further deformation to 4% was resulted in failure of the sample where the stress level reached to ~2000 MPa.

Similar to 550 °C-3h, the material was not in austenite at temperature 60 °C and 80 °C and the remain strains were fully recovered by heating up the samples above A_f for 650 °C-3h aged condition. Near perfect superelasticity with small irrecoverable strain of 0.1% was observed at 100 °C where the σ_{SIM} was 1130 MPa. In addition, perfect superelastic with 3% recoverable strain and corresponding σ_{SIM} of 1370 MPa was experimented at high temperature of 120 °C after 650 °C-3h aging.

4.6.3 Shape Memory Properties

Recoverable and irrecoverable strains of solutionized and aged samples are extracted from the load-biased thermal cycling experiments (Figure 4.19) and are presented in Figure 4.21a. It is evident that the recoverable strains increase with applied compressive stress due to the fact that applied stress favors certain variants pairs along its loading direction. Consequently, with increasing applied stress, the amount of shearing in the lattice structures of the transforming phases also increases leading to more transformation strains. The increase in the transformation strains is followed by a tendency to saturate as in the aged materials. In the solutionized condition, recoverable strain was reached a maximum of 0.8% at 1200 MPa and then suddenly dropped as stress increased to 1500 MPa due to formation of plastic deformation in the material.

Maximum recoverable and irrecoverable strains decrease with three hours aging at 450 °C as shown in Figure 4.21a. The decrease can be derived from the increased volume fraction of the precipitates aging temperature. Since the precipitates cannot transform, the increase of the volume fraction yields less transformable material in the matrix and thus, smaller recoverable strains are observed with increasing volume of precipitates. Other possible reason could be attributed to the difficulty of nucleation of martensite where no shape memory behavior was observed at stress levels below 500 MPa (Figure 4.19b) since the stress was not sufficient to select favorable martensite variants. It could be predicted that fine precipitates with small interparticle distance formed after 450 °C-3h aging that created strong local stress fields, thus, more energy need to be provided to overcome the internal stress fields and nucleate martensite plates. In addition, the low irrecoverable strain links to high strength of the material due to precipitation strengthening.

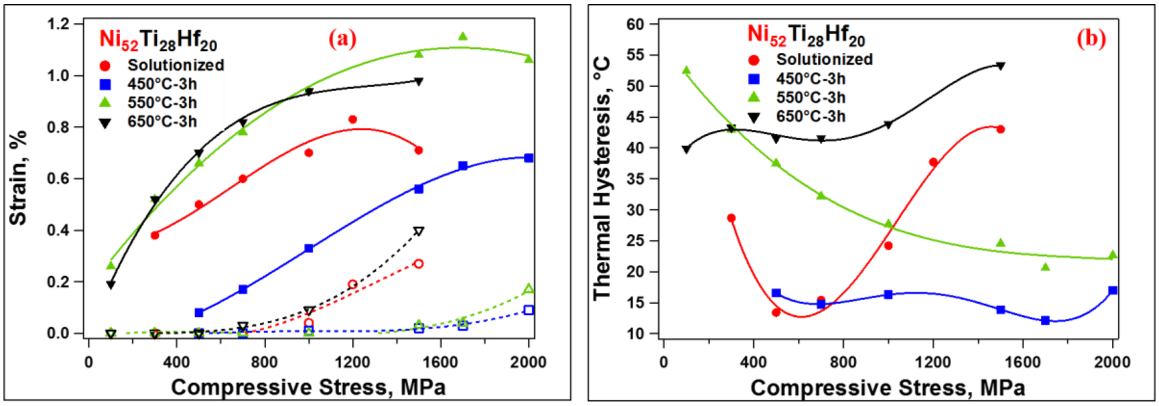

Figure 4.21: (a) Recoverable (solid lines) and irrecoverable (dashed lines) strains and (b) thermal hysteresis of $Ni_{52}Ti_{28}Hf_{20}$ as a function of compressive stress.

The specimen aged at 550 °C and 650 °C for three hours show slightly higher transformation strains as compared to the solutionized and 450 °C-3h aged conditions. This case is also similar to what was observed in high strength $Ni_{45.3}Ti_{29.7}Hf_{20}Pd_5$ (at. %) polycrystalline SMAs [112] and $Ni_{50.3}Ti_{29.3}Hf_{20}$ (at. %) HTSMAs [114]. A slight change in the lattice parameters of the transforming phases or internal stress fields around the precipitates could be responsible for the change (e.g. increase) in the transformation strain [34]. It has been reported in 550 °C-3h aged $Ni_{50.3}Ti_{29.3}Hf_{20}$ that the small precipitates (less than 20nm in size) could absorbed by martensite plates during transformation which resulted in an increase in transformation strain.

The thermal hysteresis was measured graphically as a temperature difference at the midpoint of heating and cooling curves (Figure 4.19) and is shown in Figure 4.21b. The thermal hysteresis was found to be decreased with stress up to 700 MPa and then increased at high stress levels for solutionized $Ni_{52}Ti_{28}Hf_{20}$. The decrease in thermal hysteresis with stress can be attributed to that the more favorable variants were selected at higher stress level and the dissipation energy due to interaction between martensite variants was decreased and the alloys has high strength to suppress plastic deformation. Therefore, the thermal hysteresis were decreased from 52 °C at 100 MPa to 23 °C at 2000 MPa for the 550 °C-3h aged condition. The thermal hysteresis was below 20 °C for 450 °C-3h aged sample where the material exhibited high strength and low irrecoverable strain. The increase in the temperature hysteresis in the 650 °C-3h aged material can be ascribed to defect generation upon applied stress due to low strength of alloys (as evidenced from the irrecoverable strain increase with stress as shown in Figure 4.21a). It is a well-known fact that defect generation dissipates energy and increase hysteresis in shape memory alloys [37, 147].

Figure 4.22 shows the dependence of M_s as a function of applied stress from the shape memory curves in Figure 4.19. As expected, M_s increases linearly with stress following the CC relationship which was expressed in equation 1.3. It is clear that the M_s are lower for aged conditions in contrast with solutionized sample which indicates that there were second phases existed in the matrix after solution treated at 900 °C-3h as shown in Figure 4.18. Furthermore, M_s was raised with increasing aging temperature which can be attributed to increase volume fraction of precipitates with aging temperature and more depletion of Ni content from matrix, thus the TTs were shifted to higher temperatures. It was found that CC slopes were 17.4 MPa/ °C, 16.4 MPa/ °C, 11.3 MPa/ °C and 15.5 MPa/ °C for solutionized, 450 °C-3h, 550 °C-3h and 650 °C-3h aged condition, respectively.

The lack of superelasticity in solution treated can be due to high CC slope and low strength of the matrix. However, the CC slope only decreased by 1 MPa/ °C after 450 °C-3h aging but perfect superelasticity was observed at low temperature window of –60 to 0°C. First reason can be related to lower TTs in 450 °C-3h sample as compared to solutionized case. Lower TTs allow the superelasticity test conduct at lower temperatures where the material has higher strength since the critical stress for slip decreased with temperature. In addition, the extreme high strength of the aged sample allows the material to show excellent dimensional stability at high stress levels (Figure 4.19b) and perfect superelastic behavior (4.20) after 450 °C-3h aging.

In contrast to 450 °C-3h aged condition, it is clear for Figure 4.22 that the 550 °C-3h aged sample had a highest recoverable strain and lowest CC slope while the superelastic window was very narrow. This could attributed to that the strength of the material was diminished while the TTs where increased to higher temperature after 550 °C-3h aging. Thus, stress induced martensitic transformation and plastic deformation simultaneously were occurred in the matrix which linked to failure of material while it was loading to 4% deformation at 60 °C (Figure 4.20). In addition, lack of precipitation strengthening, high CC slop and TTs could be the reasons for poor shape memory properties of 650 °C-3h aged sample.

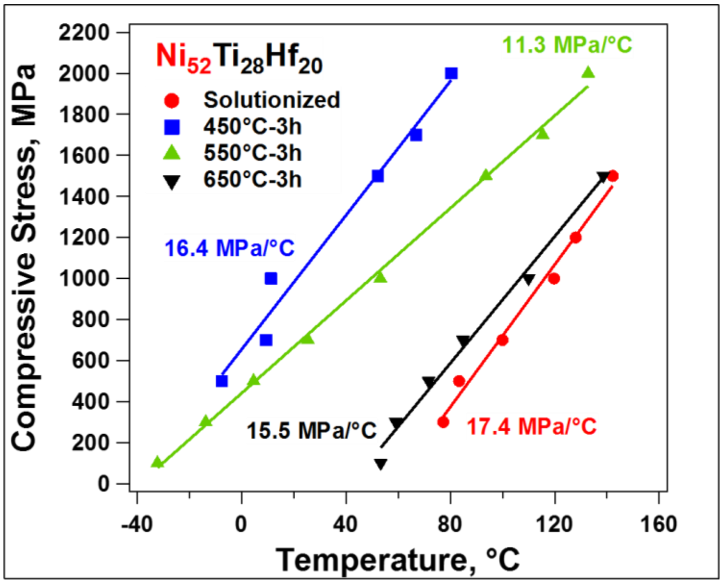

Figure 4.22: Applied stress vs. M_s for solutionized and aged $Ni_{52}Ti_{28}Hf_{20}$ alloys.

4.7 Conclusions: $Ni_{52}Ti_{28}Hf_{20}$

Effects of aging on the shape memory properties of $Ni_{52}Ti_{28}Hf_{20}$ polycrystalline SMAs were documented by means of various experimental techniques such as DSC, thermal cycling under stress and superelastic tests at constant temperatures. The findings can be summarized as following:

1. The TEM micrograph show the existence of second phases in the solution treated sample. In contrast to solution treated case, the TTs shifted to lower temperature after three hours aging, while, TTs increase with aging temperature.

2. Almost perfect dimensional stability with negligible irrecoverable strain observe at ultra-high stress level of 2 GPa for 450 °C-3h aged sample. Also, full recovery of 4% strain illustrates at low temperature range (–60 to 0 °C) with maximum achievable stress level of 2.2 GPa and CC slope of 16.4 MPa/ °C after 450 °C-3h

aging. The material shows low mechanical and thermal hysteresis due to high strength and storage elastic energy during martensitic transformation.

3. Aging at 550 °C-3h results in near perfect dimensional stability with recoverable strain of less than 1.2% at stress levels as high as 2 GPa. The superelastic window is narrow since the strength of the alloy reduces while the TTs increase after 550 °C-3h aging which result
4. The strength of material diminishes where large irrecoverable strain of 0.4% experiments under 1500 MPa after 650 °C-3h aging. Poor shape memory properties of 650 °C-3h sample is due to lack of precipitation strengthening.

5 Effect of Stress States

5.1 Introduction

It is known that the martensitic transformation in SMAs can be induced not only by thermal cycling, but also by applied stress. The deformation modes of SMAs highly depend on the structure of transforming phases, martensite morphology, precipitation characteristics and crystallographic orientation [5]. Furthermore, it was also illustrated that the deformation behavior of SMAs can be altered by the stress states [79, 148-151]. The tension-compression asymmetry of SMAs is well established experimentally which can be attributed to the difference in deformation mechanisms (e.g twinning types, detwinning) with applied stress direction and unidirectional nature of twin deformation [78, 79, 149].

The stress-strain curves of NiTi demonstrated considerable asymmetry with stress state [71, 78, 79, 148, 149]. It has been concluded that the polycrystalline NiTi demonstrates smaller recoverable strain, higher critical stress to induce martensitic transformation (σ_{SIM}) and steeper transformation stress-strain slopes in compression than in tension [71, 148, 152, 153]. For instance, the σ_{SIM} was ~200 MPa under compression while it was greater than 300 MPa under tension for $Ni_{50.8}Ti_{49.2}$ after 400 °C-1.5h aging [79]. In textured $Ni_{50.8}Ti_{49.2}$ after 500 °C-15h aging [69], it was revealed that the recoverable strain was two times higher in tension than in compression. The critical stress for transformation is found to be higher in tension as compared to torsion during the deformation of equiatomic NiTi [57].

Recently, NiTiHf SMAs are becoming a promising candidate to use in variety of applications mainly in aerospace, automotive and energy industries where they will be subjected to bending and/or multiaxial loads. Thus, it is important to study the shape memory behavior of NiTiHf under different stress states. In this chapter, shape memory properties and superelastic behavior of $Ni_{50.3}Ti_{29.7}Hf_{20}$ were investigated in tension. $Ni_{50.3}Ti_{29.7}Hf_{20}$ was induction melted and then casted into a 1 inch diameter copper chill mold. The ingot was homogenized at 1050 °C for 72h in vacuum, then extruded at 900 °C with 7:1 reduction followed by air cooling. This condition referred to "as-extruded" throughout the chapter. The alloys were aged at selected temperatures for three hours to study the effects of precipitation on their tensile behavior and the results were compared to the previous shape memory characteristics reported under compression.

5.2 Experimental Results

DSC responses of $Ni_{50.3}Ti_{29.7}Hf_{20}$ alloys that are heat treated at selected temperatures from 300 to 800 °C for three hours are shown in Figure 5.1a. Each sample was thermally cycled for three times to reveal the stability of the transformation peaks. Figure 5.1b illustrates the transformation peak temperatures (M_p and A_p) and thermal hysteresis of aged samples. The M_p was about or below 100 °C after aging at low temperatures region (< 500 °C). After the initial dropped at 400 °C, TTs increased with aging temperature and M_p reached the maximum temperature of 189 °C after 700 °C-3h aging. Lastly, TTs started to decrease as aging temperature was elevated above 700 °C. Thermal hysteresis decreased from 38 to 30 °C with aging temperature raised from 300 to 500 °C and reached to the maximum value of 48 °C for 700 °C-3h aged sample. It is clear from Figure 5.1 that the TTs were increased and stability of transformation peaks were improved after three hours aging at 500 and 550 °C. Thus, these two aged conditions are selected to capture the influences of aging on shape memory properties of $Ni_{50.3}Ti_{29.7}Hf_{20}$ under tensile stress.

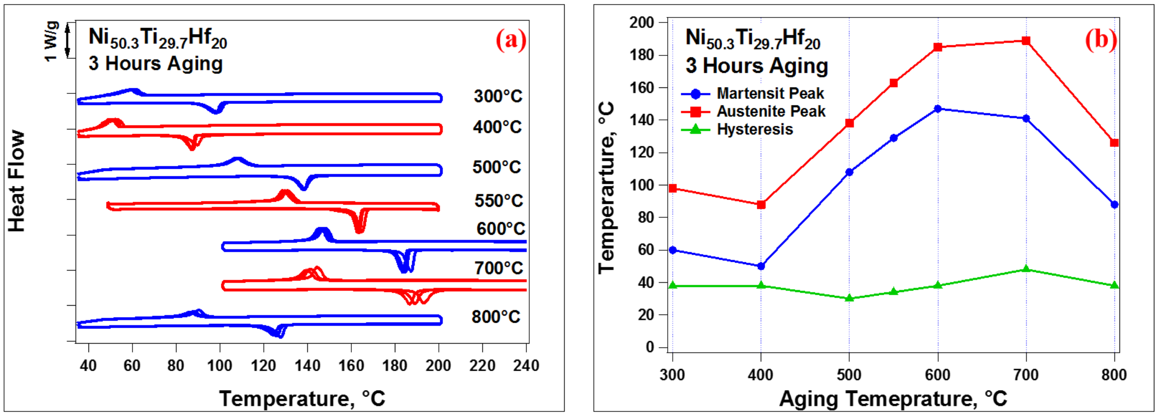

Figure 5.1: (a) DSC responses and (b) transformation peak temperatures (M_p and A_p) and thermal hysteresis of $Ni_{50.3}Ti_{29.7}Hf_{20}$ as a function of aging temperature.

Figure 5.2 represents the thermal cycling behavior of $Ni_{50.3}Ti_{29.7}Hf_{20}$ in tension for the as-extruded, 500 °C-3h and 550 °C-3h aged conditions. The thermal cycling under compressive stress [114, 128] was added to Figure 5.2 for comparison. It is clear that TTs were increased with stress and aging temperatures for both tension and compression conditions.

Figure 5.2a shows the thermal cyclic behavior of as-extruded alloy. The M_s was increased from 75 to 165 °C as applied tensile stress was elevated from 100 to 600 MPa. Total tensile strain was 1.9 % at 100 MPa and increased to 4.9 % at 500 MPa. Near perfect shape memory effect with small irrecoverable strain of 0.2 % was observed at 500 MPa. However, total tensile strain of 5.5% with corresponding irrecoverable strain of 0.7% was detected during thermal cycling under 600 MPa. Furthermore, thermal hysteresis was increased with tensile stress and raised from 33 °C under 100 MPa to 63 °C under 500 MPa.

Shape memory behavior of $Ni_{50.3}Ti_{29.7}Hf_{20}$ after 500 °C-3h aging is shown in Figure 5.2b. The strength of the material was improved after aging at 500 °C-3h where near prefect dimensional stability with negligible irrecoverable strain was demonstrated under tensile stress of 500 MPa and only small residual strain of 0.1% was obtained at 700 MPa. Also, M_s was shifted to the temperatures above 100 °C and make these alloys a good candidate for high temperature applications. Total tensile strains of 1.4%, 3.5% and 4% were achieved during thermal cycling under 100 MPa, 500 MPa and 700 MPa, respectively. The thermal hysteresis was lower than 25 °C for the tensile stress levels between 100 to 600 MPa.

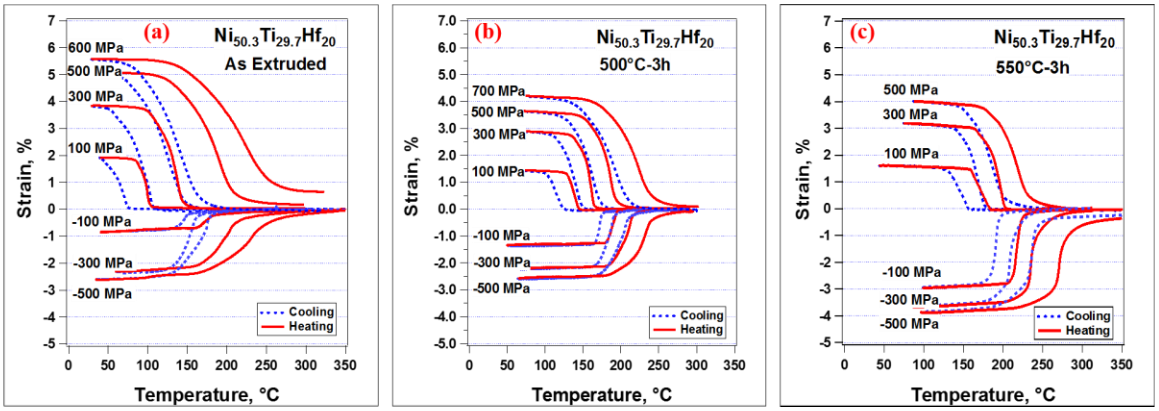

Figure 5.2: Thermal Cycling behavior of (a) as-extruded, (b) 500 °C-3h aged, and (c) 550 °C-3h aged $Ni_{50.3}Ti_{29.7}Hf_{20}$ alloys under applied tensile and compressive stress.

Figure 5.2c illustrates the shape memory behavior of 550 °C-3h aged $Ni_{50.3}Ti_{29.7}Hf_{20}$ alloy. The TTs were reached to their highest value amongst all other conditions where M_s was 157 °C at 100 MPa and raised to 200 °C at 500 MPa. Furthermore, perfect dimensional stability with maximum recoverable strain of 3.6% was exhibited at 500 MPa. Thermal hysteresis was about 25–30 °C for the stress levels up to 500 MPa.

Isothermal tensile stress-strain responses of as-extruded, 500 °C-3h and 550 °C-3h aged $Ni_{50.3}Ti_{29.7}Hf_{20}$ at selected temperatures above A_f are illustrated in Figure 5.3. Full recovery was not exhibited in as-extruded condition after 5% deformation unloading, however, the residual strains were fully recovered upon heating the sample to 300 °C. It is noticeable that the σ_{SIM} was increased with test temperature for all cases. In as-extruded condition, the σ_{SIM} was increased from 500 MPa at 160 °C to 680 MPa at 200 °C and it decreased after each stress cycle. This could be attributed to the fact that retained martensite and plastic deformation assisted the formation stress induced martensite transformation in the next stress cycle.

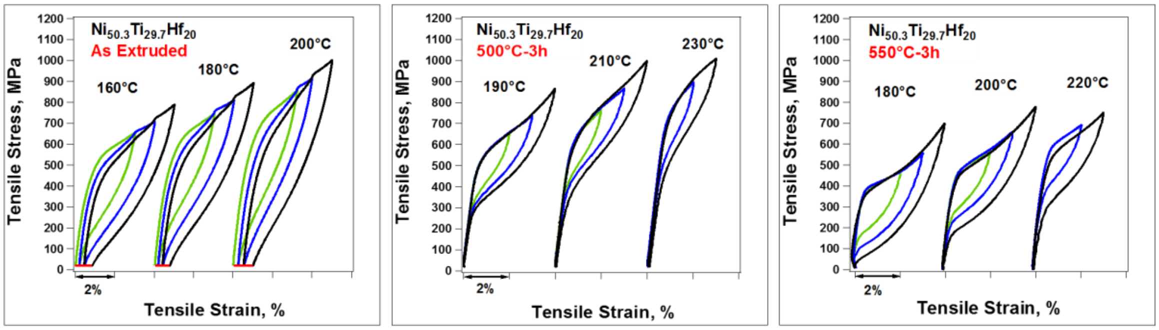

Figure 5.3: Stress-Strain relationship of as-extruded, 500 °C-3h, and 550 °C-3h of $Ni_{50.3}Ti_{29.7}Hf_{20}$ alloy.

Perfect superelasticity with 4% tensile recoverable strain at high temperatures of 190–210 °C was observed in the 500 °C-3h aged alloy. The σ_{SIM} was increased from 530 MPa at 190 °C to 730 MPa at 230 °C and the alloy reached to 1000 MPa after 4% deformation. Negligible irrecoverable strain of 0.05% was experimented after 3% deformation at 230 °C. Aging at 550 °C-3h resulted in perfect superelastic behavior between temperatures 180 °C and 220 °C. Also, the σ_{SIM} was 400 MPa at 180 °C and was increased to 640 MPa when the test temperature raised to 220 °C for 550 °C-3h aged condition.

The stress-strain curves are more stable and the dissipation of energy is lower after aging in contrast to the as-extruded condition. The mechanical hysteresis was determined as the stress difference between loading/unloading curves in transformation regions at the middle of stress-strain curves. The mechanical hysteresis was strain dependent and increased from ~280 MPa after 3% deformation to ~380 MPa after 5% strain at 180 °C for the as-extruded condition. The mechanical hysteresis is in the range of 160-220 MPa and 200-280 MPa for 500 °C-3h and 550 °C-3h aged conditions, respectively. It is worth to mention that the dissipation energy during thermal and stress induce transformation are in a good correlation with each other where the as-extruded samples demonstrated high thermal and mechanical hysteresis, whereas, low temperatures and stress hysteresis were observed after 500 °C-3h aging.

5.3 Discussion

Figure 5.4a represents the recoverable and irrecoverable strains of $Ni_{50.3}Ti_{29.7}Hf_{20}$ alloys observed in tension from the current results and compression from literature [114, 128] that extracted from thermal cycling under stress. It is clear that recoverable strain increases initially with applied stress which is attributed to the increase in the volume fraction of favorable martensite variants with stress. Then, recoverable strain saturates and decreases with further increase in stress due to plastic deformation. For instance, the recoverable strain of as-extruded sample increased from 1.9% under 100 MPa to maximum of 4.7% under 500 MPa and it saturated while 0.2% irrecoverable strain was observed at 500 MPa and it increases to 0.7% as tensile stress elevated to 600 MPa.

It is noticeable from Figure 5.4a that the recoverable strain at low tensile stress level of 100 MPa is low for all conditions due to the fact that the stress was not sufficient to select favorable martensite variants and mostly self-accommodated martensite plates formed during martensitic transformation. Tensile strains after three hours aging at 500 °C and 550 °C were almost identical for both aging conditions but lower than the strains of as-extruded sample. Formation of non-transformable particles after aging decreased the volume fraction of transforming regions in the matrix and hence the tensile strain. The recoverable strains in tension are higher than the ones in compression which can be attributed the change in martensite morphology and activation of different martensite corresponding variant pairs in tension.

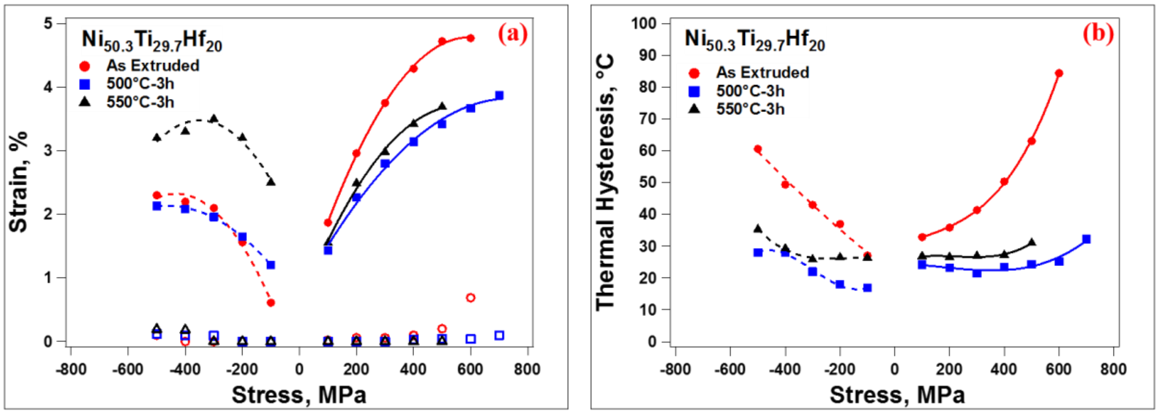

Figure 5.4: (a) recoverable (solid markers) and irrecoverable (hollow markers) strains and (b) thermal hysteresis of $Ni_{50.3}Ti_{29.7}Hf_{20}$ as function of tensile (solid lines) and compressive (dashed lines) stresses.

Thermal hysteresis of $Ni_{50.3}Ti_{29.7}Hf_{20}$ alloys under tension are illustrated in Figure 5.4b where the thermal hysteresis under compression [114, 128] are also added for comparison. Temperature hysteresis highly depends on the dissipation energy through friction, defects generation during transformation, interaction between the interphases, lattice compatibility between phases and strength of the material. It is clear from Figure

5.4b that thermal hysteresis decreases after aging in both tension and compression due to precipitation strengthening. Thermal hysteresis increases rapidly with applied stress in as-extruded condition due to lower strength of the alloy where applied stress is sufficient to generate defects during the phase transformation. It is noticeable that the thermal hysteresis is almost identical in tension and compression which means that the dissipation energy is stress state independent in $Ni_{50.3}Ti_{29.7}Hf_{20}$ alloys.

The tension-compression asymmetry in NiTiHf can be attributed to the unidirectional nature of shear strain across the martensite habit planes and martensite ordering. It is known that during martensitic transformation, only one specific martensite variant group is selected that provides the largest possible strain along the loading direction. The martensite corresponding variant pair (CVPs) with the largest RSSF are activated and then oriented along the shear direction with transformation. If the same material loaded in the opposite direction, it is possible that the RSSF of those CVPs are not the largest ones along the transformation direction, hence, they are not energetically favored where other CVPs can be activated. Another possible reason for the different transformation strains in tension and compression can be the change in the mobility of martensite variant interfaces.

It has been reported that the martensite variants boundaries are twin related and can be moved easily as transformation proceeds under tension in NiTi [149, 150]. However, the junction between the twin related martensite variants is not mobile under compression, resulting in generation of lattice defect during transformation and difficulty in phase transformation and detwinning. Microstructural investigations on the deformed equiatomic NiTi alloys confirmed that the deformation mechanism is different in tension and compression [149, 150]. After tensile deformation, <011> type II twinning is more frequently observed and two neighboring martensite variants become (001) twin related to each other. This (001) twin boundary is highly mobile under tension and as a result, two self-accommodated variants change into one variant favorable to applied stress by movement of boundaries between variants. In addition, no significant plastic deformation is observed inside the twin bands while dislocations are illustrated along the variants interfaces. On the other hand, high density of dislocations inside twin bands and variants accommodated area is observed after compressive deformation. Boundaries between two martensite plates containing <011> type II twins are not twin related to each other, resulting in no interfacial movement in compression. Thus, deformation proceeds by continuously increased compressive load and results in high stress-strain slope in the transformation region where plateau type deformation was observed under tensile.

Figure 5.5a shows the relationship between M_s and applied tensile and compressive [114, 128] stresses in $Ni_{50.3}Ti_{29.7}Hf_{20}$ alloys which are extracted from the thermal cycling under stress experiments. The M_s linearly increases with stress, following the CC relation where the slope of the lines are proportionally related to enthalpy of transformation and inversely correlated to transformation strain and equilibrium temperature. The difference in M_s values under no applied stress in tension and compression results could be attributed to the slight composition variation of the alloys during the fabrication process and rate of cooling after extrusion.

The CC slopes were 5.4 MPa/ °C in tension and 12.5 MPa/ °C in compression for the as-extruded sample. After 550 °C-3h aging, M_s was shifted to the higher temperature and the CC slope in compression was decreased to 7.5 MPa/ °C while it was increased to

8.5 MPa/ °C in tension. The change in CC slope could simply be explained by the asymmetry of transformation strain for tension and compression. The as-extruded material have maximum tensile strain of 5.5% while the maximum compressive strain was 2.4%, resulting in higher CC slope in compression as compared to tension. In contrast to as-extruded samples, the maximum transformation strain decreased under tensile loading while it increased under compression stress after three hours aging at 550 °C. Consequently, the CC slope of aged samples increased in tension and decreased in compression.

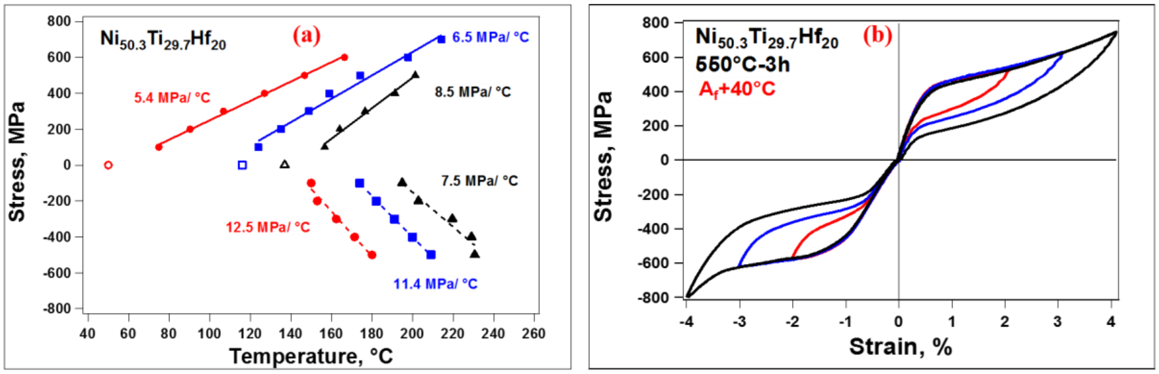

Figure 5.5: (a) M_s as function of tensile and compressive stresses and (b) stress-strain curve of 550 °C-3h aged $Ni_{50.3}Ti_{29.7}Hf_{20}$ after 4% deformation.

It is clear that after aging at 550 °C-3h the transformation strain and CC slopes under compression and tension are very identical. It should be noted that the recoverable strains and thermal hysteresis are also very similar in tension and compression after 550 °C-3h aging. Thus, the asymmetric behavior depends on the precipitation characteristics and after 550 °C-3h aging, $Ni_{50.3}Ti_{29.7}Hf_{20}$ act as an isotropic material where shape memory properties weakly depend on the direction of applied stress. This fact can be attributed to precipitation characteristics where strong stress fields around the precipitates can alter the selection of martensite variants and martensite morphology could change with precipitation size and interparticle distance.

It is worth to mention that perfect superelastic behavior with 4% recoverable strain is demonstrated at high temperatures under tension and compression [114] after three hours aging at 550 °C as shown in Figure 5.5b. The phase transformation can be considered completed in compression while it was not fully accomplished in tension due to higher transformation strain in tension. Similar to the NiTi [79], the tensile stress-strain curve demonstrated non-linearity upon unloading while the compressive curves were nearly perfectly elastic. It has been explained that strong local stress fields exist in the matrix due to the lattice mismatch between precipitates and martensite phase which try to inhibit the detwinning process. However, detwinning progress in opposition to the internal stress fields and developed strong back stress on the internal twin interfaces. The internal twins still exist upon unloading since the detwinning process is not completed and the strong back stresses help the reverse martensite detwinning process. In summary, the non-linearity behavior is attributed to the reverse movement of internal twins that strong back stress had formed on their interfaces during detwinning process. Detailed microstructural analysis is needed to explain the deformation mechanisms in NiTiHf under tension and compression.

5.4 Conclusion

It has been shown that the shape memory properties of $Ni_{50.3}Ti_{29.7}Hf_{20}$ alloys can be tailored by aging. Transformation peak temperatures were stable after 500 °C-3h aging and M_s reached the maximum value of 150 °C after 600 °C-3 aging. The polycrystalline $Ni_{50.3}Ti_{29.7}Hf_{20}$ alloys demonstrated superior shape memory effect and superelasticity in tension. The high recoverable strain of ~5% was achieved by thermal cycling under 600

MPa of the as-extruded alloy. Near perfect dimensional stability with negligible irrecoverable strain and recoverable strain of 4% was experimented under 700 MPa after 500 °C-3h aging. Further aging at 550 °C-3h resulted in a perfect dimensional stability with recoverable strain of 3.7% under 500 MPa. In addition, the CC slopes were in the order of 5-9 MPa/ °C under tensile stress and perfect superelastic with 4% recoverable strain was demonstrated at high temperature window of 180–230 °C for 500 °C-3h and 550 °C-3h aged conditions.

Experimental recoverable strains were found to be higher in tension than compression. The asymmetry in recoverable strain under tension and compression can be attributed to ordering of martensitic transformation, the unidirectional nature of habit plane and activation of different number of CVPs. In addition, the NiTiHf is anisotropic material and the shape memory properties of this HTSMAs is highly depend on the direction of applied stress and orientation of stress axis. However, after aging at 550 °C, the tension compression asymmetry is weak where the transformation strain and hysteresis are almost identical under tension and compression which can be attributed to the effects of precipitates.

6 Orientation Dependence of NiTiHf

6.1 Introduction

The shape memory (e.g. transformation strain, hysteresis, CC slope) and mechanical (critical stress for slip, ductility) properties of Ni-rich NiTi alloys are highly orientation and thermal treatment dependent [19, 37, 70, 154, 155]. Recent compression studies on as-grown $Ni_{50.3}Ti_{29.7}Hf_{20}$ single crystals showed a small transformation strain of 1% for [001] crystals, which did not change significantly with applied compressive stress up to ~1500 MPa [156]. In contrast, transformation strain was a function of stress approaching 3% and 4% at 700 MPa along the [111] and [011] orientations, respectively [156, 157]. In addition, [111]-oriented $Ni_{50.3}Ti_{29.7}Hf_{20}$ single crystals exhibited reasonable superelastic behavior but with a small residual strain in the temperature range of 180-200 °C [157]. However, it should be noted that these previous studies on single crystals [156, 157] were conducted in the as-grown condition with H-phase precipitates were already present in the microstructure due to the thermal conditions encountered during directional solidification. Therefore, no attempt was made to optimize the size or volume fraction of precipitate phase. Moreover, the orientation dependence of superelasticity was not previously investigated.

In this chapter, the shape memory and superelastic responses of solutionized (900 °C-3h) and solutionized plus aged (550 °C-3h and 650 °C-3h) Ni-rich $Ni_{50.3}Ti_{29.7}Hf_{20}$ single crystals were characterized along the three selected crystallographic orientations of [001], [011], and [111]. The effects of stress, temperature and precipitate characteristics on TTs, transformation strain and hysteresis were investigated in compression. The aging conditions were selected by considering the findings of previous studies on $Ni_{50.3}Ti_{29.7}Hf_{20}$ polycrystalline [109, 114] where 550 °C-3h aging introduced nano-size (≈ 20 nm) coherent precipitates in the matrix, which substantially improved the shape memory and mechanical properties of the alloy while aging at 650 °C for 3h produced an overaged condition, with the precipitates coarsened in size to 40–60 nm, but with transformation temperatures further increased [114].

6.2 Experimental Results

6.2.1 Martensite Transformation and Morphology

Figure 6.1 shows the DSC curves of the $Ni_{50.3}Ti_{29.7}Hf_{20}$ single crystals in the solutionized and aged conditions. The M_s of the solutionized sample is –25 °C and increases to 73 °C and 123 °C after three hours aging at 550 °C and 650 °C, respectively. The thermal hysteresis, defined as the difference between austenite and martensite peak temperatures, is 50–60 °C for all three conditions.

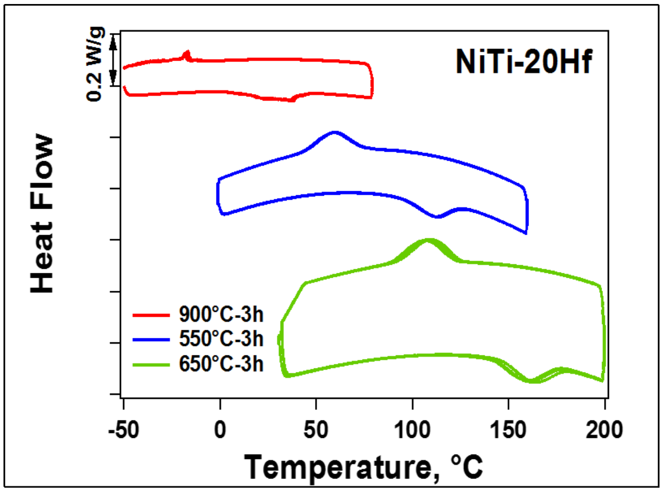

Figure 6.1: DSC Response of the $Ni_{50.3}Ti_{29.7}Hf_{20}$ alloy in the solutionized and aged conditions.

Figure 6.2 shows the TEM micrographs obtained at room temperature for the solutionized, 550 °C-3h and 650 °C-3h aged specimens. The solutionized specimen, shown in Figure 6.2a, has no precipitates and consists of a single B2 austenite phase, consistent with the DSC analysis shown in Figure 6.1. This is confirmed by the SAD diffraction pattern (inset to Figure 6.2a), which does not show evidence of any additional spots or streaking that could be due to a second phase.

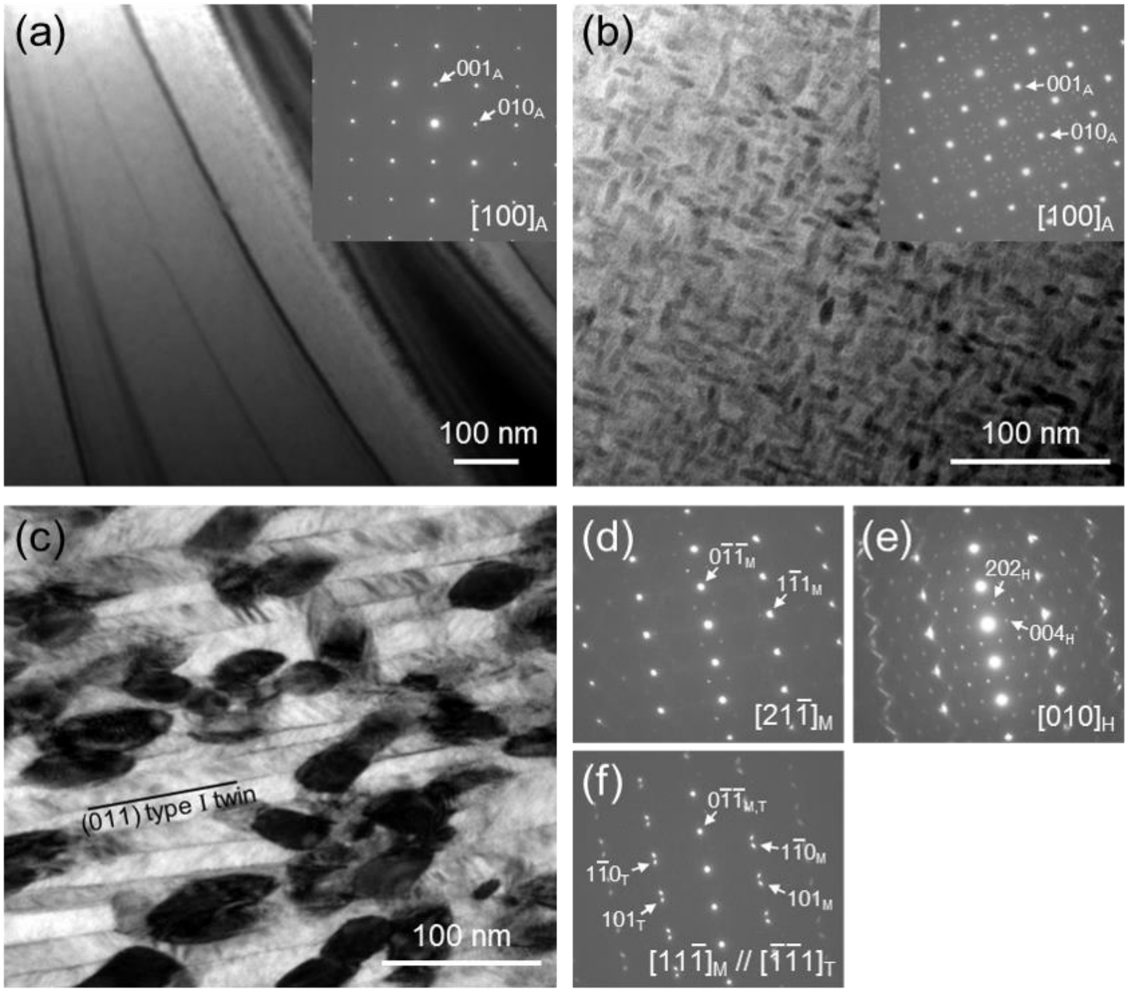

Figure 6.2: Bright field TEM micrographs and corresponding SAD patterns (insets) of the (a) solutionized specimen and (b) 550 °C-3h aged specimen. (c) Bright field image of the 650 °C-3h aged specimen and (d-f) SAD patterns obtained from (c). Subscripts A, H, M and T indicate B2 austenite, H-phase, B19′ martensite matrix, and twin, respectively.

Aging at 550 °C for three hours resulted in the formation of fine oblate spheroid-shaped precipitates with a major axis on the order ~15–20 nm as shown in Figure 6.2b. The crystal structure of the precipitates was determined by the SAD patterns as the H-phase which has been reported in Ni-rich NiTiHf alloys [110, 111].

Figure 6.2c shows the bright field image of the 650 °C-3h aged specimen. The precipitates maintain the same oblate-spheroid shape but have coarsened considerably with a long axis of 45–75 nm. Figures 6.2d and e represent the SAD patterns of the B19′ martensite taken along the $[21\bar{1}]_{B19'}$ zone axis and of the H-phase precipitate taken along the $[010]_H$ zone axis, respectively. Figure 6.2f shows the SAD pattern taken along the $[11\bar{1}]_{B19'}$ zone axis which reveals that the martensite plates in Figure 6.2c are twin-related with $\{011\}_{B19'}$ type I mode. It is noted that many streaks can be seen inside the martensite plates. The trace of the streaks was coincident with that of $(001)_{B19'}$ planes in martensite, implying that the martensite plates contain $(001)_{B19'}$ compound twins, which are considered the lattice invariant shear (LIS) of the martensitic transformation in NiTiHf alloys [106].

6.2.2 Thermal Cycling under Compressive Stress

During the thermal cycling experiments, the stress was isothermally applied above A_f when the material was in the austenite condition and then the sample was thermally cycled between a temperature below the M_f and back to a temperature above the A_f under constant stress. After the cycle was completed, the stress was incremented and the thermal cycling was repeated.

Figure 6.3 illustrates the strain-temperature responses of the solutionized NiTi-20Hf single crystals. The [001] and [111] orientations exhibited high dimensional stability, where only a small irrecoverable strain was observed under stress levels as high as 1000 MPa. Interestingly, the [011] orientation, did not exhibit shape memory behavior at lower stress levels (< 300 MPa) as apparently the stress is not sufficient to alter the self-accommodated structure and form more favorable martensite variants. The solutionized samples achieved recoverable strains of 3.1% and 3.7% at 700 MPa with corresponding irrecoverable strains of 0.5% and 0.1% along the [011] and [111] orientations, respectively. In contrast, the maximum recoverable strain along the [001] direction was only 1.1 % at 1500 MPa with a corresponding irrecoverable strain of 0.9% at this stress level.

It is clear from Figure 6.3 that the total strain (ε_{total}) and M_s increase with stress. For instance, the total strain for solutionized [111] orientation increased from 0.9 to 3.4% while M_s rises from –67 to 98 °C when the applied stress was increased from 100 MPa to 1000 MPa. Under stress, favorable martensite variants form and grow at the expense of self-accommodated variants resulting in a net shape change. The increasing external stress increases the volume fraction of favorable martensite variants over other variants and as a result, ε_{total} increases.

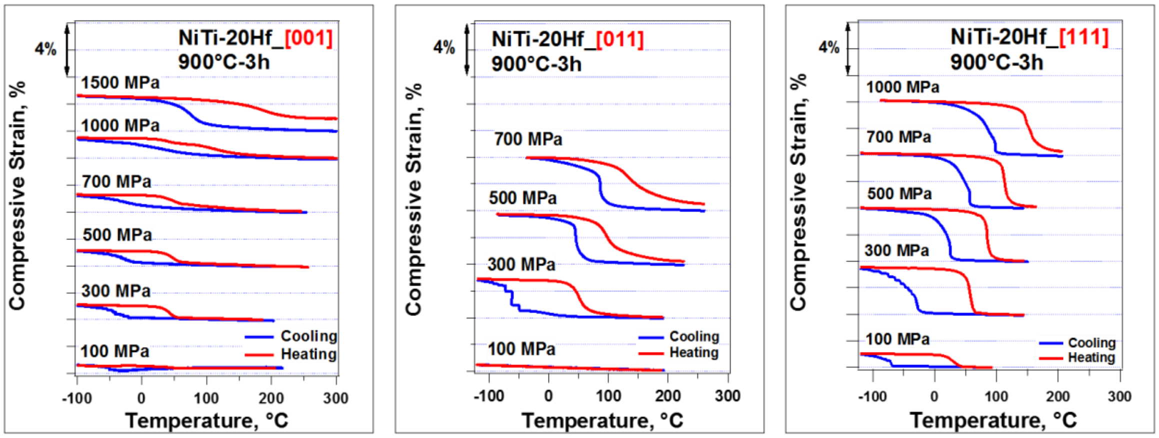

Figure 6.3: Strain vs. temperature responses for the solutionized $Ni_{50.3}Ti_{29.7}Hf_{20}$ single crystals along the [001], [011], and [111] orientations.

Figure 6.4 shows the thermal cycling responses of the 550 °C-3h aged single crystals. Compared to the solutionized condition, the 550 °C-3h aged material has even greater ability to demonstrate shape memory behavior at very high stresses, i.e., 1500 MPa along the [001] orientation and 1000 MPa along the [011] and [111] orientations, with very low irrecoverable strains. This benefit in dimensional stability is unfortunately accompanied by a general loss in total strain. For example, the 550 °C-3h aged [001] single crystals exhibit a maximum ε_{total} of ~0.7% (compared to about 1.1% for the solution treated condition). Total strains were 3% and 2.5% at 700 MPa along [011] and [111] directions, respectively, compared to the corresponding values for the solution treated condition of 3.1% and 3.7%. In this case, [111] appeared to be the orientation most impacted by aging in terms of a loss in transformation strain. But near perfect shape memory responses with irrecoverable strains of only 0.2% and 0.1% were observed for the [011] and [111] orientations, respectively, at 1000 MPa. In addition, the temperature hysteresis decreased in all aged conditions with a minimum value of 23 °C at 700 MPa along the [011] orientation, while it was still only 29 °C for the other orientations at this stress level.

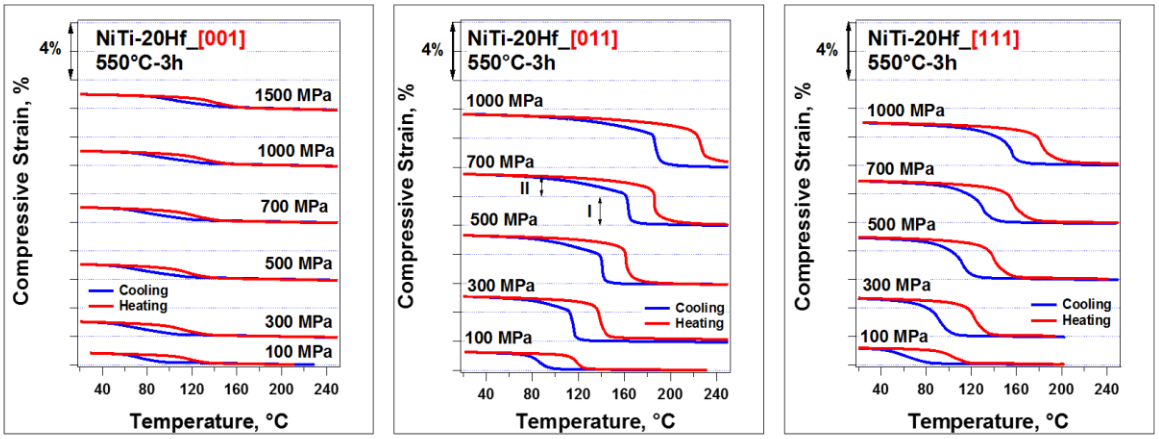

Figure 6.4: Strain vs. temperature responses for the 550 ºC-3h aged $Ni_{50.3}Ti_{29.7}Hf_{20}$ single crystals along the [001], [011], and [111] orientations.

Because the strength of the alloy improved after three hours aging at 550 °C due to the formation of fine and coherent precipitates, the irrecoverable strain along the [011] orientation decreased from 0.5 to 0.05% at 700 MPa. In the [111] orientation, irrecoverable strain also decreased from 0.12% for the solutionized case to 0.07% for the 550 °C-3h aged sample under 700 MPa.

Figure 6.5 shows the strain-temperature responses for the 650 °C-3h aged single crystals as a function of orientation. Aging at 650 °C-3h resulted in reduced total strains and dimensional stability along the [011] and [111] directions compared to the 550 °C-3h samples. The total strains of 2.5% was observed for both orientations and they exhibited irrecoverable strains of 0.8% and 0.3% at 700 MPa along the [011] and [111] orientations, respectively. In contrast, the shape memory behavior was very stable along the [001] orientation and no irrecoverable strain was observed even at 1500 MPa. However in this orientation, the thermal hysteresis increased from 28 to 40 °C while M_s was increased from 120 to 137 °C at 700 MPa when the aging temperature was increased from 550 to 650 °C.

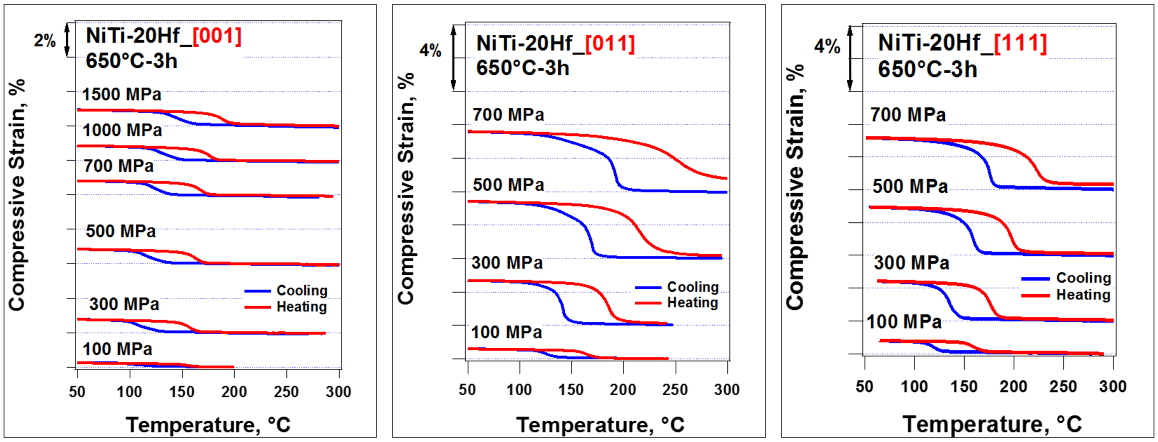

Figure 6.5: Strain vs. temperature responses for the 650 °C-3h aged $Ni_{50.3}Ti_{29.7}Hf_{20}$ single crystals along the [001], [011], and [111] orientations.

Thermal hysteresis of solutionized [001]-oriented single crystals decreased from 84 to 28 °C and 42 °C under 1000 MPa after three hours aging at 550 °C and 650 °C, respectively. In [111] orientation, the temperature hysteresis under 700 MPa was 64 °C, 30 °C and 47 °C for the solutionized, 550 °C-3h aged and 650 °C-3h aged samples, respectively. Although, thermal hysteresis for [011] orientation under 700 MPa was initially decreased from 60 to 23 °C after 550 °C-3h aging and it was increased to 68 °C for 650 °C-3h aging. It's clear that thermal hysteresis is always lowest and constant for all the stress levels after 550 ºC-3h aging in all orientations.

Summarizing the general observations concerning shape memory behavior of solutionized and aged NiTi-20Hf single crystals: i.) the ε_{total} along the [001] orientation was much smaller than the other two orientations, but the [001] orientation exhibited very stable behavior under stress with fully recoverable strain capability at stress levels as high as 1500 MPa. ii.) 550 °C-3h aging introduced fine precipitates in the material while 650 °C-3h aging resulted in a significantly coarsened precipitates. Consequently, precipitation strengthening was more pronounced after 550 °C-3h aging resulting in the best dimensional stability, lowest thermal hysteresis, and comparable or better transformation strains, while TTs were increased after 650 °C-3h aging.

6.2.3 Stress-strain Responses

As mentioned before, mechanical responses of SMAs are highly temperature dependent. If the temperature is above A_f (but below M_d), the stress-induced austenite to martensite transformation occurs after elastic deformation of the austenite phase. This process is followed by elastic deformation/detwinning and plastic deformation of the stress-induced martensite. The slope of the stress-strain curve during the stress-induced transformation mainly depends on the number of activated CVPs, plastic deformation, and storage of elastic energy [19, 70].

Stress-strain results of solutionized NiTi-20Hf single crystals as a function of temperature are shown in Figure 6.6. The σ_{SIM} increased with temperature and reached an approximate maximum value of 1700 MPa at 100 °C, 1000 MPa at 180 °C and 1200 MPa at 140 °C along the [001], [011] and [111] orientations, respectively. When samples were loaded to 4% total strain, near perfect superelasticity was observed from 40 to 100 °C along the [001] direction. Perfect superelasticity was observed over the temperature range of 40–180 °C for the [011] orientation and 40–120 °C along the [111] direction when loaded to a total strain of 5%. It should be noted that the total strain is composed of contributions of phase transformation and elastic strain. The observed superelastic windows were at least 140 °C and 80 °C along the [011] and [111] orientations, respectively. In addition, the mechanical hysteresis, which is the difference in stress values between the reverse and forward transformations, after 4% deformation are in the range of 900–1100 MPa, 400–500 MPa, and 500–600 MPa along the [001], [011], and [111] orientations, respectively.

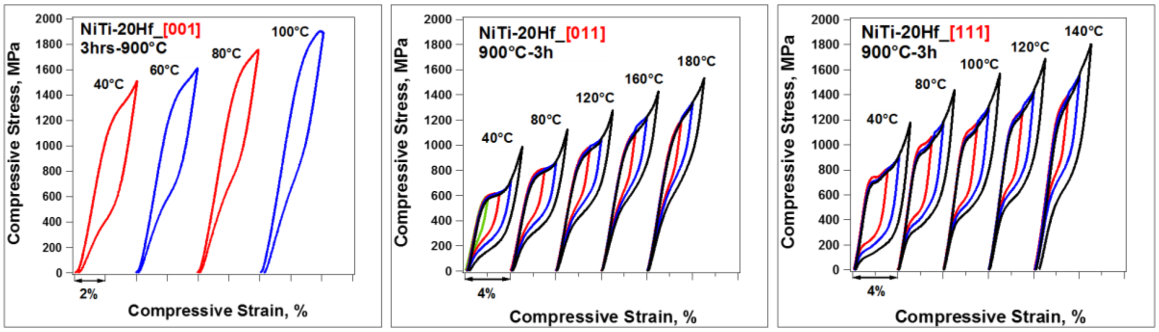

Figure 6.6: The isothermal compressive stress-strain responses of solutionized $Ni_{50.3}Ti_{29.7}Hf_{20}$ single crystals as a function of temperature and orientation.

Figure 6.7 illustrates the superelastic behavior of the 550 °C-3h aged NiTi-20Hf single crystals. In [001] orientation, stress cycling at 25 °C (when the alloy is martensite) resulted in 0.65% residual strain after unloading, which was fully recovered upon heating above A_f. However, no superelasticity was observed above A_f at test temperatures between 90 °C and 130 °C. In contrast, perfect superelasticity with a total strain of 5% was achieved over a temperature range of 140–200 °C for [011]-oriented samples. A further increase in test temperature to 220 °C led to an irrecoverable strain of 0.23% and increased stress hysteresis in this orientation. The critical stress to induce martensite formation was increased from 500 to 1100 MPa as temperature increased from 140 to 220 °C along the [011] direction. Similar to [011] orientation, perfect superelasticity was observed over a temperature range of 120–200 °C along the [111] orientation. The stress required for martensitic transformation increased from 600 to 1200 MPa as temperature increased from 120 to 180 °C for the [111] orientation.

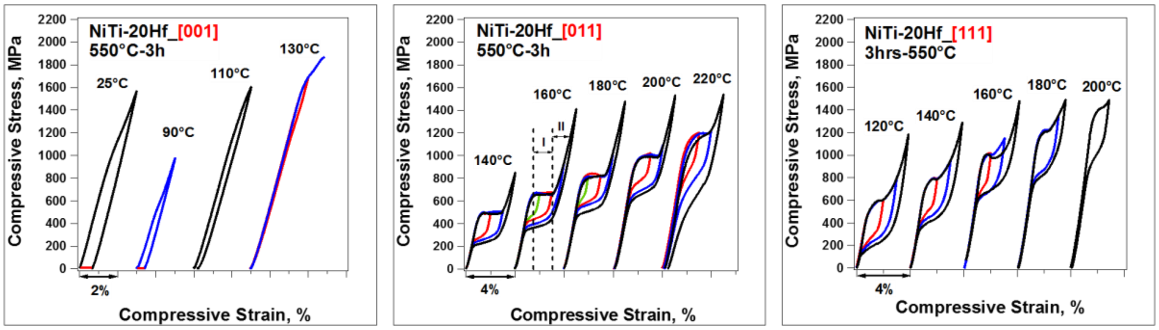

Figure 6.7: The isothermal compressive stress-strain responses of 550 °C-3h aged $Ni_{50.3}Ti_{29.7}Hf_{20}$ single crystals as a function of temperature and orientation.

Also, the slope during phase transformation was higher along the [111] direction than the [011] orientation after 550 °C-3h aging. The high slope during phase transformation can possibly be related to the activation and interaction of more CVPs or increased difficulty in dewtinning in [111] compared to the [011] orientation. It has been reported that CVPs may interact with each other and precipitates during transformation and consequently may result in a higher slope in the transformation region [19]. In addition, the stress hysteresis was 200–300 MPa and 300–400 MPa along the [011] and [111] orientations, respectively, which are lower than the values observed in the solutionized single crystals.

Figure 6.8 shows the compressive stress-strain responses of the 650 °C-3h aged NiTi-20Hf single crystals. Loading along the [001] direction at 40 °C and 140 °C (below A_f) resulted in residual strains upon unloading, however the strains were fully recovered after heating the samples above A_f. As the test temperature was increased above A_f, near perfect superelasticity with 4% strain was observed at 170 °C. The σ_{SIM} was as high as 1700 MPa at 170 °C and consequently the sample failed on loading at about 2 GPa. Near perfect superelasticity with negligible irrecoverable strain was experienced after 3% deformation in a narrow temperature range of 160 to 180 °C for the [011] and [111] orientations. As the test temperature increased to 200 °C, the stresses required for martensitic transformation reached 745 MPa and 1000 MPa for [011] and [111] directions, respectively, and irrecoverable strain was observed after loading to 4% total strain. It is worth noting that the temperature window for superelasticity was very narrow after 650 ºC-3h aging and the stress hysteresis was in the range of 500-600 MPa, 300-400 MPa, and 400-500 MPa along the [001], [011] and [111] orientations, respectively.

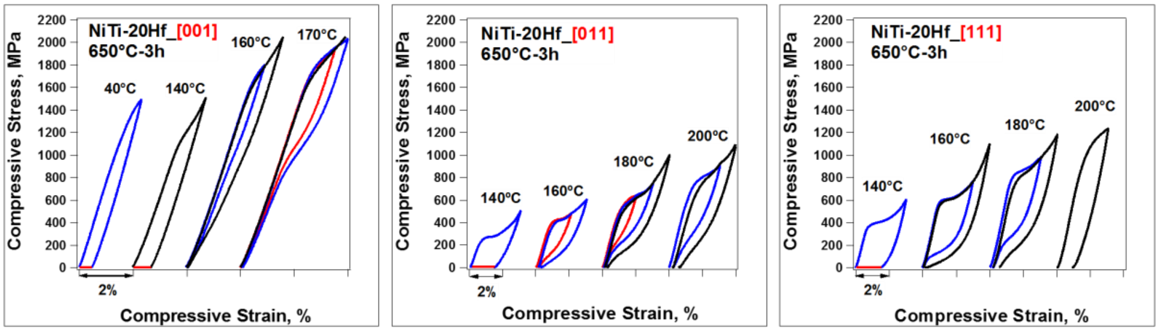

Figure 6.8: The isothermal compressive stress-strain responses of 650 °C-3h aged Ni$_{50.3}$Ti$_{29.7}$Hf$_{20}$ single crystals as a function of temperature and orientation.

6.3 Calculation of Theoretical Transformation Strains

Actuation strain is one of the main characteristics of SMA actuators. The phase transformation strain is highly orientation dependent in all SMAs due to the selection of particular martensite variants under external stress. The Ni$_{50.3}$Ti$_{29.7}$Hf$_{20}$ alloy undergoes a thermoelastic martensitic transformation from cubic B2 austenite phase with a lattice parameter of $a_0 = 0.3092$ nm to monoclinic B19′ martensite phase with lattice parameters of $a = 0.3062$ nm, $b = 0.4091$ nm, $c = 0.4872$ nm and $\beta = 103.3°$ upon cooling [114]. There are twelve lattice correspondence variants (CVs) in the B19′ martensite as listed in Table 6.1 [158]. In the present paper, transformation strains are theoretically estimated for the NiTi-20Hf alloy based on two different theories, i.e., the Energy Minimization Theory [74] and the Lattice Deformation Theory [75].

The energy minimization theory considers the existence of the invariant plane (habit plane) between austenite and martensite phases. The martensite plates with a certain pair of twin-related CVs can form habit planes. There are four possible twin relationships among the CV pairs (CVPs) in the martensite plate: $\{011\}_{B19'}$ type I, $\{\bar{1}\bar{1}1\}_{B19'}$ type I, $\langle 011\rangle_{B19'}$ type II and $\langle\bar{2}\bar{1}1\rangle_{B19'}$ type II. It is noted that the $\{011\}_{B19'}$ type I and $\{\bar{1}\bar{1}1\}_{B19'}$

type I twins are conjugates of the <011>$_{B19'}$ type II and <$\bar{2}\,\bar{1}\,1$>$_{B19'}$ type II twins, respectively. In the energy minimization theory, active CVPs are selected depending on the resolved shear stress on the most favorable CVPs under stress. The details of the calculation procedure of the B2-B19′ transformation strains can be found in work done by Sehitoglu et al. [19].

Table 6.1: The twelve lattice correspondence variants (CVs) for B19' monoclinic martensite [158].

variant	1	1′	2	2′	3	3′	4	4′	5	5′	6	6′
$[100]_{B19'}$	$[100]_{B2}$	$[\bar{1}00]_{B2}$	$[100]_{B2}$	$[\bar{1}00]_{B2}$	$[010]_{B2}$	$[0\bar{1}0]_{B2}$	$[010]_{B2}$	$[0\bar{1}0]_{B2}$	$[001]_{B2}$	$[00\bar{1}]_{B2}$	$[001]_{B2}$	$[00\bar{1}]_{B2}$
$[010]_{B19'}$	$[011]_{B2}$	$[0\bar{1}\bar{1}]_{B2}$	$[0\bar{1}1]_{B2}$	$[01\bar{1}]_{B2}$	$[101]_{B2}$	$[\bar{1}0\bar{1}]_{B2}$	$[10\bar{1}]_{B2}$	$[\bar{1}01]_{B2}$	$[110]_{B2}$	$[\bar{1}\bar{1}0]_{B2}$	$[\bar{1}10]_{B2}$	$[1\bar{1}0]_{B2}$
$[001]_{B19'}$	$[0\bar{1}1]_{B2}$	$[0\bar{1}1]_{B2}$	$[0\bar{1}\bar{1}]_{B2}$	$[0\bar{1}\bar{1}]_{B2}$	$[10\bar{1}]_{B2}$	$[10\bar{1}]_{B2}$	$[\bar{1}0\bar{1}]_{B2}$	$[\bar{1}0\bar{1}]_{B2}$	$[\bar{1}10]_{B2}$	$[\bar{1}10]_{B2}$	$[\bar{1}\bar{1}0]_{B2}$	$[\bar{1}\bar{1}0]_{B2}$

The 12 transformation matrices (U) with each one a function of the lattice parameter of cubic and monoclinic phases were determined in the cubic reference frame by using the 12 independent lattice correspondences in Table 6.1. For instance, the first transformation matrix can be defined as follows [19, 159, 160];

$$U_1 = \begin{bmatrix} \mathit{\Delta}_1 & \mathit{\Phi} & \mathit{\Phi} \\ \mathit{\Psi} & \Delta_2 & \mathit{\Psi} \\ \mathit{\Phi} & \mathit{\Phi} & \Delta_2 \end{bmatrix} \tag{6.1}$$

$$\mathit{\Delta}_1 = \frac{\alpha^2+\alpha\gamma\sin\theta}{\sqrt{\alpha^2+\gamma^2+2\alpha\gamma\sin\theta}} \tag{6.2}$$

$$\mathit{\Delta}_2 = \frac{1}{2}\left(\frac{\gamma^2+\alpha\gamma\sin\theta}{\sqrt{\alpha^2+\gamma^2+2\alpha\gamma\sin\theta}} + \beta\right) \tag{6.3}$$

$$\mathit{\Phi} = \frac{\alpha\gamma\cos\theta}{\sqrt{2(\alpha^2+\gamma^2+2\alpha\gamma\sin\theta)}} \tag{6.4}$$

$$\mathit{\Psi} = \frac{1}{2}\left(\frac{\gamma^2+\alpha\gamma\sin\theta}{\sqrt{\alpha^2+\gamma^2+2\alpha\gamma\sin\theta}} - \beta\right) \tag{6.5}$$

Where $\alpha = \frac{a}{a0}$, $\beta = \frac{b}{\sqrt{2}a0}$, and $\gamma = \frac{c}{\sqrt{2}a0}$. a_0, a, b, and c are lattice parameters and θ is the monoclinic angle between b and c.

There are two kinds of invariant plane in the twinned martensite. One is the twin plane (interface between the two lattice correspondence variants), the other is the habit plane (interphase between the twin martensite and parent phase). In order to calculate the habit plane parameters, first we need to form the symmetry matrix C as follows [19];

$$C = U_i^{-1}.U_j^{2}.U_i^{-1} \tag{6.6}$$

The symmetry matrix *C* has ordered eigenvalues $\lambda_1 < \lambda_2 = 1 < \lambda_3$. By calculating the eigenvalues, the twinning shear vector *(a)* and twin plane normal *(n)* are going to be determined using the following equations [19]:

$$a = \rho(\sqrt{\frac{\lambda_3(\lambda_2-\lambda_1)}{\lambda_3-\lambda_1}}e_1 + k\sqrt{\frac{\lambda_1(\lambda_3-\lambda_2)}{\lambda_3-\lambda_1}}e_3) \tag{6.7}$$

$$n = U_i^{-1}.[\rho^{-1}\left(\frac{\sqrt{\lambda_3}-\sqrt{\lambda_1}}{\sqrt{\lambda_3-\lambda_1}}\right)\left(-\sqrt{\lambda_2-\lambda_1}e_1 + k\sqrt{\lambda_3-\lambda_2}e_3\right)] \tag{6.8}$$

where e_1, e_2 and e_3 are the eigenvectors of matrix *C* corresponding to λ_1, λ_2 and λ_3, respectively. The constant ρ represents an invariant scaling of the solution. The constant k will take the values of ±1.

In near-equiatomic NiTi alloys, the $<011>_{B19'}$ type II twin is the dominant twinning observed in martensite plates [77] while $\{011\}_{B19'}$ type I twins have been frequently observed in Ni rich NiTiHf alloys [114, 136]. In the case of $Ni_{50.3}Ti_{29.7}Hf_{20}$, the twinning elements of the $\{011\}_{B19'}$ type I twin are K_1 (twinning plane) = $\{011\}_{B19'}$ ($\{100\}_{B2}$), K_2 (conjugate twinning plane) = $\{0.9805, 1, \bar{1}\}_{B19'}$ ($\{0, 0.9805, 1\}_{B2}$), η_1 (twinning direction)

= <2.1331, 1, $\bar{1}$>$_{B19'}$ (<0, 1.0665, 1>$_{B2}$), η_2 (conjugate twinning direction) = <011>$_{B19'}$ (<100>$_{B2}$) and s (twinning shear) = 0.4676. The volume fraction of the minor CV in the {011}$_{B19'}$ type I twins was determined to be f = 0.4423.

The corresponding solution of habit plane normal (m) and shear direction (b) can be calculated as follows;

$$b = \rho\left(\sqrt{\frac{\lambda_3(\lambda_2-\lambda_1)}{\lambda_3-\lambda_1}}e_1 + k\sqrt{\frac{\lambda_1(\lambda_3-\lambda_2)}{\lambda_3-\lambda_1}}e_3\right) \tag{6.9}$$

$$m = \rho^{-1}\left(\frac{\sqrt{\lambda_3}-\sqrt{\lambda_1}}{\sqrt{\lambda_3-\lambda_1}}\right)\left(-\sqrt{\lambda_2-\lambda_1}e_1 + k\sqrt{\lambda_3-\lambda_2}e_3\right) \tag{6.10}$$

Two sets of the habit plane normal and the shape strain direction were calculated to be ***m*** = {0.9827, 0.1583, 0.0957}$_{B2}$ and ***b*** = <$\overline{0.0266}$, 0.1815, 0.0204>$_{B2}$ or ***m*** = {0.9915, 0.1186, 0.0529}$_{B2}$ and ***b*** = <0.0125, 0.0158, $\overline{0.1835}$>$_{B2}$. It is noted that {011}$_{B19'}$ type I twin related martensite plates in NiTiHf alloys contain (001)$_{B19'}$ compound twins [106, 112], which would affect the habit plane and the amount of transformation strain. However, since the internal (001)$_{B19'}$ compound twins cannot be calculated by the energy minimization theory, the effects of the compound twin on theoretical strain calculations cannot be considered in this section.

By calculating the habit plane parameters we can evaluate the average deformation gradient using the following equation [19];

$$F_M - I = b \otimes m \tag{6.11}$$

where F_M represents the deformation gradient and I is the identity tensor. If the twins are fine enough then F_M will satisfy the following equation [19];

$$F_M = R_h[fR_{ij}U_i + (1-f)U_i] \tag{6.12}$$

where R_h is the relative rotation between austenite and twinned martensite phases, f is the martensitic volume fraction and U_i and U_j are correspondence variants. The strain will be determined by using the following equation [19];

$$\varepsilon = \frac{1}{2}(F_M^T.F_M - I) = \frac{1}{2}[b\otimes m + m\otimes b + (b.b)m\otimes m] \tag{6.13}$$

Once the orientation of the loading axis is selected, the resolved shear stress factor (RSSF) can be calculated from the habit plane normal ($\boldsymbol{m}$) and the shape strain direction ($\boldsymbol{b}$) as follows [19];

$$RSSF = (b.e)(m.e)/|b| \tag{6.14}$$

where e denotes the single crystal loading direction. The active CVPs are determined according to the maximum RSSF and the transformation strain can be calculated from the active CVPs. The transformation strain produced by the active CVPs is denoted as CVP strain hereafter. The application of further stress to active CVPs causes the detwinning of the CVPs. The single variant (detwinned CVP) strain can be calculated when the volume fraction of the minor CV is set as zero. In this section, the CVP strain and the single variant (detwinned CVP) strain for NiTi-20Hf were calculated.

On the other hand, the lattice deformation theory does not consider the existence of habit planes. The theory assumes that the austenite transforms into a single crystal of martensite without twins. First, the transformation strains along the loading axis are calculated for all the twelve CVs from the lattice parameters of the austenite and martensite phases and the lattice correspondence shown in Table 6.1. The active CVs are considered the CVs that produce the maximum transformation strain along the loading axis. The details of the calculation procedure of the transformation strains are described in Ref. [75].

Figure 6.9 shows the calculated RSSFs, CVP strains and single variant (detwinned CVP) strains from the energy minimization theory expressed by contour lines for each orientation in a standard stereographic triangle for type I twinning. The orientation dependence of the RSSFs and transformation strains is shown for both $\{011\}_{B19'}$ type I and $\{\bar{1}\bar{1}1\}_{B19'}$ type I twinning modes. High RSSFs and large CVP strains are obtained for orientations close to $<011>_{B2}$ for the two twinning modes. The single variant (detwinned CVP) strain shows the maximum value at an orientation close to $<112>_{B2}$.

The transformation strains calculated using the energy minimization theory and the lattice deformation theory are summarized in Table 6.2 for compression axes of $[001]_{B2}$, $[011]_{B2}$ and $[111]_{B2}$. The possible four twinning modes in the energy minimization theory, volume fractions of the minor CVs, active CVPs, RSSFs, CVP strains and single variant (detwinned CVP) strains are included in the table. A CVP is represented as (*i*,*j*) in Table 6.2 where *i* is the major CV and *j* is the minor CV in the CVP. The transformation strains with active CVs obtained from the lattice deformation theory are also listed in Table 6.2. The activity of dislocation slip systems is also dependent on the crystal orientation. The Schmid factors of two slip systems in B2 austenite, $\{011\}_{B2}<100>_{B2}$ and $\{001\}_{B2}<100>_{B2}$ [161, 162], were calculated and listed in Table 6.2.

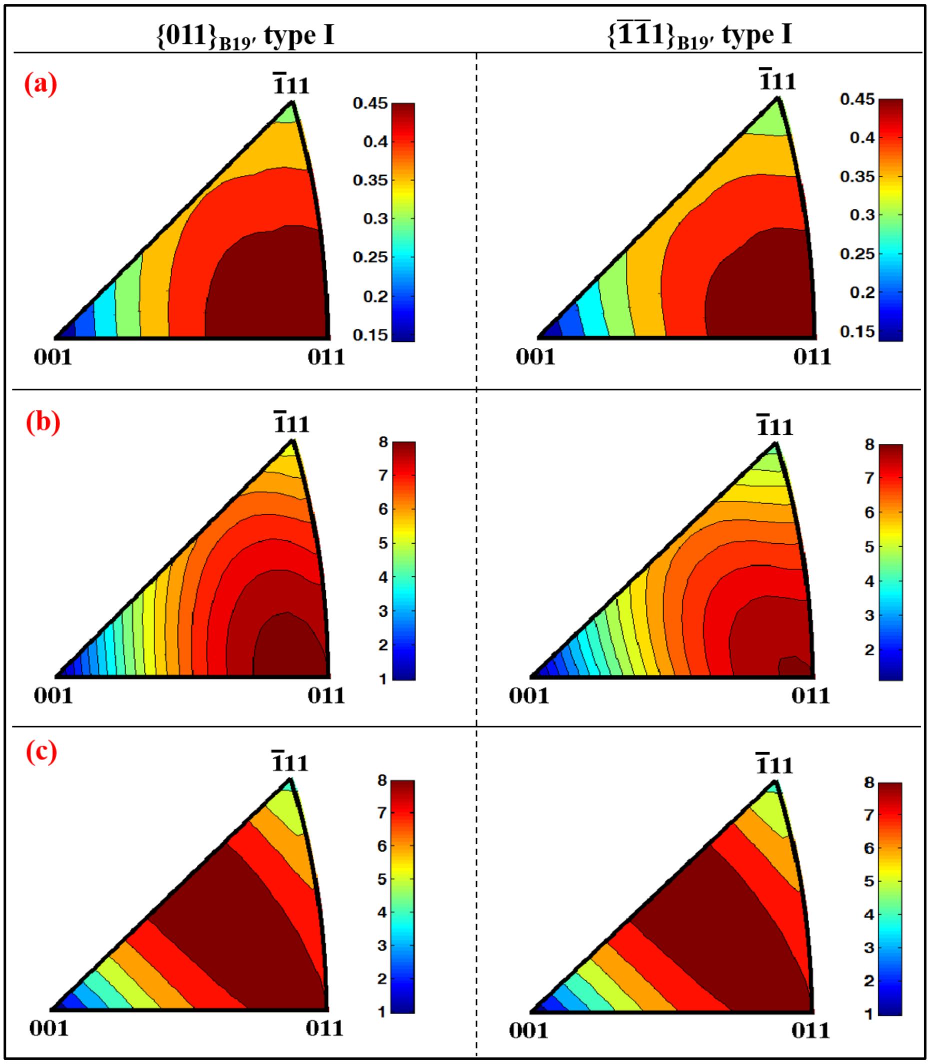

Figure 6.9: (a) RSSF, (b) CVP strain, and (c) single variant (detwinned CVP) strain contours under compression for NiTi-20Hf for $\{011\}_{B19'}$ type I and $\{\bar{1}\bar{1}1\}_{B19'}$ type I twinning.

In all the three orientations of $[001]_{B2}$, $[011]_{B2}$ and $[111]_{B2}$, the single variant (detwinned CVP) strains are almost the same as the CVP stains. Both energy minimization and lattice deformation theories give almost the same single variant strains since the major CVs obtained from the two theories are the same in most of the cases. In the $[011]_{B2}$ orientation, RSSFs have high values of about 0.5 for the four twinning modes. Correspondingly, the Schmid factors of the $\{011\}_{B2}<100>_{B2}$ and $\{001\}_{B2}<100>_{B2}$ slip systems are 0.354 and the maximum value of 0.5, respectively. RSSFs are around 0.3 for the $[111]_{B2}$ orientation for the four twinning modes. The Schmid factor of the $\{001\}_{B2}<100>_{B2}$ slip system is also around 0.3 while that of the $\{011\}_{B2}<100>_{B2}$ system has a higher value of 0.471. In the $[001]_{B2}$ orientation, almost zero RSSFs are obtained for the four twinning modes, while Schmid factors are zero for the two slip systems.

Table 6.2: Calculated active martensite variants, volume fractions of the minor variants, RSSF, CVP strains, and single variant (detwinned CVP) strains for compression along the $[001]_{B2}$, $[011]_{B2}$ and $[111]_{B2}$ based on the energy minimization theory and the lattice deformation theory.

		$\{011\}_{B19'}$ type I	$\{\bar{1}\bar{1}1\}_{B19'}$ type I	$<011>_{B19'}$ type II	$<\bar{2}\bar{1}1>_{B19'}$ type II	Lattice deformation	$\{011\}_{B2}<100>_{B2}$ slip	$\{001\}_{B2}<100>_{B2}$ slip
	Volume fraction	0.4423	0.3213	0.3152	0.4415			
$[001]_{B2}$	Active variants	(5,6) (5,6′) (5′,6) (5′,6′) (6,5) (6,5′) (6′,5) (6′,5′)	(5,2) (5,3′) (5′,1) (5′,4) (6,1′) (6,3) (6′,2′) (6′,4′)	(5,6) (5,6′) (5′,6) (5′,6′) (6,5) (6,5′) (6′,5) (6′,5′)	(5,2) (5,3′) (5′,1) (5′,4) (6,1′) (6,3) (6′,2′) (6′,4′)	(5) (5′) (6) (6′)		
	RSSF	0.141	0.138	0.203	0.050		0	0
	CVP strain (%)	-0.97	-1.11	-2.28	0.72			
	Single variant (detwinned CVP) strain (%)	-0.97	-0.97	-0.97	-0.97	-0.97		
$[011]_{B2}$	Active variants	(3′,4′) (4′,3′) (5,6′) (6′,5)	(3′,5) (4′,6′) (5,3′) (6′,4′)	(3′,4′) (4′,3′) (5,6′) (6′,5)	(3′,5) (4′,6′) (5,3′) (6′,4′)	(3′) (4′) (5) (6′)		
	RSSF	0.484	0.487	0.478	0.485		0.354	0.500
	CVP strain (%)	-8.00	-8.00	-8.00	-8.06			
	Single variant (detwinned CVP) strain (%)	-8.00	-8.00	-8.00	-8.00	-8.35		
$[111]_{B2}$	Active variants	(2′,1) (2′,1′) (4′,3) (4′,3′) (6′,5) (6′,5′)	(1,5′) (1′,3) (3,1′) (3′,5) (5,3′) (5′,1)	(2′,1) (2′,1′) (4′,3) (4′,3′) (6′,5) (6′,5′)	(2′,4′) (2′,6′) (4′,2′) (4′,6′) (6′,2′) (6′,4′)	(1) (1′) (3) (3′) (5) (5′)		
	RSSF	0.326	0.299	0.298	0.343		0.471	0.333
	CVP strain (%)	-5.25	-4.48	-4.32	-5.57			
	Single variant (detwinned CVP) strain (%)	-4.24	-4.48	-4.24	-4.24	-4.58		

The $[011]_{B2}$ orientation has the largest CVP strains of the three orientations, of around –8%. The $[111]_{B2}$ orientation exhibits CVP strains from –4.3 to –5.6% depending on the twinning modes. On the other hand, small CVP strains with a maximum of –2.3% are obtained in the $[001]_{B2}$ orientation. For the case of the $<\bar{2}\,\bar{1}\,1>_{B19'}$ type II twinning, the $[001]_{B2}$ orientation shows a tensile CVP strain of 0.72%, It should be noted that observation of tensile strain under compressive stress is not expected.

6.4 Discussion

6.4.1 Transformation Strain

Figure 6.10 summarizes the effect of compressive stress on the recoverable strain (ε_{rec}), extracted from the thermal cycling experiments shown in Figures 6.3, 6.4 and 6.5. Recoverable strain increases initially and then saturates with stress for all orientations. Such progression in ε_{rec} is the consequence of the evolution of martensite variants as a function of external stress. As mentioned before, a small ε_{rec} at low stresses can be attributed to the fact that applied stress is not sufficient to completely bias the formation of self-accommodating martensitic structures. The volume fraction of preferred variants increases with stress and therefore, so does the ε_{rec}. Eventually the increase in ε_{rec} saturates as the fraction of preferred variants approaches 100%.

The decrease in ε_{rec} after aging can be attributed to the presence of precipitates. Since the precipitates do not undergo phase transformation, the volume fraction of the alloy that transforms to martensite decreases. Recoverable strain reached to maximum values of 3.2%, 3% and 2.9% at 500 MPa for solutionized, 550 °C-3h, and 650 °C-3h aged conditions, respectively, along the [011] orientation. The absolute highest ε_{rec} among all conditions was observed for the solutionized [111] orientation, which was 3.7% at 500 MPa. The maximum ε_{rec} along the [111] orientation for 550 °C-3h and 650 °C-3h aged samples was 2.5% at 700 MPa. Finally, for the [001] orientation, the ε_{rec} reached a maximum value of 1.1% in the solutionized condition and decreased to 0.7% after aging.

Although the values of theoretically calculated transformation strains (Table 6.2 and Figure 6.9) do not match well with the experimentally observed transformation strains, but they capture some trends. Furthermore, the effects of aging are not considered in theoretical strain calculations. Therefore it is better to compare the theoretical results with the strains measured in the solutionized samples. The maximum transformation strains observed experimentally were 1.1%, 3.1% and 3.7% compared to theoretical strains for Type-I twinning which are 2.4%, 8% and 5.6% along the [001], [011], and [111] orientations, respectively. It is clear that in both cases the lowest strain is observed along the [001] orientation. The largest difference between the theoretical and experimental results is observed along the [011] orientation. However, due to high stress levels and the high RSSF for slip in this orientation (Table 6.2), it is difficult to determine the maximum transformation strain that might be possible because plastic deformation may have interrupted the transformation process. In addition, the main difference between the experimental and theoretical strains can be attributed to the formation multiple interacting Type-I twins in the actual material, whereas the calculations assume transformation to a single variant of martensite. Finally, the effect of compound twins inside the martensite variants, cannot be captured in the theoretical calculations.

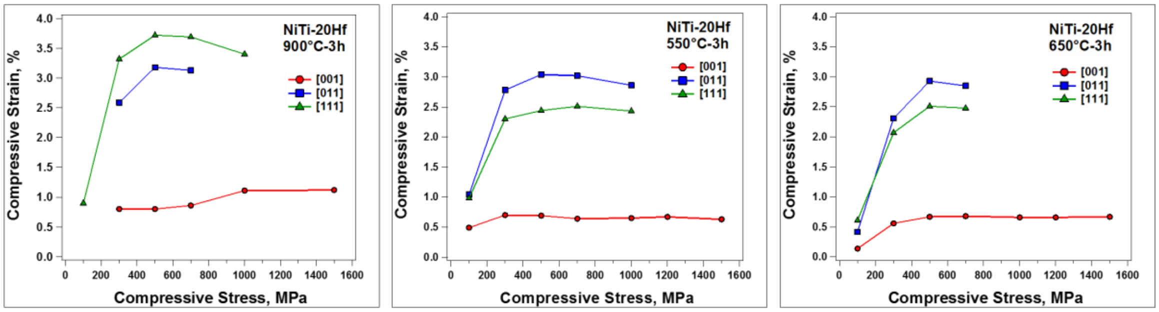

Figure 6.10: Recoverable strain of solutionized and aged $Ni_{50.3}Ti_{29.7}Hf_{20}$ single crystal as function of applied compressive stress along the [001], [011], and [111] orientations.

It is worth noting the stability of the ε_{rec} with stress in the [001] orientation, even at applied stresses as high as 1500 MPa. This is a consequence of the zero RSSF for the two <100> type slip systems in B2 alloys along the [001] orientation, which results in the absence of plastic deformation and thus leads to stable and fully reversible shape memory behavior at very high stresses. Unfortunately, the recoverable strains in this orientation are also very small, as confirmed theoretically.

6.4.2 Thermal Hysteresis

Aging is a fundamental method to improve the shape memory and mechanical properties of $Ni_{50.3}Ti_{29.7}Hf_{20}$ alloys. It can be seen that while the solutionized $Ni_{50.3}Ti_{29.7}Hf_{20}$ alloy has low TTs, aging can improve the situation making the alloy a viable candidate for HTSMA applications. When the solutionized material was aged at 550 °C for three hours, fine H-phase precipitates with the size of ~15–20 nm were formed and M_s was increased from –23 to 73 °C. In addition, the aged material exhibited good dimensional stability up to 1500 MPa along the [001] and 1000 MPa along [011] and [111] orientations, with negligible irrecoverable strains. Moreover, perfect superelasticity with 5% recoverable strain was observed at temperatures in the range of 120–200 °C along [011] and [111] orientations. Aging at 650 °C-3h resulted in much larger precipitates. This led to a further increase in M_s to 125 °C, but resulted in lower strength, a much smaller superelastic window, higher irrecoverable strains, and a much wider thermal hysteresis.

Thermal hysteresis stems from structural defect (e.g. dislocation) formation and dissipated frictional energy due to resistance to the movement of phase boundaries. Figure 6.11 summarizes the temperature hysteresis of the solutionized and aged $Ni_{50.3}Ti_{29.7}Hf_{20}$ single crystals as functions of stress and orientation. It is clear that thermal hysteresis is wider in solutionized samples compared to the aged condition. This can be attributed to the increased stored elastic strain energy and frictional dissipation [37, 163]. When the strength of the material was improved by the formation of precipitates the dissipated energy decreased due to reduced contributions from plastic deformation. The wide hysteresis for 650 °C-3h aged crystals can be attributed to lack of precipitation hardening leading to increased plasticity when the particles are large and incoherent.

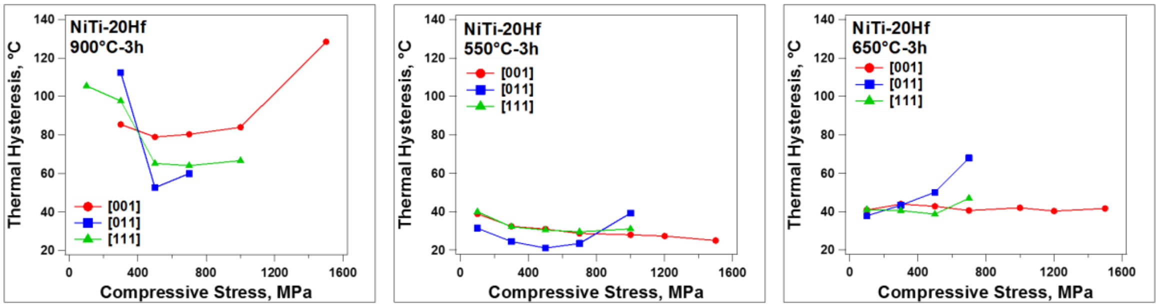

Figure 6.11: Thermal hysteresis of solutionized and aged $Ni_{50.3}Ti_{29.7}Hf_{20}$ single crystals as functions of applied compressive stress along the [001], [011], and [111] orientations.

For solutionized and 550 °C-3h aged [110] and [111] crystals, the thermal hysteresis initially decreased with stress and then increased at higher stress levels. The decrease can be attributed to the increased volume fraction of favored martensite variants with stress, which decreases the interaction between variant interfaces. At high stress levels, plastic deformation was introduced into the material increasing the thermal hysteresis.

6.4.3 Transformation Behavior in [011] Crystal

The thermal cycling responses under low (100 MPa) and moderate to high (≥300 MPa) stress levels are very different along the [011] orientation, especially for the 550 °C-3h aged sample. A symmetric strain-temperature curve was observed at 100 MPa, where the strain changes nearly linearly with temperature on heating and cooling. However, the strain-temperature curve is asymmetric at stresses ≥300 MPa. At the higher stresses, the cooling portion of the strain-temperature curve exhibits a two stage behavior. Initially strain decreases rapidly at first (Figure 6.4, stage I) and then a significant change in slope occurs with the strain changing much more gradually but linearly over a wide temperature range to completion of the martensite formation (Figure 6.4, stage II). During heating the response is single stage and the transformation occurs over a narrow temperature range A_s to A_f. The first stage of rapid decrease in strain during cooling is due to the formation of preferred martensite variants (CVPs). The second stage is apparently formation of additional martensite variants that are propagation limited or detwinning, requiring significant undercooling to complete. It is likely that multiple type-I and type-II variants are formed on initial cooling (Stage 1), since the RSSF for all four variant types in Table 6.2 are essentially the same. As the primary variants grow and interact, there will be regions between these initial variants that need to form a more accommodative martensite to allow the transformation to continue to completion. This behavior would also explain the low transformation strains in this orientation and the large discrepancy between theoretical and experimental strains.

In addition, the slope of strain-temperature response provides information on the elastic energy storage. When multivariants of martensite are formed, the stored energy is large due to variant-variant interaction and it helps the martensite to austenite back transformation. During the formation of single variant of martensite the stored elastic energy is very small, resulting in a very steep slope of strain-temperature, but during detwinning process the stored elastic energy increases resulting in overcooling to accomplish the transformation. During heating, the stored elastic energy helps the formation of twinned martensite from detwinned martensite at first, and then single variant of martensite transforms back to austenite. Similar behavior can also be seen in superelasticity test of 550 °C-aged [011] orientation at 160 °C where during loading, initially a plateau is observed due to the formation of a single variant of twinned martensite and then hardening occurs due to detwinning.

6.4.4 Transformation Temperatures

Figure 6.12 illustrates the M_s of single crystals as a function of applied stress and orientation, determined from the strain-temperature curves from Figures 6.3, 6.4 and 6.5. The results indicate that M_s increases linearly with stress which satisfies the CC relation. The T_0 and ΔH are independent of crystal orientation, while ε_{tr} is strongly orientation dependent. It is clear that the CC slope is inversely proportional to ε_{tr}, with [001] samples exhibiting the highest CC slopes for each condition.

For the solutionized condition, [001] had the highest CC slope of 9.66 MPa/ °C, while [011] and [111] orientations had CC slopes of 5.52 MPa/ °C and 5.29 MPa/ °C, respectively, consistent with the [001] orientation having the lowest transformation strain among all orientations. The transformation strain was lowest in [001] after aging, which resulted in the highest CC slopes, in the range of 30-40 MPa/ °C. The CC slopes along the [011] and [111] orientations were independent of aging treatment and were about 9 MPa/ °C and 11 MPa/ °C after aging at 550 °C-3h and 650 °C-3h, respectively.

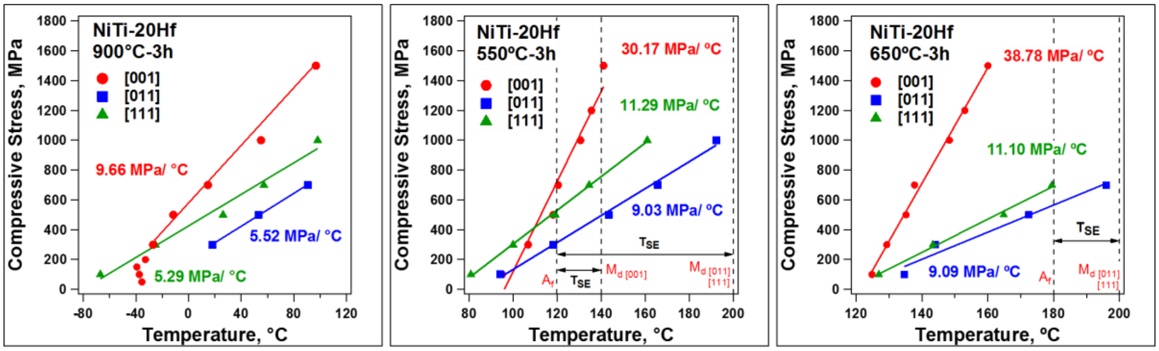

Figure 6.12: Stress vs. temperature relationship of solutionized and aged $Ni_{50.3}Ti_{29.7}Hf_{20}$ single crystal along the [001], [111], and [011] orientations.

It is worth to note that the stress do not have linear relationship with temperature at low stress levels as shown in solutionized [001] orientation. The behavior could be attributed to the fact that mechanical stress is functions of strain, chemical, elastic and dissipation energies where $\sigma_{mech} = \frac{1}{\varepsilon}\left(\Delta G_{chemical} + \Delta G_{elastic} + \Delta G_{dissipatoin}\right)$. Dissipation energy is a function of applied stress during thermal cycles for solutionized condition and thermal hysteresis was varied with stress. In contrast to aged conditions, the difference between the thermal hysteresis at low and high stress levels is larger for solutionized case, hence, the mechanical stress is not linear function of temperature at low stresses. For instance, the thermal hysteresis does not change that much with stress level for 650 °C-3h condition and as a result the lines intersect each other at a same point at low stress levels, while for solutionized case the dissipation energy is function of stress and there is no linear relation between stress and temperature at low stress levels.

6.4.5 Superelastic Temperature Window

The temperature window over which superelastic behavior occurs is narrow for the [001] orientation and 650 °C-3h aged samples. This is because the superelastic temperature window highly depends on the CC slope, thermal hysteresis, and yield strength. According to Liu and Galvin [164], the criteria for superelasticity can be written as

$$\sigma_y > 2\sigma_0 + (A_f - M_s)\frac{\Delta\sigma}{\Delta T} \tag{6.15}$$

where σ_y is the austenite yield strength, σ_0 is the minimum stress level required for stress-induced martensitic transformation, and $A_f - M_s$ is the thermal hysteresis. From this relationship, the superelastic temperature window can be calculated as

$$T_{SE} = \sigma_y \ / \frac{\Delta\sigma}{\Delta T} - (A_f - M_s) \tag{6.16}$$

It is clear from Equation 6.16 that T_{SE} increases with yield strength. Thus, precipitation hardening is expected to increase the superelastic window. However, a high volume fraction of precipitate phase will result in a decrease in transformation strain, which increases the CC slope. If we assume that yield strength is constant, a steep CC slope diminishes the temperature window for superelasticity since the critical stress for phase transformation reaches the yield strength over a smaller temperature range. Also, yield strength in general decreases with increasing temperature so that materials with high TTs may exhibit lower $T_{SE.}$

Thus, lack of superelasticity in aged [001] samples can be attributed to the fact that stress required to induce the martensite transformation is higher than the stress required for slip due to a large CC slope. In contrast, perfect superelasticity was observed for solutionized and 550 °C-3h aged conditions along the [011] and [111] orientations, but the superelastic temperature window decreased after aging for [011] orientation. The superelastic window was the same for the [111] crystals in both the solutionized and 550 °C-3h aged conditions, i.e., 80 °C, though the temperature range was higher in the case of the aged sample. Along the [011] orientation, the decrease in superelastic window for the aged material compared to the solution treated was due to a decreasing yield strength with increasing temperature and the very high stress needed to initiate the stress-induced transformation at temperatures above 200 °C.

After aging at 650 °C-3h, the TTs and thermal hysteresis increased and the strength of material decreased compared to the 550 °C-3h aged samples. Since both 550 °C-3h and 650 °C-3h aged samples have similar CC slopes along [011] and [111] directions, poor superelasticity in the 650 °C-3h condition can be attributed to the large hysteresis and lower yield strength of the material.

6.4.6 Comparison to NiTi and NiTiHf-based Alloys

It is worth comparing the results of the $Ni_{50.3}Ti_{29.7}Hf_{20}$ single crystals with those reported previously on NiTi shape memory single crystals. Single crystal $Ni_{51.5}Ti_{48.5}$ (at. %) has M_s temperatures below –196 °C and –37 °C in the solutionized (1000 °C-2h) and overaged (550 °C-1.5h) conditions, respectively [70]. Superelasticity with recoverable compressive strains of 3.9%, 4.2% , and 1.2% for solutionized and 3.3% , 3.7% , and 3% for overaged single crystals was reported along [001], [110], and [111] orientations, respectively. In addition, the experimentally recoverable strains under compression in $Ni_{50.8}Ti_{49.2}$ were 3.5%, 3.2%, and 2.3% for samples aged at 400 °C-1.5h and 4.3%, 3.6% , and 3% after aging at 500 °C-1.5h along [100], [110], and [111] directions, respectively [79].

These studies [70, 124] indicate that the transformation strain was minimum along the [111] orientation in binary NiTi, but current results indicate that the minimum in transformation strain occurs along [001] for $Ni_{50.3}Ti_{29.7}Hf_{20}$. The maximum transformation strain was observed along the [111] orientation for $Ni_{50.3}Ti_{29.7}Hf_{20}$ compared to the [100] and [110] orientations in $Ni_{51.5}Ti_{48.5}$ and $Ni_{50.8}Ti_{49.2}$, respectively. Even though the NiTi and NiTiHf alloys have the same crystal structures for the austenite (B2) and martensite (B19') phases, their maximum and minimum transformation strains are observed along different orientations under compression. This can be attributed to differences in the active twining types of martensite, where the $<011>_{B19'}$ type II twin is the dominant twinning mode in NiTi, while the $\{011\}_{B19'}$ type I twin is the dominant twinning observed in martensite plates of NiTiHf.

Studies have also been conducted on the orientation dependence of shape memory properties of a similar alloy, $Ni_{45.3}Ti_{29.7}Hf_{20}Pd_5$ [124, 126, 127, 165]. Perfect superelasticity with 4.2% recoverable strain was attained between –30 °C and 70 °C and the alloy exhibited yield strength greater than 2500 MPa along the [111] orientation in the solution treated condition [127]. After three hours aging at 550 °C, shape memory behavior with maximum reversible strains of 2.2%, 2.7% and 0.7% at 1000 MPa and fully recoverable superelastic responses were observed along [111], [011] and [-117] orientations, respectively [165]. This study also demonstrated that the CC relation was a strong function of orientation and aging condition, where the CC slopes for 550 °C-3h aged samples increased from 11.1 MPa/ °C, 8.2 MPa/ °C, and 27.6 MPa/ °C to 12.5 MPa/ °C, 9.3 MPa/ °C, and 42.2 MPa/ °C after aging at 600 °C for 48h along [111], [011], and [-117] orientations, respectively [165]. Thus, we can conclude that the $Ni_{50.3}Ti_{29.7}Hf_{20}$ alloy shows similar behavior to $Ni_{45.3}Ti_{29.7}Hf_{20}Pd_5$, but can exhibit higher transformation temperatures and strains upon aging.

It can be suggested that the shape memory properties of the polycrystalline $Ni_{50.3}Ti_{29.7}Hf_{20}$ alloy can be improved by texturing along [001], [011], or [111] for a desired set of properties. [100] texture can be used for stable shape memory behavior under high stress, while [111] and [011] can be chosen for large transformation strains and wide superelastic window. In addition, aging can be used to tailor the microstructure and thus shape memory properties by introducing nano-size precipitates in the matrix.

6.5 Conclusion

In this chapter, the orientation dependence of shape memory properties of solutionized and aged $Ni_{50.3}Ti_{29.7}Hf_{20}$ single crystals were investigated. The following conclusions were drawn from the present work:

1. Transformation temperatures and shape memory properties of $Ni_{50.3}Ti_{29.7}Hf_{20}$ alloys can be tailored by aging. Aging at 550 °C-3h introduced nano-size coherent precipitates in the matrix and thus improved the strength and shape memory behavior of the single crystals. Aging at 650 °C-3h can be used to increase the martensitic transformation temperatures, however, precipitation hardening was diminished due to the formation of large precipitates.

2. Among the three orientations, [001]-oriented single crystals have the highest strength and exhibit limited plastic strain during thermal cycling even at 1500 MPa. The transformation strain and thermal hysteresis are low along the [001] orientation and no superelastic behavior has been observed due to the higher critical stress for martensitic transformation. The [001] orientation exhibits a dramatic increase in critical stress with temperature with a CC slope of about 30 MPa/ °C.
3. Shape memory behavior with 3.7% and 2.5% recoverable strain at a 1000 MPa can be observed in solutionized and 550 °C-3h aged conditions of [111]–oriented single crystals, respectively. Perfect superelasticity with 5% recoverable strain is observed for temperature ranges of 40–120 °C and 120–180 °C for the solutionized and 550 °C-3h aged crystals, respectively. The [111] orientation has the CC slope in the range of 5–11 MPa/ °C.
4. Transformation strains of 3.6% and 3.1% was obtained by thermal cycling under 700 MPa for the solutionized and 550 °C-3h aged conditions along the [011] orientation, respectively. The [011] orientation exhibited perfect superelasticity with 5% recoverable strain for over a temperature range of 40–180 °C and 140–200 °C for solutionized and 550 °C-3h aged samples, respectively. The CC slope of [011]-oriented single crystals is in the range of 5–9 MPa/ °C.

7 Summary and Future Works

7.1 Summary and Conclusion

Development of HTSMAs for a wide range of applications in aerospace, energy and automotive industries connecting the gap of the astonishing properties of this class of materials. The requirements of the industries for the commercial applications, specifically the requirement of TTs to be higher than 100 °C, as well as other number of properties including ductility, thermal and dimensional stability, fatigue life and high work output that can be derived out from the material. Among all the NiTi-based HTSMAs, NiTiHf alloys have relatively lower cost comparing to NiTi(Pd, Pt, Au) alloys that makes them suitable nominee for large scale of applications. In addition, Ni-rich NiTiHf alloys have the abilities to show superelasticity at high temperatures and shape memory effect under high stress levels [5, 136].

In this study, a detailed investigation on shape memory properties and transformation behavior of single crystal and polycrystalline Ni-rich NiTiHf alloys was carried out. The alloys contained 20 at. % Hf and the Ni content was varied from 50.3 to 52 at. %. The alloys were precipitation hardenable, have excellent dimensional stability at high stress levels with narrow hysteresis which made them a promising candidates for high force actuator applications at wide temperature ranges.

It was shown that small changes in chemical composition are very effective to tailor the shape memory and material properties of Ni-rich NiTiHf alloys. It has been shown that H-phase precipitates were formed in furnace cooled NiTiHf alloy due to furnace cooling after homogenization and their size and volume fraction increased with Ni content. The

TTs decreased as the Ni content were increased from 50.3 to 52 at. %. Furthermore, the strength of furnace cooled NiTiHf alloys was increased with Ni content due to the change in precipitation characteristic and solid solution hardening. The increase in critical strength has shown to improve the dimensional stability of NiTiHf alloys during thermal cycling under stress where almost full recovery was demonstrated at ultra-high stress level of 2 GPa for furnace cooled $Ni_{52}Ti_{28}Hf_{20}$.

In addition to compositional effects, the aging effects were investigated. In order to study the effects of thermal treatments on Ni-rich NiTiHf, the material were solution treated at 900 °C for three hours followed by water quenching to avoid formation of precipitates in the solutionized condition. It was shown that shape memory behavior and martensite morphology in Ni-rich NiTiHf alloys were mainly related to precipitates size and the distance between them. For summary, a schematic representation of effects of precipitates on strength and martensite morphology is shown in Figure 7.1. The TTs of Ni-rich NiTiHf were increased after aging at appropriate temperatures due to formation of Ni-rich precipitates that resulted in depletion of Ni from matrix and made the matrix relatively Ti-rich in contrast with nominal compassion which would result in an increase in TTs.

The strength of material highly depends on the size and interparticle distance of precipitates which could acts as obstacles against dislocation motion. Formation of fine precipitates with small interparticle distance increase the strength of material since they produced resistance to slip of dislocation. In other word, Small precipitates are sheared by dislocation cutting through them which new interface between precipitates and matrix is produced and increased the interfacial energy, hence, the strength of material improved. In the case of bigger precipitates with longer interparticle distances, dislocations could bypass the precipitates by looping around them instead of cutting through them as schematized in Figure 7.1. It is worth to mention that the high strength of furnace cooled $Ni_{52}Ti_{28}Hf_{20}$ with large precipitates can be linked to the intrinsic strength of the alloy compositions due to solid solution. In addition, the high strength can also be attributed to different martensite morphology and type of twinning in this material.

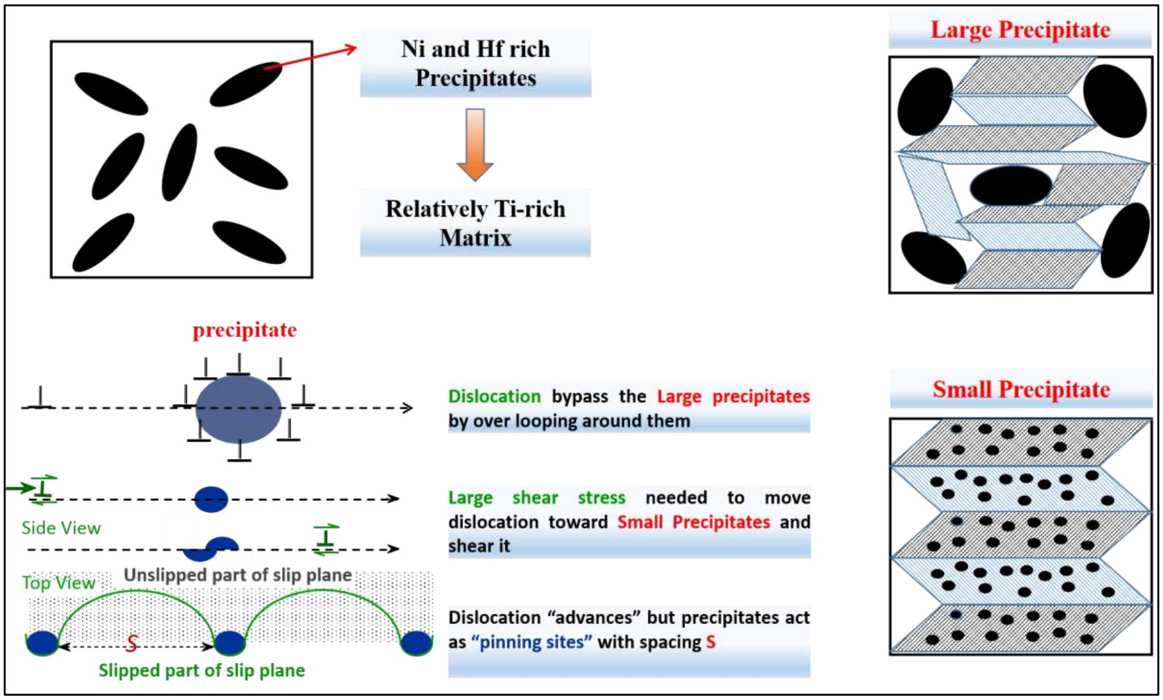

Figure 7.1: Schematic representation of effects of precipitate on strength and martensite morphology.

It was found that the martensite morphology and twinning type is function of precipitates characteristics. At low aging temperatures (450 °C-3h and 550 °C-3h), the strain field around the precipitates can still be accommodated during martensitic transformation. Therefore, the martensite plates were able to absorb numerous nanosize (less than 20 nm) precipitates once they started to grow. However, large precipitates (greater than 50 nm) formed after aging at high temperature (650 °C-3h) which act as obstacles to martensite variants growth and could not be absorbed. Thus, the nucleation and propagation of martensite variants was limited within the space between the particles as shown in Figure 7.1. In addition, (011) type I twins was the dominant twinning mode in the alloys with small precipitates while (001) compound and (011) type I twins were mostly observed with large precipitates.

Shape memory behavior of Ni-rich NiTiHf alloys are also related to precipitation characteristic. Formation of nanosize precipitates after 450 °C-3h aging suppress the nucleation of martensite where no martensitic transformation was observed under low stress levels for $Ni_{51.2}Ti_{28.8}Hf_{20}$ and $Ni_{52}Ti_{28}Hf_{20}$ alloys. It has been shown that additional undercooling is needed to complete the forward transformation after 450 °C-3h aging (Figures 4.13a and 4.19b) and the low strain-temperature slope during the forward transformation designates the high elastic energy storage during austenite to martensite transformation. The stored elastic energy is affected by martensite morphology and precipitation characteristics and will increase as the resistance to the progression of the phase transformation increases [37, 145, 147]. In the 450 °C-3h aged condition, the increased resistance can be attributed to the additional fine precipitates against interface motion. Therefore, the process of trying to bypass and absorb precipitates during forward transformation make the nucleation and propagations of martensite difficult. Thus, the slope of the transformation strain-temperature decreases as the stored elastic energy increases in the material due to increased constraints in the microstructures. However, the stored elastic energy may be relaxed as precipitates become larger due to formation of dislocation. In such case, the slop of transformation strain-temperature slope will become steeper due to easier nucleation and propagation of martensite plates, resulting in lower elastic energy storage.

Shape memory properties of Ni-rich NiTiHf alloys are highly composition, aging and orientation dependent. The recoverable strains in $Ni_{52}Ti_{28}Hf_{20}$ alloys are lower compared to the $Ni_{50.7}Ti_{29.3}Hf_{20}$ and $Ni_{51.2}Ti_{28.8}Hf_{20}$ in furnace cooled and aged conditions. The reason for the difference in recoverable strains of Ni-rich NiTiHf alloys can be attributed to the change in the twinning properties with composition. It should also be noted that transformation strain can be decreased due to increase in non-transformable precipitates which result in decreased volume fraction of matrix that undergo transformation. A detailed comparison between the twinning properties, precipitation characteristics and volume fractions of the forming precipitates would be useful to relate the microstructure to the shape memory properties.

Thermal hysteresis become narrow after three hours aging at 450 °C and 550 °C which can stem from hindering dislocation generation due to precipitation strengthening that may result to less energy dissipation. Another possible reason for the lower thermal hysteresis after aging can be a slight change of the lattice parameters of Ni-rich NiTiHf SMAs. It is known that when the compatibility between the transforming phases is better, less dissipation is expected [166]. Since the compatibility strongly depends on the lattice parameters of the transforming phases, which are subsequently dependent on matrix composition and temperature. Thus, it is possible that aging may modify the lattice parameters in a manner that could result in improved compability and subsequently smaller thermal hysteresis in aged Ni-rich NiTiHf alloys. In addtion, the increase in the thermal hysteresis with applied stress was observed in some conditions which was attributed to low strength of the material and subsequently easy dislocation generation at high stress levels. The decrease in thermal hysteresis with stress can also be due to the increase of volume fraction of favorable martensite variants, which results in decreased of dissipation energy due to less interaction between martensite variant interfaces. Low thermal hysteresis is a desire of the alloys that well be used in actuator applications.

In actuator type applications, work output is an essential parameter for making comparisons between various SMA families and for comparing the capability of SMAs to conventional actuators. In this case, work output can simply be defined as the product of applied stress and recoverable strain and was determined from the thermal cycling experiments. A summary of actuation strains and work outputs of selected NiTi-based SMAs are illustrated in Figure 7.2. Work output was less 20 J cm^{-3} with maximum actuation strain of ~4% for slightly Ni-rich $Ni_{50.3}Ti_{29.7}Hf_{20}$ under compression while the maximum work output of 29 J cm^{-3} was achieved under tension where the actuation strain was ~5%. The low work output under compression is due to the fact that the actuation strain in compression is lower than the tension. Slight increase of Ni content to 50.7 at. % resulted in a maximum work output of 22 J cm^{-3} while the actuation strain was decreased to 3%. The high work output of $Ni_{50.7}Ti_{29.3}Hf_{20}$ can be due to ability of the alloy to show near perfect dimensional stability at higher stress levels in contrast with $Ni_{50.3}Ti_{29.7}Hf_{20}$. As Ni concentration increased the maximum actuation strains decreased to below 2% while the high work outputs of 27 J cm^{-3} and 25 J cm^{-3} were achieved by $Ni_{51.2}Ti_{28.8}Hf_{20}$ and $Ni_{52}Ti_{28}Hf_{20}$ alloys, respectively. The high work output with low actuation strain is due to high strength of material and as a result perfect dimensional stability was observed at high stress levels of greater than 1500 MPa. In addition, NiTiHf single crystal reached to the highest work output of ~35 J cm $^{-3}$ due to the perfect dimensional stability under high stress levels and a reasonable actuation strain of 4%. In contrast to Ni-rich NiTiHf alloys, NiTi can reach a maximum actuation strain of 8% with a work output in the range of below 20 J cm $^{-3}$ [167] but they can only operate at temperatures below 100 °C. Addition of ternary alloys such as Pd, Pt, and Hf decrease the actuation strain but improve the strength of the material in some cases [5, 136] and increase the TTs. Work output for NiTiPd and NiTiPt HTSMAs is below 15 J cm^{-3}. On the other hand, $Ni_{45.3}Ti_{29.7}Hf_{20}Cu_5$ alloys can generate work outputs of around 14–15 J cm^{-3} [132] while NiTiHfNb alloys have work output levels of 17–18 J cm^{-3} above 100 °C [129] and 150 °C, respectively. Furthermore, $Ni_{45.3}Ti_{29.7}Hf_{20}Pd_5$ alloys can generate higher work outputs of 32–35 J/cm^3 [112] (up to 120 °C) while upper temperature capability is somewhat limited compared to the above mentioned NiTiHf-based alloys.

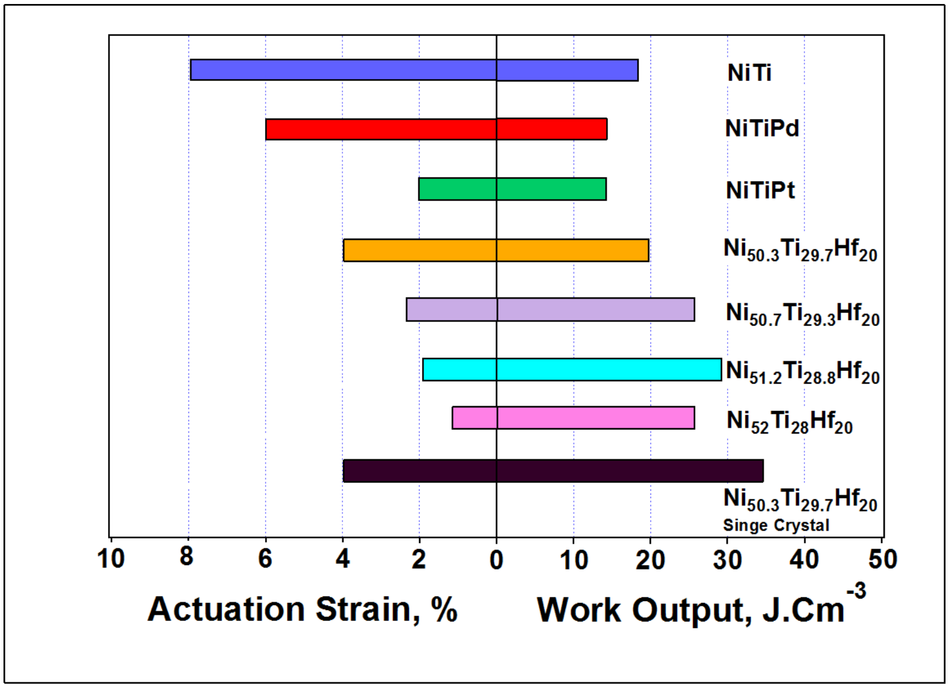

Figure 7.2: Comparison of work output and actuation strain of for typical NiTi-based SMAs.

The exceptional property of Ni-rich NiTiHf alloys is the high strength of these alloys where almost full recovery was observed at ultra-high stress levels as result of thermal and stress induced martensitic transformation. Ultra strength behavior has been mostly observed in nanoscale materials such as; nanowires, nanopillars, nanolayers, nanocrystals and nanoparticles materials [168]. Ultra strength phenomena in nanoscale materials can be characterized by the overall stress levels of sample reaching to a significant fraction of its ideal strength, defined as the highest stress a perfect crystal can sustain without any plastic deformation [168, 169]. The ideal strength of alloys are defined as the one tenth of their elastic modulus (E) [169-171]. Alternatively, alloys can be considered to have ultra-strength if their strength is in GPa levels [171]. The deformation mechanisms of ultra-strength materials are related to the nucleation and movement of dislocations, dislocation-interface interactions and deformation twinning [168, 171]. In the current research, $Ni_{51.2}Ti_{28.8}Hf_{20}$ and $Ni_{52}Ti_{28}Hf_{20}$ alloys demonstrated ultra-strength where near perfect dimensional stability was experimented during thermal cycling above 1500 MPa. Moreover, full superelastic recovery with about 4% total strain at low and high temperatures was observed at stress levels of about 2 GPa after three hours of aging at 450 °C and 550 °C.

Ultimate strength of different class of materials [172, 173] are summarized in Figure 7.3. The elastic modulus of austenite is determined from stress-strain curves to be ~80 GPa for aged Ni-rich NiTiHf alloys. Since the alloy can work under 2 GPa, the ratio of actual strength to ideal strength can be calculated as 25%, which is quite high for conventional materials since the ratio of actual to ideal strength of conventional steels are less 20 %. It is clear from Figure 7.3 that the strength of Ni-rich NiTiHf material is higher than conventional steels and shape memory alloys. In addition, conventional strength of most metals decreases with increasing temperature while it has been demonstrated that Ni-rich $Ni_{51.2}Ti_{28.8}Hf_{20}$ are capable to reach a ultra-strength at room temperature and also high temperatures after appropriates heat treatments. Other than the presence of fine precipitates with small interparticle distance, it has been reported that the strengthening of this material is the result of point defects clusters or additional ordering on austenite phase and also antisite defects that expected to be present in Ni-rich NiTiHf alloys [Coughlin 2015]. The ability to show full recovery after loading to 2 GPa at room and high temperatures make Ni-rich NiTiHf alloys suitable for biomedical and high temperature applications.

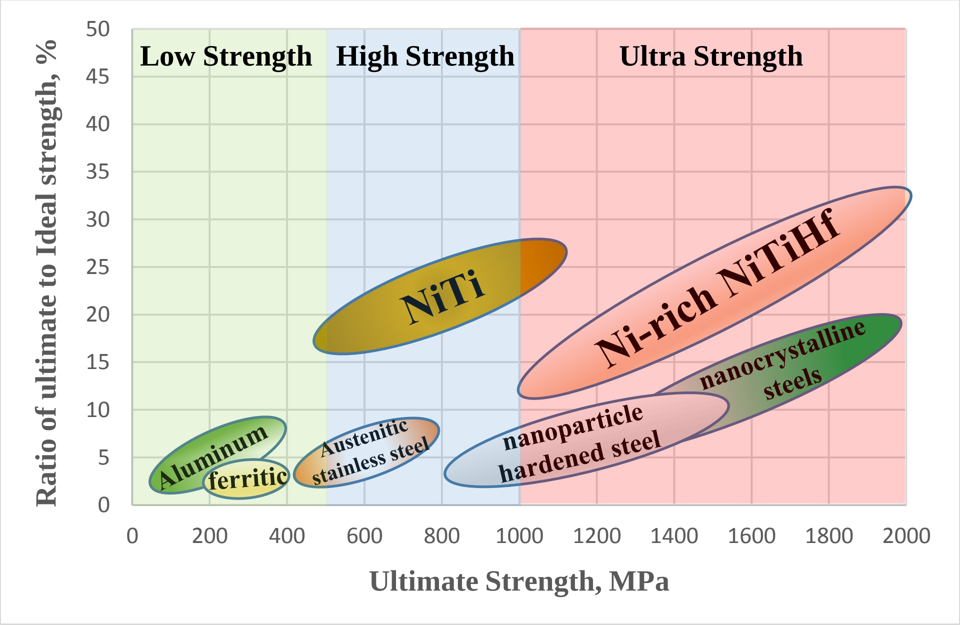

Figure 7.3: Comparison of the strength of common materials.

7.2 Future Works

This project has shown that slight changes in chemical composition create significant changes in martensite morphology and consequently material properties. In addition, it was discovered that three hours aging at 450 °C and 550 °C improve HTSMAs properties of the Ni-rich NiTiHf alloys and orientation dependence of $Ni_{50.3}Ti_{29.7}Hf_{20}$ was investigated. The thermal cycling under stress and isothermal compression experiments were used were used to aid modeling efforts that will help material behavior predictions for future applications.

In addition of observed results, possible future studies on these types of alloy systems could be to:

1. Detailed microstructural analysis to investigate the reasons of decrease in TTs after aging at low temperatures (below 400 °C).
2. Study the effects of aging under stress on the shape memory properties in NiTiHf alloy systems.
3. Characterize the fatigue properties of NiTiHf alloys
4. Investigate stress generation capabilities of single crystals and polycrystalline NiTiHf alloys and compare them to NiTi alloys.
5. Detailed microstructural analysis to find out the difference in deformation mechanism under tension and compression.
6. Investigate the damping and dynamic behavior of NiTiHf alloys.

References

[1] Lagoudas DC. Shape Memory Alloys: Modeling and Engineering Applications. New York: Springer, 2008.

[2] Otsuka K, Ren XB. Intermetallics 1999;7:511.

[3] Noebe R, Biles T, Padula SA. NiTi-Based High-Temperature Shape-Memory Alloys: Properties, Prospects, and Potential Applications

Advanced Structural Materials. 2007. p.145.

[4] Firstov GS, Van Humbeeck J, Koval YN. J. Intell. Mater. Syst. Struct. 2006;17:1041.

[5] Ma J, Karaman I, Noebe RD. Int. Mater. Rev. 2010;55:257.

[6] Hartl D, Lagoudas DC. Proceedings of the Institution of Mechanical Engineers, Part G: Journal of Aerospace Engineering 2007;221:535.

[7] Firstov GS, Van Humbeeck J, Koval YN. Scr. Mater. 2004;50:243.

[8] Kockar B, Karaman I, Kim JI, Chumlyakov Y. Scr. Mater. 2006;54:2203.

[9] Otsuka K, Wayman CM. Shape Memory Materials: Cambridge University Press, 1998.

[10] Kassner ME, Pérez-Prado MT. Prog. Mater. Sci. 2000;45:1.

[11] Besseghini S, Villa E, Tuissi A. Mater. Sci. Eng. A-Struct. Mater. Prop. Microstruct. Process. 1999;273:390.

[12] Meng XL, Zheng YF, Wang Z, Zhao LC. Scr. Mater. 2000;42:341.

[13] Nishida M, Wayman CM. Materials Science and Engineering 1987;93:191.

[14] Frick CP, Ortega AM, Tyber J, Maksound AEM, Maier HJ, Liu YN, Gall K. Mater. Sci. Eng. A-Struct. Mater. Prop. Microstruct. Process. 2005;405:34.

[15] Golberg D, Xu Y, Murakami Y, Morito S, Otsuka K, Ueki T, Horikawa H. Intermetallics 1995;3:35.

[16] Golberg D, Xu Y, Murakami Y, Otsuka K, Ueki T, Horikawa H. Mater. Lett. 1995;22:241.

[17] Khalil-Allafi J, Dlouhy A, Eggeler G. Acta Materialia 2002;50:4255.

[18] Chumlyakov YI, Panchenko EY, Aksenov VB, Kireeva IV, Kuksa MP, Karaman I, Sehitoglu H. Journal De Physique Iv 2004;115:21.

[19] Sehitoglu H, Karaman I, Anderson R, Zhang X, Gall K, Maier HJ, Chumlyakov Y. Acta Materialia 2000;48:3311.

[20] Jung J, Ghosh G, Olson GB. Acta Materialia 2003;51:6341.

[21] Jung J, Ghosh G, Olson GB. Metallurgical and Materials Transactions A 2003;34A:1221.

[22] Kurdjumove GV, Khandros LG. Doklady Akademii Nauk 1949;66:211.

[23] Chang LC, Read TA. Journal of Metals 1951;3:47.

[24] Buehler WJ, Wiley RC, Gilfrich JV. Applied Physics 1963;34:1475.

[25] Wang FE, Buehler WJ, Pickart SJ. Applied Physics 1965;36:3232.

[26] Schetky LM. In: Saburi T, editor. The industrial applications of shape memory alloys in North America. 2000. p.9.

[27] Wayman M, Harrison J. Journal of Minerals, Metals and Materials 1989;41:26.

[28] Wu MH, Schetky LM. Industrial applications for shape memory alloys. International Conferece on Shape Memory and Superlastic Technologies. California, 2000.

[29] Melton K, Mercier O. Metallic Trans 1978;9A.

[30] Miyazaki S, Mizukoshi K, Ueki T, Sakuma T, Liu Y. Materials Science and Engineering: A 1999;273–275:658.

[31] Hsieh SF, Wu SK. Journal of Alloys and Compounds 1998;266:276.

[32] Wollants P, Roos J, Delaey L. Progress in Materials Science 1993;37:227.

[33] Panchenko E, Chumlyakov Y, Kireeva I, Ovsyannikov A, Sehitoglu H, Karaman I, Maier Y. The Physics of Metals and Metallography 2008;106:577.
[34] Otsuka K, Ren X. Progress in materials science 2005;50:511.
[35] Sehitoglu H, Efstathiou C, Maier HJ, Chumlyakov Y. Mechanics of Materials 2006;38:538.
[36] Sehitoglu H, Karaman I, Zhang XY, Chumlyakov Y, Maier HJ. Scripta Materialia 2001;44:779.
[37] Hamilton RF, Sehitoglu H, Chumlyakov Y, Maier HJ. Acta Materialia 2004;52:3383.
[38] Tong H, Wayman C. Acta Metallurgica 1974;22:887.
[39] Tong H, Wayman C. Acta Metallurgica 1975;23:209.
[40] Benafan O, Noebe R, Padula II S, Garg A, Clausen B, Vogel S, Vaidyanathan R. International Journal of Plasticity 2013;51:103.
[41] Otsuka K, Sawamura T, Shimizu K. Physica status solidi (a) 1971;5:457.
[42] Kudoh Y, Tokonami M, Miyazaki S, Otsuka K. Acta Metallurgica 1985;33:2049.
[43] Gall K, Sehitoglu H, Chumlyakov YI, Zuev YL, Karaman I. Scripta materialia 1998;39:699.
[44] Liu Y, Blanc M, Tan G, Kim J, Miyazaki S. Materials Science and Engineering: A 2006;438:617.
[45] Miyazaki S, Wayman C. Acta metallurgica 1988;36:181.
[46] Šittner P, Lukáš P, Novák V, Daymond MR, Swallowe GM. Materials Science and Engineering: A 2004;378:97.
[47] Khalil-Allafi J, Eggeler G, Schmahl WW, Sheptyakov D. Materials Science and Engineering: A 2006;438–440:593.
[48] Khalil Allafi J, Ren X, Eggeler G. Acta Materialia 2002;50:793.
[49] Bataillard L, Bidaux J-E, Gotthardt R. Philosophical magazine A 1998;78:327.
[50] Nishida M, Hara T, Ohba T, Yamaguchi K, Tanaka K, Yamauchi K. Materials Transactions 2003;44:2631.
[51] Tang W, Sundman B, Sandström R, Qiu C. Acta materialia 1999;47:3457.
[52] Wasilewski R, Butler S, Hanlon J, Worden D. Metallurgical Transactions 1971;2:229.
[53] Ravari BK, Farjami S, Nishida M. Acta Materialia 2014;69:17.
[54] Hornbogen E, Mertinger V, Wurzel D. Scr. Mater. 2001;44:171.
[55] Khamei AA, Dehghani K. Journal of Alloys and Compounds 2010;490:377.
[56] Frenzel J, George EP, Dlouhy A, Somsen C, Wagner M-X, Eggeler G. Acta Materialia 2010;58:3444.
[57] Duerig TW, Melton K, Stöckel D. Engineering aspects of shape memory alloys: Butterworth-Heinemann, 2013.
[58] Tang W. Metallurgical and Materials Transactions A 1997;28:537.
[59] Nishida M, Wayman CM, Honma T. Metall Trans 1986;17A:1505.
[60] Carroll M, Somsen C, Eggeler G. Scr. Mater. 2004;50:187.
[61] Michutta J, Somsen C, Yawny A, Dlouhy A, Eggeler G. Acta materialia 2006;54:3525.
[62] Prasher M, Sen D. Journal of Alloys and Compounds 2014;615:469.
[63] Miyazaki S, Imai T, Otsuka K, Suzuki Y. Scripta Metallurgica 1981;15:853.
[64] Miyazaki S, Otsuka K, Suzuki Y. Scripta Metallurgica 1981;15:287.
[65] Yoneyama T, Miyazaki S. Shape memory alloys for biomedical applications: Elsevier, 2008.
[66] Knowles K, Smith D. Acta Metallurgica 1981;29:101.
[67] Zheng Y, Huang B, Zhang J, Zhao L. Materials Science and Engineering: A 2000;279:25.
[68] Sittner P, Liu Y, Novák V. Journal of the Mechanics and Physics of Solids 2005;53:1719.
[69] Gall K, Sehitoglu H, Anderson R, Karaman I, Chumlyakov YI, Kireeva IV. Materials Science and Engineering: A 2001;317:85.

[70] Sehitoglu H, Jun J, Zhang X, Karaman I, Chumlyakov Y, Maier HJ, Gall K. Acta Materialia 2001;49:3609.
[71] Orgéas L, Favier D. Acta Materialia 1998;46:5579.
[72] Liu Y, Mahmud A, Kursawe F, Nam T-H. Journal of Alloys and Compounds 2008;449:82.
[73] Sehitoglu H, Hamilton R, Canadinc D, Zhang X, Gall K, Karaman I, Chumlyakov Y, Maier H. Metallurgical and Materials Transactions A 2003;34:5.
[74] Ball JM, James RD. Arch. Ration. Mech. Anal. 1987;100:13.
[75] Saburi T, Nenno S. Solid to Solid Phase Transformations 1981:1455.
[76] Miyazaki S, Kimura S, Otsuka K, Suzuki Y. Scripta metallurgica 1984;18:883.
[77] Nishida M, Ohgi H, Itai I, Chiba A, Yamauchi K. Acta metallurgica et materialia 1995;43:1219.
[78] Gall K, Sehitoglu H. International Journal of Plasticity 1999;15:69.
[79] Gall K, Sehitoglu H, Chumlyakov YI, Kireeva IV. Acta Materialia 1999;47:1203.
[80] Liu Y, Xie ZL, Van Humbeeck J, Delaey L. Acta materialia 1999;47:645.
[81] Donkersloot H, Van Vucht J. Journal of the Less Common Metals 1970;20:83.
[82] Eckelmeyer K. Scripta Metallurgica 1976;10:667.
[83] Wu SK, Wayman CM. Metallography 1987;20:359.
[84] Wu SK, Wayman CM, Procedure E, Results E. Scripta Metallurgica 1987;21:83.
[85] Noebe R, Gaydosh D, II SP, Garg A, Biles T, Nathal M. Smart Structures and Materials 2005: Active Materials: Behavior and Mechanics, SPIE Conf. 2005;5761:364.
[86] Lindquist P, Wayman C. Butterworth-Heinemann, Engineering Aspects of Shape Memory Alloys(UK), 1990 1990:58.
[87] Shimizu S, Xu Y, Okunishi E, Tanaka S, Otsuka K, Mitose K. Materials Letters 1998;34:23.
[88] Kovarik L, Yang F, Garg A, Diercks D, Kaufman M, Noebe R, Mills M. Acta materialia 2010;58:4660.
[89] Meisner LL, Sivokha VP. De Physique Iv 1995;5.
[90] Van Humbeeck J. J. Eng. Mater. Technol.-Trans. ASME 1999;121:98.
[91] Meng XL, Cai W, Chen F, Zhao LC. Scr. Mater. 2006;54:1599.
[92] Angst DR, Thoma PE, Kao MY. J. Phys. IV 1995;5:747.
[93] Wang YQ, Zheng YF, Cai W, Zhao LC. Scr. Mater. 1999;40:1327.
[94] Zarinejad M, Liu Y, White TJ. Intermetallics 2008;16:876.
[95] Potapov P, Shelyakov A, Gulyaev A, Svistunov E, Matveeva N, Hodgson D. Materials Letters 1997;32:247.
[96] Otsuka K, Sawamura T, Shimizu Ki, Wayman C. Metallurgical Transactions 1971;2:2583.
[97] Dilibal S, Sehitoglu H, Hamilton R, Maier H, Chumlyakov Y. Materials Science and Engineering: A 2011;528:2875.
[98] Z.Pu HTaKW. SPIE, vol. 2441, 1995. p.171.
[99] J. WKHPZ. Martensite transformation of (HfxTi50−x)Ni50 shape memory alloys. ICOMAT 95 : International Conference on Martensitic Transformation, vol. 5, 1995. p.759.
[100] König D, Zarnetta R, Savan A, Brunken H, Ludwig A. Acta Materialia 2011;59:3267.
[101] Thoma PE, Boehm JJ. Materials Science and Engineering: A 1999;273–275:385.
[102] Meng XL, Cai W, Fu YD, Zhang JX, Zhao LC. Acta Materialia 2010;58:3751.
[103] Tong Y, Chen F, Tian B, Li L, Zheng Y. Materials Letters 2009;63:1869.
[104] Javadi M, Belbasi M, Salehi M, Afshar MR. J. of Materi Eng and Perform 2011;20:618.
[105] Zhang J, Sato M, Ishida A. Philosophical Magazine A 2002;82:1433.
[106] Han XD, Zou WH, Wang R, Zhang Z, Yang DZ. Acta Materialia 1996;44:3711.
[107] Han X, Chung C, Wang R, Zhang Z, Lai J, Yang D. Materials Transactions, JIM 1997;38:842.

[108] Meng XL, Cai W, Zheng YF, Zhao LC. Materials Science and Engineering: A 2006;438–440:666.

[109] Coughlin D, Phillips P, Bigelow G, Garg A, Noebe R, Mills M. Scripta Materialia 2012;67:112.

[110] Santamarta R, Arróyave R, Pons J, Evirgen A, Karaman I, Karaca HE, Noebe RD. Acta Materialia 2013;61:6191.

[111] Yang F, Coughlin DR, Phillips PJ, Yang L, Devaraj A, Kovarik L, Noebe RD, Mills MJ. Acta Materialia 2013;61:3335.

[112] Karaca HE, Acar E, Ded GS, Basaran B, Tobe H, Noebe RD, Bigelow G, Chumlyakov YI. Acta Materialia 2013;61:5036.

[113] Bigelow G, Garg A, Padula II S, Gaydosh D, Noebe R. Scripta Materialia 2011;64:725.

[114] Karaca HE, Saghaian SM, Ded G, Tobe H, Basaran B, Maier HJ, Noebe RD, Chumlyakov YI. Acta Materialia 2013;61:7422.

[115] Han X, Wang R, Zhang Z, Yang D. Acta materialia 1998;46:273.

[116] Evirgen A, Basner F, Karaman I, Noebe RD, Pons J, Santamarta R. Funct. Mater. Lett. 2012;5.

[117] Dalle F, Perrin E, Vermaut P, Masse M, Portier R. Acta materialia 2002;50:3557.

[118] Meng X, Cai W, Zheng Y, Tong Y, Zhao L, Zhou L. Materials Letters 2002;55:111.

[119] Meng X, Cai W, Wang L, Zheng Y, Zhao L, Zhou L. Scripta materialia 2001;45:1177.

[120] Meng XL, Zheng YF, Wang Z, Zhao LC. Materials Letters 2000;45:128.

[121] Olier P, Brachet J, Bechade J, Foucher C, Guenin G. J. Phys. IV 1995;C8:741.

[122] Meng XL, Zheng YF, Cai W, Zhao LC. Journal of Alloys and Compounds 2004;372:180.

[123] Besseghini S, Villa E, Tuissi A. Materials Science & Engineering A 1999;273-275:390.

[124] Acar E, Karaca HE, Basaran B, Yang F, Mills MJ, Noebe RD, Chumlyakov YI. Materials Science and Engineering: A 2013;573:161.

[125] Acar E, Karaca HE, Tobe H, Noebe RD, Chumlyakov YI. Journal of Alloys and Compounds 2013;578:297.

[126] Karaca HE, Acar E, Basaran B, Noebe RD, Bigelow G, Garg A, Yang F, Mills MJ, Chumlyakov YI. Scr. Mater. 2012;67:728.

[127] Karaca HE, Acar E, Basaran B, Noebe RD, Chumlyakov YI. Scripta Materialia 2012;67:447.

[128] Ded G. Characterization of Ni-rich NiTiHf based High Temperature Shape Memory Alloys. Mechanical Engineering, vol. Master of Science: University of Kentucky, 2010.

[129] Kim HY, Jinguu T, Nam T-h, Miyazaki S. Scr. Mater. 2011;65:846.

[130] Meng XL, Cai W, Lau KT, Zhao LC, Zhou LM. Intermetallics 2005;13:197.

[131] Liang XL, Chen Y, Shen HM, Zhang ZF, Li W, Wang YN. Solid State Commun. 2001;119:381.

[132] Karaca H, Acar E, Ded G, Saghaian S, Basaran B, Tobe H, Kok M, Maier H, Noebe R, Chumlyakov Y. Materials Science and Engineering: A 2015;627:82.

[133] Lagoudas DC. Science and Business Media, LLC 2008.

[134] Zarinejad M, Liu Y, Tong Y. Intermetallics 2009;17:914.

[135] Zarinejad M, Liu Y. Advanced Functional Materials 2008;18:2789.

[136] Karaca HE, Acar E, Tobe H, Saghaian SM. Materials Science and Technology 2014;30:1530.

[137] Evirgen A, Karaman I, Santamarta R, Pons J, Noebe RD. Acta Materialia 2015;83:48.

[138] Evirgen A, Karaman I, Noebe RD, Santamarta R, Pons J. Scr. Mater. 2013;69:354.

[139] Benafan O, Garg A, Noebe RD, Bigelow GS, Padula II SA, Gaydosh DJ, Schell N, Mabe JH, Vaidyanathan R. Intermetallics 2014;50:94.

[140] Benafan O, Noebe RD, Padula SA, Vaidyanathan R. Metallurgical and materials Transactions A 2012;43:4539.
[141] Kireeva I, Picornell C, Pons J, Kretinina I, Chumlyakov YI, Cesari E. Acta Materialia 2014;68:127.
[142] Coughlin DR. Characterization of Stoichiometric and Aging Effects on NiTiHf High Temperature Shape Memory Alloys. vol. PHD: Ohio State University, 2013.
[143] Sandu AM, Tsuchiya K, Tabuchi M, Yamamoto S, Todaka Y, Umemoto M. Materials Transactions 2007;48:432.
[144] Zhang J, Cai W, Ren X, Otsuka K, Asai M. JIM, Materials Transactions 1999;40:1367.
[145] Salzbrenner R, Cohen M. Acta Metallurgica 1979;27:739.
[146] Rösner H, Schloßmacher P, Shelyakov A, Glezer A. Acta materialia 2001;49:1541.
[147] Olson GB, Cohen M. Scripta Metallurgica 1975;9:1247.
[148] Wasilewski R. Metallurgical and Materials Transactions B 1971;2:2973.
[149] Liu Y, Xie Z, Van Humbeeck J, Delaey L. Acta Materialia 1998;46:4325.
[150] Xie Z, Liu Y, Van Humbeeck J. Acta Materialia 1998;46:1989.
[151] Panchenko E, Chumlyakov Y, Maier H, Timofeeva E, Karaman I. Intermetallics 2010;18:2458.
[152] Plietsch R, Ehrlich K. Acta materialia 1997;45:2417.
[153] Jacobus K, Sehitoglu H, Balzer M. Metallurgical and Materials Transactions A 1996;27:3066.
[154] Sehitoglu H, Karaman I, Zhang X, Viswanath A, Chumlyakov Y, Maier HJ. Acta Materialia 2001;49:3621.
[155] Karaca HE, Karaman I, Chumlyakov YI, Lagoudas DC, Zhang X. Scr. Mater. 2004;51:261.
[156] Stebner AP, Bigelow GS, Yang J, Shukla DP, Saghaian SM, Rogers R, Garg A, Karaca HE, Chumlyakov Y, Bhattacharya K, Noebe RD. Acta Materialia 2014;76:40.
[157] Karaca HE, Saghaian SM, Basaran B, Bigelow GS, Noebe RD, Chumlyakov YI. Scr. Mater. 2011;65:577.
[158] Miyazaki S, Otsuka K, Wayman C. Acta Metallurgica 1989;37:1873.
[159] Hane KF, Shield TW. Acta Materialia 1999;47:2603.
[160] James RD, Hane KF. Acta Materialia 2000;48:197.
[161] Surikova N, Chumlyakov YI. PHYSICS OF METALS AND METALLOGRAPHY C/C OF FIZIKA METALLOV I METALLOVEDENIE 2000;89:196.
[162] Ezaz T, Wang J, Sehitoglu H, Maier HJ. Acta Materialia 2013;61:67.
[163] Ortín J, Delaey L. International Journal of Non-Linear Mechanics 2002;37:1275.
[164] Liu Y, Galvin SP. Acta Materialia 1997;45:4431.
[165] Acar E, Karaca HE, Tobe H, Noebe RD, Chumlyakov YI. Intermetallics 2014;54:60.
[166] Cui J, Chu YS, Famodu OO, Furuya Y, Hattrick-Simpers J, James RD, Ludwig A, Thienhaus S, Wuttig M, Zhang Z, Takeuchi I. Nat Mater 2006;5:286.
[167] Grummon DS. Minerals: Metals and Materials Society 2003;55:24.
[168] Zhu T, Li J. Prog. Mater. Sci. 2010;55:710.
[169] Ogata S, Li J, Hirosaki N, Shibutani Y, Yip S. Physical Review B 2004;70:104104.
[170] Pokluda J, Černý M, Šandera P, Šob M. Journal of computer-aided materials design 2004;11:1.
[171] Zhu T, Li J, Ogata S, Yip S. Mrs Bulletin 2009;34:167.
[172] Shackelford JF, Alexander W. CRC materials science and engineering handbook: CRC press, 2000.
[173] Raabe D, Ponge D, Dmitrieva O, Sander B. Scr. Mater. 2009;60:1141.

VITA

Sayed M. Saghaian was born in 1987 in Kentucky, USA. He got his bachelor degree in mechanical engineering from University of Kentucky, Kentucky, USA. In August 2010, he was admitted to PHD program in Mechanical Engineering department at the University of Kentucky. He has been work as a PhD student on high temperature shape memory alloys project funded by NASA since 2010. His research interests include process-microstructure-mechanical properties relationships in metallic materials and mechanics of advance metallic materials. He has published seven journal articles and a book chapter during his graduate tenure.